N° d'ordre : 2007-30 ANNÉE 2007

THÈSE

présentée devant
L'ÉCOLE CENTRALE DE LYON

pour obtenir
le titre de DOCTEUR
SPÉCIALITÉ ACOUSTIQUE

par

Thomas Emmert

Development of a multidomain high-order algorithm for computational aeroacoustics: Application to subsonic and transonic confined flows

Soutenue le 15 novembre 2007 devant la Commission d'Examen

JURY

M.	Christophe BAILLY	prof. Ecole Centrale de Lyon
M.	Patrick BONTOUX	DR CNRS, MSNM-GP Marseille
M.	Sébastien CANDEL	prof. Ecole Centrale de Paris
M.	Philippe LAFON	ingénieur chercheur EDF & LaMSID
M.	Éric MANOHA	ingénieur chercheur ONERA
M.	Claus-Dieter MUNZ (Rapporteur)	prof. Université de Stuttgart
M.	Pierre SAGAUT (Rapporteur)	prof. Université Paris VI

Laboratoire de Mécanique des Fluides et d'Acoustique
UMR CNRS 5509 et École Centrale de Lyon

Ce travail s'est déroulé au sein du Laboratoire de Mécanique des Structures Industrielles Durables, UMR EDF CNRS 2832. Il s'est effectué dans le cadre de la collaboration entre le département Analyses Mécaniques et Acoustique d'EDF R&D et le Laboratoire de Mécanique des Fluides et d'Acoustique de l'Ecole Centrale Lyon.

Je souhaite tout d'abord remercier chaleureusement Philippe Lafon, ingénieur chercheur et Christophe Bailly, professeur de l'ECL, pour avoir encadré cette thèse et pour m'avoir accordé leur confiance. Je tiens à remercier Stéphane Andrieux pour m'avoir accueilli au sein du LaMSID.

J'exprime tout particulièrement mes remerciements à Claus-Dieter Munz et à Pierre Sagaut qui m'ont fait l'honneur d'accepter d'être rapporteurs de mon travail. Je remercie sincèrement Sébastien Candel, Patrick Bontoux et Eric Manoha d'avoir fait partie du jury de thèse.

Je remercie les anciens thésards du Centre Acoustique de l'Ecole Centrale de Lyon et notamment Julien Berland, Vincent Fleury et Olivier Marsden dont j'ai eu l'honneur d'être le stagiaire pendant mon travail de fin d'études au Centre Acoustique.

Je remercie les ingénieurs du groupe T63, pour leur accueil chaleureux. Merci notamment à Sébastien Caillaud, Fabien Crouzet, Jean-Paul Devos, Michel Guivarch, Fabrice Junker et Pierre Moussou.

Je remercie les doctorants et les post doctorants du LaMSID, qui m'ont suivi au fil de ces trois années. Une pensée particulière est réservée à Josselin Delmas, Amine Sbitti, Mohamed Torkhani, Khaled Hadj Sassi, Pierre-Emmanuel Dumouchel, Benjamin Goult et Frédéric Daude. Un grand merci à Géraldine Fassassi pour son efficacité à résoudre nos problèmes administratifs. Merci également à Maria et Catherine pour le café bienfaiteur du matin.

Finalement, je remercie Lucie pour m'avoir supporté et encouragé pendant presque trois ans et aussi tous les habitants du 9 rue des Citeaux; Beatrice et Dominic, Carole, Bertrand et Jules, Christine, Patrice, Boris, Maxime, Pascale et Johan. Le temps que j'ai passé avec eux fut une source de motivation et d'inspiration. Un grand merci également à ma famille, notamment à mon frère Andi, dont le soutien a rendu la fin de ma thèse possible.

Contents

Introduction

Flows generate noise, and noise often interacts with flows through a feedback loop. These complex mechanisms raise many questions of fundamental, technical and industrial interests. Since the 50's and the development of turbojet engines for commercial aircrafts, the need to deal with these problems has spread to other industrial fields: ground transportation, energy production, ...

Aeroacoustics is considered as a branch of fluid mechanics. But the nature of acoustics fluctuations that are compressible, propagative and of small amplitude takes a special place in the field of fluid mechanics that usually deals with incompressible, convective, turbulent fluctuations draining a significant percentage of the main flow energy. Here lies the difficulty of aeroacoustics which is devoted to flow induced noise and more generally to flow acoustics phenomena.

Industrial background

In the industrial field of interest for EDF, strong aeroacoustic phenomena are often generated when pipe flows are disturbed by flow control devices. That is the case, for example, downstream control valve at small aperture such as shown in Figure 1 (a). The pressure ratio is very high and the flow is then transonic. In such shocked configurations, flow patterns are very sensitive to instabilities and this can lead to strong pressure oscillations when they are in resonance with acoustic modes [95, 6]. Other examples are given by diffuser flows where oscillations are generated due to the interaction of a normal shock with a separating shear or boundary layer [24, 23]. Self-sustained oscillations of the shock wave can couple with longitudinal acoustic duct modes [143] and can lead to high amplitude oscillations.

That is also the case in subsonic flow when shear layers or jets impinge on downstream obstacles. It is well know that in such situations, self-sustained oscillations can appear. The flow above a shallow cavity is a typical illustration of this phenomenon. An industrial example is given in Figure 1 (b) showing a gate valve with a cavity located at the bottom of the valve. Due to confinement, coupling can occur with transverse duct modes when the frequency of cavity oscillations matches the resonant frequency of the duct. This leads to high amplitude pressure fluctuations even at low Mach numbers whereas for open cavities, no considerable noise generation is observed. The same phenomenon can even be found in nearly incompressible flow such as high pressure water flow through orifices [129]. The consequence of these phenomena is the generation of large amplitude acoustic tones that are undesirable as regards vibrations of pipe structures and protection of nearby workers from high acoustic levels.

All these aeroacoustic phenomena exhibit the same physical behavior: they occur when a self-

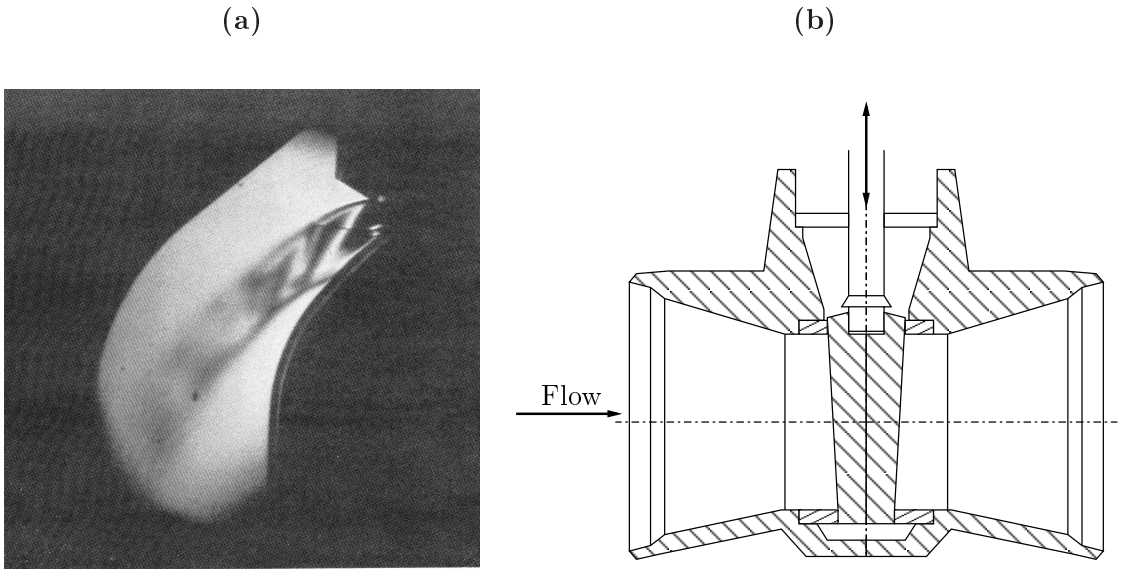

Figure 1: Examples of flow control devices: **(a)** Strioscopy of the flow in a control valve; **(a)** gate valve.

sustained oscillation due to a flow instability (shock, jet, shear layer) is coupled with an acoustic resonator. They also clearly emphasize feedback loops from the acoustics to the aerodynamics.

Computational issues

Since the beginning of the 50's and the birth of aeroacoustics as a new scientific field through the publication by Lighthill of its founding papers, the problem is mainly how to use the information coming from the aerodynamics and especially how to link aerodynamics and aeroacoustics in a modeling point of view. Although acoustics and aerodynamics are two branches of fluid mechanics, classical methods used in Computational Fluid Dynamics (CFD) can not be applied easily. This is due to the disparity of scales and dynamics between the aerodynamic field and the acoustic field. For example, for a free jet at Mach $M = 0.9$, the pressure fluctuations of the acoustic field is about 100 times smaller than the pressure fluctuations of the aerodynamic field. The disparity is even greater between the velocity fluctuations of the acoustic field and the aerodynamic field. An error of 1% in the computation of the aerodynamic field therefore produces an error of 100% for the acoustic field. As a result, two approaches have been developed in the past.

The first approach is based on the so-called hybrid methods that consist of a two-step procedure. First, the incompressible mean flow field is calculated, then a source term is defined and at last an acoustic solver gives the propagation field generated by the source. That is the principle of Lighthill's or Ffowcs-Williams's analogies that use integral methods as the acoustic solver but that is also the principle of the methods based on the computation of Linearized Euler Equations (LEE). In this first approach, the flow is obtained from classical incompressible low-order flow solvers giving steady (Reynolds Averaged Navier-Stokes (RANS) models) or unsteady (Unsteady RANS (URANS), Large-Eddy Simulation (LES)) results. The source term expression can be either statistical [17, 10], stochastic [16, 12, 91, 11, 52] or temporal [14, 41].

It has been shown above that in many issues, the acoustic field interacts with the flow field. Particularly in ducted configurations, strong acoustic feedback mechanisms are involved. For those problems, the hybrid approaches are no longer valid and it is necessary to use the second modeling approach which implies to solve flow and acoustic fields at once [54, 29] . This approach is called Direct Noise Computation (DNC). In this case, standard low-order CFD techniques are difficult to use because they are too dissipative and too dispersive so they can not preserve the amplitude and the phase of the acoustic fluctuations. Large efforts have been carried out to develop numerical techniques suitable to Computational AeroAcoustics (CAA) [123, 40]. An important step was made with the Dispersion Relation Preserving schemes introduced by Tam and Webb [128]. These schemes are based on high-order accurate finite differences, optimized in order to minimize the dispersion error. Although they are restricted to structured computational grids and despite of the impressive rise in computing power, their computational efficiency compared to finite volume methods such as spectral volume or discontinuous Galerkin methods made them very popular. Following this principle, Bogey and Bailly [30] proposed improved schemes which have proved their efficiency on jet noise computations [29]. In order to treat more complicated geometries, Marsden [92] applied these schemes on curvilinear meshes around bodies such as cylinders or a NACA0012 profile. The present work is on the same path and aims to be able to deal with configurations close to industrial applications.

Objectives of the thesis

The objectives of the thesis are to develop a high-order finite-difference algorithm for Euler and Navier-Stokes equations for the simulation of aeroacoustic phenomena in complex geometries and to apply it on flow configurations that are typical of industrial applications. The flows to be addressed are subsonic, transonic and supersonic.

In order to apply high-order finite-difference schemes in complex geometries, an overset-grid approach is chosen. Classically used for acoustic propagation problems, this approach [43] has recently been adapted for the Direct Noise Computation approach and LES [116, 92, 45, 134]. In order to avoid algorithmic developments that are not in the scope of this work, it is necessary to use available tools dealing with overset grids. For example, the freely available *Overture* library developed by the Lawrence Livermore National Laboratory seems to be a good candidate for the creation of overset grids in complex geometries. In this work the applicability of such tools will be studied. In particular, the crucial problem of the communication between grids through interpolation will be examined because interpolation must be of high-order to preserve the accuracy given by the numerical schemes.

Another disadvantage of finite-difference schemes is that they exhibit stability problems due to their minimized dissipation. In general, high-order finite-difference schemes fail to simulate flows with strong shocks. Shock-capturing filters have therefore been developed in the literature for high-order accurate computation of transonic and supersonic shock-containing flows. In this work, we will verify that they are suitable to model aeroacoustic phenomena and will adapt them if necessary.

After having validated the algorithm on classical test cases for CAA, its application on two complex

configurations that are typical of the industrial problems of EDF will be tested: first the case of a subsonic confined cavity and second the case of an abruptly expanded transonic flow. The simulations can be validated with available experimental data. In particular, the acoustic coupling of self-sustained oscillation and duct resonance modes is to be considered in this work.

Organization of thesis

The thesis is organized as follows. First, the numerical algorithm is explained in detail and the chosen numerical schemes are detailed. The implemented shock-capturing filter is discussed. The overset-grid approach is explained and some performance aspects of the parallelized solver are given.

In the second chapter, classical validation test cases are presented. Those test cases, involving the diffraction of a monopolar pressure source by a cylinder, the convection of an inviscid vortex, the 1-D shock/sound interaction problem in a convergent divergent nozzle, the 1-D shock/entropy wave interaction problem, a 2-D compressible plane Couette flow, a low-Reynolds number flow and the computation of a 3-D shock tube, are reported.

In the third chapter, a first industrial application is presented. The configuration consists in a low Mach number flow over a ducted cavity. The flow at high Reynolds number is computed in 3-D and compared to available experimental data. In order to demonstrate the numerical evidence of the coupling mechanism, a series of computations with different Mach numbers are carried out. For particular values of the incoming velocity, the amplification of the pressure is maximum, showing the coupling of the cavity modes and the duct modes.

In chapter four, the sudden expansion of a transonic flow is computed for different pressure ratios. The study consists first in a computation of a pressure ratio where the flow is entirely supersonic and features a system of crossing oblique shocks. Then, the influence of the pressure ratio on the flow is examined. Finally, a configuration is presented where the oscillations of the shock are coupled with longitudinal duct modes.

Chapter 1

Governing equations and numerical algorithm

1.1 Governing equations

The governing equations used in this work are the curvilinear Euler and Navier-Stokes equations, written in conservative form. In this section, the derivation is first established for the Euler equations. The derivation of the curvilinear Navier-Stokes equations is given in section 1.7.

The system of equations can be derived starting from the Euler equations written in Cartesian coordinates

$$\frac{\partial \mathbf{U}}{\partial t} + \frac{\partial \mathbf{E}}{\partial x} + \frac{\partial \mathbf{F}}{\partial y} + \frac{\partial \mathbf{G}}{\partial z} = 0. \tag{1.1}$$

The unknown vector $\mathbf{U}$ contains the conservative variables

$$\mathbf{U} = \begin{pmatrix} \rho \\ \rho u \\ \rho v \\ \rho w \\ \rho e_t \end{pmatrix},$$

where ρ is the density, u, v and w are the velocity components in x, y and z-direction and ρe_t is the specific total energy. For a perfect gas, ρe_t is defined such as

$$\rho e_t = \frac{p}{\gamma - 1} + \frac{1}{2}\rho(u^2 + v^2 + w^2),$$

where γ is the ratio of specific heats and p designates the pressure. The vectors $\mathbf{E}$, $\mathbf{F}$, $\mathbf{G}$ contain the Eulerian flux terms

$$\mathbf{E} = \begin{pmatrix} \rho u \\ \rho u^2 + p \\ \rho uv \\ \rho uw \\ (\rho e_t + p)u \end{pmatrix}, \mathbf{F} = \begin{pmatrix} \rho v \\ \rho vu \\ \rho v^2 + p \\ \rho vw \\ (\rho e_t + p)v \end{pmatrix}, \mathbf{G} = \begin{pmatrix} \rho w \\ \rho wu \\ \rho wv \\ \rho w^2 + p \\ (\rho e_t + p)w \end{pmatrix}. \tag{1.2}$$

In the following, the coordinate transformation of the Euler equations (1.1) from Cartesian coordinates (x, y, z) to curvilinear coordinates (ξ, η, ζ) is sketched. Only time-invariant grids are considered in this work resulting in curvilinear coordinates which are only functions of (x, y, z):

$$\tau \equiv t,\ \xi = \xi(x, y, z),\ \eta = \eta(x, y, z),\ \zeta = \zeta(x, y, z). \tag{1.3}$$

Further details can be found in the work of Vinokur [136] and Pulliam and Steger [102].

Chain rule expansions are used to represent the Cartesian derivatives in terms of the curvilinear derivatives

$$\begin{bmatrix} \partial_x \\ \partial_y \\ \partial_z \end{bmatrix} = \begin{bmatrix} \xi_x & \eta_x & \zeta_x \\ \xi_y & \eta_y & \zeta_y \\ \xi_z & \eta_z & \zeta_z \end{bmatrix} \begin{bmatrix} \partial_\xi \\ \partial_\eta \\ \partial_\zeta \end{bmatrix}. \tag{1.4}$$

Solving the metric equations leads to the following expressions:

$$\begin{aligned} \hat{\xi}_x &= y_\eta z_\zeta - y_\zeta z_\eta, \quad \hat{\eta}_x = y_\zeta z_\xi - y_\xi z_\zeta, \quad \hat{\zeta}_x = y_\xi z_\eta - y_\eta z_\xi, \\ \hat{\xi}_y &= z_\eta x_\zeta - z_\zeta x_\eta, \quad \hat{\eta}_y = z_\zeta x_\xi - z_\xi x_\zeta, \quad \hat{\zeta}_y = z_\xi x_\eta - z_\eta x_\xi, \\ \hat{\xi}_z &= x_\eta y_\zeta - x_\zeta y_\eta, \quad \hat{\eta}_z = x_\zeta y_\xi - x_\xi y_\zeta, \quad \hat{\zeta}_z = x_\xi y_\eta - x_\eta y_\xi, \end{aligned} \tag{1.5}$$

where $\hat{\xi}_x = \xi_x/J$, $\hat{\xi}_y = \xi_y/J$, ... and J stands for the determinant of the transformation Jacobian matrix that is determined using

$$\frac{1}{J} = x_\xi y_\eta z_\zeta + x_\zeta y_\xi z_\eta + x_\eta y_\zeta z_\xi - x_\xi y_\zeta z_\eta - x_\eta y_\xi z_\zeta - x_\zeta y_\eta z_\xi.$$

Applying the transformation (1.4) to the governing equations (1.1), the weak conservation form of the curvilinear equations is obtained:

$$\mathbf{U}_t + \xi_x \mathbf{E}_\xi + \eta_x \mathbf{E}_\eta + \zeta_x \mathbf{E}_\zeta + \xi_y \mathbf{F}_\xi + \eta_y \mathbf{F}_\eta + \zeta_y \mathbf{F}_\zeta + \xi_z \mathbf{G}_\xi + \eta_z \mathbf{G}_\eta + \zeta_z \mathbf{G}_\zeta = 0.$$

The strong conservation form is recovered by dividing by the Jacobian J and by using the product rule. For example we have:

$$\hat{\xi}_x \mathbf{E}_\xi = (\hat{\xi}_x \mathbf{E})_\xi - (\hat{\xi}_x)_\xi \mathbf{E}.$$

Thus the Euler equations become for curvilinear coordinates

$$\begin{aligned} \frac{1}{J}\mathbf{U}_t + (\hat{\xi}_x \mathbf{E} + \hat{\xi}_y \mathbf{F} + \hat{\xi}_z \mathbf{G})_\xi + (\hat{\eta}_x \mathbf{E} + \hat{\eta}_y \mathbf{F} + \hat{\eta}_z \mathbf{G})_\eta + (\hat{\zeta}_x \mathbf{E} + \hat{\zeta}_y \mathbf{F} + \hat{\zeta}_z \mathbf{G})_\zeta \\ + \mathbf{E}\left[(\hat{\xi}_x)_\xi + (\hat{\eta}_x)_\eta + (\hat{\zeta}_x)_\zeta\right] + \mathbf{F}\left[(\hat{\xi}_y)_\xi + (\hat{\eta}_y)_\eta + (\hat{\zeta}_y)_\zeta\right] + \mathbf{G}\left[(\hat{\xi}_z)_\xi + (\hat{\eta}_z)_\eta + (\hat{\zeta}_z)_\zeta\right] = 0. \end{aligned} \tag{1.6}$$

The terms in brackets are known as the metric invariants of the transformation. If the equations for the metric relations (1.5) are introduced, they vanish and the strong conservation form of the governing equations is finally derived:

$$\frac{\partial \hat{\mathbf{U}}}{\partial t} + \frac{\partial \hat{\mathbf{E}}}{\partial \xi} + \frac{\partial \hat{\mathbf{F}}}{\partial \eta} + \frac{\partial \hat{\mathbf{G}}}{\partial \zeta} = 0, \tag{1.7}$$

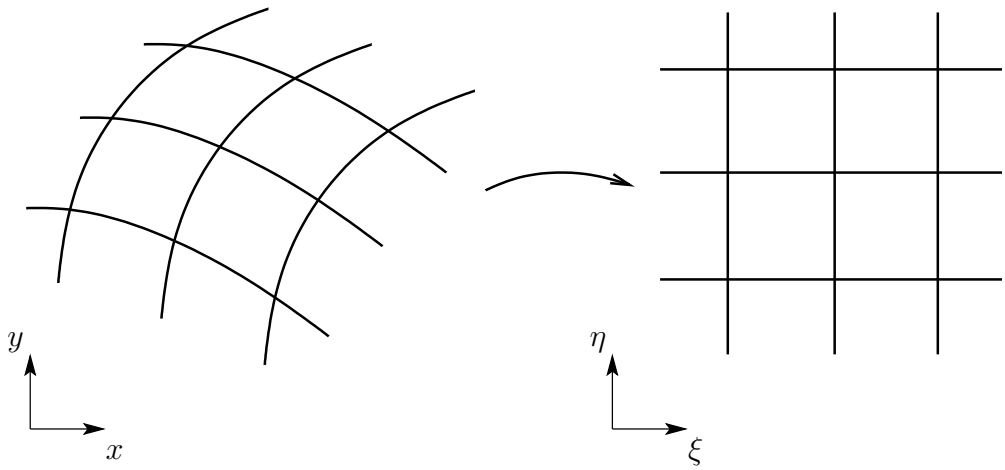

Figure 1.1: 2-D transformation from Cartesian coordinates (x, y) in the physical domain to curvilinear coordinates (ξ, η) in the computational domain.

The unknown vector $\hat{\mathbf{U}} = \mathbf{U}/J$ contains the conservative variables weighted by the inverse of the Jacobian, proportional to the volume of a grid cell in 3-D. The new flux vectors $\hat{\mathbf{E}}$, $\hat{\mathbf{F}}$, $\hat{\mathbf{G}}$ contain the Eulerian flux terms

$$\hat{\mathbf{E}} = \frac{1}{J}\begin{pmatrix} \rho U \\ \rho U u + p\xi_x \\ \rho U v + p\xi_y \\ \rho U w + p\xi_z \\ (\rho e_t + p)U \end{pmatrix}, \hat{\mathbf{F}} = \frac{1}{J}\begin{pmatrix} \rho V \\ \rho V u + p\eta_x \\ \rho V v + p\eta_y \\ \rho V w + p\eta_z \\ (\rho e_t + p)V \end{pmatrix}, \hat{\mathbf{G}} = \frac{1}{J}\begin{pmatrix} \rho W \\ \rho W u + p\zeta_x \\ \rho W v + p\zeta_y \\ \rho W w + p\zeta_z \\ (\rho e_t + p)W \end{pmatrix}.$$

The quantities U, V, W are the contravariant components of the velocity, defined by

$$U = \xi_x u + \xi_y v + \xi_z w, \quad V = \eta_x u + \eta_y v + \eta_z w \quad \text{and} \quad W = \zeta_x u + \zeta_y v + \zeta_z w.$$

The resolution of the Euler equations on a curvilinear grid is then similar to the resolution of the equations on Cartesian mesh. The computation of the flux terms is more computationally demanding, as the contravariant velocities have to be computed first. The grid spacing in the computational domain is taken uniform with $\Delta\xi = 1$, $\Delta\eta = 1$ and $\Delta\zeta = 1$.

1.2 Spatial Differentiation

The inviscid non-linear flux terms govern the propagation of acoustic waves and their interaction with the aerodynamic field. In aeroacoustics, acoustic waves are propagated over long distances that requires low dispersion and low dissipation errors of the numerical scheme. This makes the use of high-order accurate schemes necessary.

Many high-order accurate schemes have been proposed in the literature for the purpose of CAA and LES. An overview on high-order accurate schemes can be found in the review article of Ekaterinaris [50]. Either based on the integral form or on the differential form of the Euler equations, two approaches can be found in the literature: the finite-volume and the finite-difference approaches.

The finite-volume approach is based on the integral form of the Euler equations and the flow field is computed via surface integrals of the fluxes through a control volume. Finite-volume methods are used in commercial CFD codes because they can be applied to unstructured grids and are by construction conservative. Traditionally finite-volume methods are low-order accurate. In the last decade, high-order accurate finite volume-approaches have been developed. For example Barth *et al.* [13] pioneered the use of an arbitrary high-order reconstruction method to compute the flux at the control volume boundary. Other methods like the Discontinuous Galerkin (DG) methods that have been developed by Cockburn *et al.* [36] shows promise for high-resolution simulations on fully unstructured meshes. Another method based on the finite-element framework are spectral element methods developed recently by Wang [141]. ADER (Arbitrary high-order schemes using DERivatives) finite-volume methods developed by Schwartzkopff *et al.* [115] and DG methods have been proposed in the literature [49]. Although these methods allows a maximum flexibility in grid generation, high-order finite volume methods on unstructured grids remain computationally intensive and very few 3-D applications, in general at low Reynolds numbers, can be found in the literature [50].

The finite-difference approach is based on the differential form of the Euler equations. Those methods do not require a reconstruction of the flux around a control volume and the derivatives are approximated by finite-differences. High-order accuracy can be obtained very easily by enlarging the finite-difference stencil and by eliminating low-order terms by a certain choice of the stencil coefficients. As large stencils of grid points are needed to reconstruct the derivatives with high accuracy, the finite-difference approach is in general restricted to structured grids with reduced grid flexibility. For non-linear problems the finite-difference approach allows to access to high Reynolds number applications and are often used for DNS and LES. In combination with high-order overset-grid approach, complex geometries can be taken into account and the finite-difference method has been used in this work.

Several finite-difference based schemes exist in the literature. Among those the compact schemes of Lele [86], the Dispersion Relation Preserving (DRP) scheme of Tam and Webb [128], high-order implicit compact MacCormack-type scheme such as developed by Hixon *et al.* [70] and the explicit 11-point optimized explicit finite-difference scheme of Bogey and Bailly [30] can be mentioned at this point.

In order to simplify the domain decomposition in a parallel approach, the explicit centered 11-point finite-difference scheme developed by Bogey and Bailly [30] has been implemented in this work. This scheme is optimized in wave number space and is able to resolve accurately perturbations with only four points per wavelength. For example, the derivative of $\hat{\mathbf{E}}$ in ξ-direction at (i,j,k) is computed using the expression

$$\left.\frac{\partial \hat{\mathbf{E}}}{\partial \xi}\right|_{i,j,k} = \sum_{r=1}^{5} a_r (\hat{\mathbf{E}}|_{i+r,j,k} - \hat{\mathbf{E}}|_{i-r,j,k}).$$

The coefficients a_r of the scheme are given in Table 1.1.

$$
\begin{aligned}
a_0 &= 0. \\
a_1 &= 0.872756993962667 \\
a_2 &= -0.286511173973333 \\
a_3 &= 9.032000128000002 \times 10^{-2} \\
a_4 &= -2.077940582400000 \times 10^{-2} \\
a_5 &= 2.484594688000000 \times 10^{-3}
\end{aligned}
$$

Table 1.1: Coefficients of the interior centered spatial differencing scheme [30].

1.3 Time integration scheme

A low-storage explicit Runge-Kutta scheme has been implemented in the solver to update the flow variables at the new time instance $\hat{\mathbf{U}}^{n+1}$. The algorithm can be summarized as follows:

$$
\begin{aligned}
\hat{\mathbf{U}}^{(0)} &= \hat{\mathbf{U}}^{n}, \\
\hat{\mathbf{U}}^{(l)} &= \hat{\mathbf{U}}^{n} - \alpha_l \, \Delta t \, \boldsymbol{\mathcal{F}}(\hat{\mathbf{U}}^{(l-1)}) \quad \text{for } l = 1, ..., p, \\
\hat{\mathbf{U}}^{n+1} &= \hat{\mathbf{U}}^{(p)},
\end{aligned}
$$

where $\hat{\mathbf{U}}^{(l)}$ contains the flow variables computed at the sub stage l, α_l are the coefficients of the Runge Kutta scheme given in Table 1.3, Δt is the time step and $\boldsymbol{\mathcal{F}}$ is given by

$$
\frac{\partial \hat{\mathbf{U}}}{\partial t} + \boldsymbol{\mathcal{F}}(\hat{\mathbf{U}}) = 0.
$$

	RK(p=4)	RKo(p=6)
α_1	1/4	0.11797990162882
α_2	1/3	0.18464696649448
α_3	1/2	0.24662360430959
α_4	1	0.33183954273562
α_5	–	1/2
α_6	–	1

Table 1.2: Coefficients α_l of standard (RK) and optimized Runge Kutta (RKo) scheme [30].

In this work, either four-stage or an optimized six-stage Runge-Kutta scheme such as proposed by Bogey and Bailly [30] are used. The six-stage scheme has been optimized in the frequency domain in order to reduce the dispersion and dissipation errors. Both schemes are fourth-order accurate for linear problems and are second-order for non-linear problems.

1.4 Selective filtering

Centered finite-difference schemes have no built-in dissipation such as upwind schemes. Non physical grid-to-grid oscillations that are generated at boundary conditions, geometrical singularities, non-linear energy cascade and strong gradients such as shocks can accumulate in the computational domain,

ending up with a divergence of the solution. In order to ensure numerical stability, an explicit 11-point low-pass filter has been implemented. The filter, optimized in the wave-number space [30], removes all high frequency waves resolved with less then 4 points per wavelength. Thus the cut-off frequency matches with the maximum resolution of the finite-difference schemes. The filter is separately applied once after every time iteration in each coordinate direction. The algorithm for filtering in ξ-direction can be written such as

$$\mathbf{W}_{\mathbf{p}i,j,k}^{d} = \mathbf{W}_{\mathbf{p}i,j,k} - \sigma(\mathbf{D}_\xi + \mathbf{D}_\eta + \mathbf{D}_\zeta)$$

where

$$\mathbf{D}_\xi = \sum_{r=-5}^{5} d_r \mathbf{W}_{\mathbf{p}i+r,j,k},\ \mathbf{D}_\eta = \sum_{r=-5}^{5} d_r \mathbf{W}_{\mathbf{p}i,j+r,k},\ \mathbf{D}_\zeta = \sum_{r=-5}^{5} d_r \mathbf{W}_{\mathbf{p}i,j,k+r}.$$

The filtering coefficient σ has to be chosen between 0 and 1. If not otherwise indicated a coefficient of $\sigma = 0.2$ is used. The filter is applied to the primitive variables $\mathbf{W} = (\rho, u, v, w, p)^T$. The stencil coefficients $d_r = d_{-r}$ are given in Table 1.3.

d_0	=	0.2150448841109084
d_1	=	-0.1877728835894673
d_2	=	0.1237559487873421
d_3	=	$-5.922757557574387 \times 10^{-2}$
d_4	=	$1.872160915720372 \times 10^{-2}$
d_5	=	$-2.999540834788787 \times 10^{-3}$

Table 1.3: Coefficients of the centered filtering [30] for interior points.

In order to preserve accuracy near the wall boundaries, the optimized 11-point non-centered finite-difference schemes such as developed by Berland *et al.* [21] are used. The associated non-centered filters exhibit stability problems, when the mesh is stretched, contains discontinuities or for strongly compressible flows. Centered filters with reduced order can be therefore optionally applied at boundary conditions.

1.5 Computation of the metrics

The solution of the transformed Navier-Stokes equations require the evaluation of the Jacobian matrix $\mathbf{J}$:

$$\mathbf{J} = \frac{\partial(\xi, \eta, \zeta)}{\partial(x, y, z)} = \begin{pmatrix} \xi_x & \eta_x & \zeta_x \\ \xi_y & \eta_y & \zeta_y \\ \xi_z & \eta_z & \zeta_z \end{pmatrix},$$

and its determinant J. Only the mapping function $\mathbf{x} = (\mathbf{x}, \mathbf{y}, \mathbf{z})^{\mathbf{T}} = \mathbf{x}(\xi, \eta, \zeta)$ is *a priori* known and therefore only its inverse $\mathbf{J}^{-1}$ can be determined directly from $\mathbf{x}$. The Jacobian matrix $\mathbf{J}$ can be computed from equation (1.5). When solving the transformed Navier-Stokes equations grid with finite-difference schemes, Pulliam and Steger [101] and Thomas and Lombard [130] highlighted then

the following relations,

$$\begin{aligned}(\hat{\xi}_x)_\xi + (\hat{\eta}_x)_\eta + (\hat{\zeta}_x)_\zeta = 0,\\ (\hat{\xi}_y)_\xi + (\hat{\eta}_y)_\eta + (\hat{\zeta}_y)_\zeta = 0,\\ (\hat{\xi}_z)_\xi + (\hat{\eta}_z)_\eta + (\hat{\zeta}_z)_\zeta = 0,\end{aligned} \tag{1.8}$$

must be verified numerically to ensure an effective conservative form. The metric relations are the first part of the Geometric Conservation Law (GCL). An additional equation comes into play when the mesh is time-variant. The equation writes [130]

$$J_t + (\hat{\xi}_t)_\xi + (\hat{\eta}_t)_\zeta + (\hat{\zeta}_t)_\zeta = 0.$$

However being evaluated with finite-differences, the first metric relation becomes for example:

$$(\hat{\xi}_x)_\xi + (\hat{\eta}_x)_\eta + (\hat{\zeta}_x)_\zeta = (y_\eta z_\zeta)_\xi - (y_\zeta z_\eta)_\xi + (y_\zeta z_\xi)_\eta - (y_\xi z_\zeta)_\eta + (y_\xi z_\eta)_\zeta - (y_\eta z_\xi)_\zeta \neq 0$$

due to the numerical failure of the product rule as noticed by Hixon [69]. Therefore Thomas and Lombard [130] proposed to compute the metric coefficients in a conservative form such as:

$$\begin{aligned}\hat{\xi}_x &= (y_\eta z)_\zeta - (y_\zeta z)_\eta, \quad \hat{\eta}_x = (y_\zeta z)_\xi - (y_\xi z)_\zeta, \quad \hat{\zeta}_x = (y_\xi z)_\eta - (y_\eta z)_\xi,\\ \hat{\xi}_y &= (z_\eta x)_\zeta - (z_\zeta x)_\eta, \quad \hat{\eta}_y = (z_\zeta x)_\xi - (z_\xi x)_\zeta, \quad \hat{\zeta}_y = (z_\xi x)_\eta - (z_\eta x)_\xi,\\ \hat{\xi}_z &= (x_\eta y)_\zeta - (x_\zeta y)_\eta, \quad \hat{\eta}_z = (x_\zeta y)_\xi - (x_\xi y)_\zeta, \quad \hat{\zeta}_z = (x_\xi y)_\eta - (x_\eta y)_\xi.\end{aligned} \tag{1.9}$$

This form is analytically identical to the metric terms in equations (1.5). Substituting this in the first metric invariant gives

$$(\hat{\xi}_x)_\xi + (\hat{\eta}_x)_\eta + (\hat{\zeta}_x)_\zeta = (y_\eta z)_{\zeta\xi} - (y_\zeta z)_{\eta\xi} + (y_\zeta z)_{\xi\eta} - (y_\xi z)_{\zeta\eta} + (y_\xi z)_{\eta\zeta} - (y_\eta z)_{\xi\zeta} = 0$$

because the order of differentiation can be interchanged numerically as also explained by Hixon [69]. This is demonstrated by using a ξ-derivative and η-derivative defined by

$$(x_{i,j})_\xi = \sum_{k=k_s}^{k_e} a_k x_{i+k,j}, \quad (x_{i,j})_\eta = \sum_{l=l_s}^{l_e} b_l x_{i,j+l},$$

where k_s, l_s and k_e, l_e denote the number points on the left and right side of the stencil respectively and a_k and b_l the stencil coefficients. Note that the index for the third direction is omitted. The quantity $x_{\xi\eta}$ is computed as:

$$\begin{aligned}[(x_\xi)_\eta]_{i,j} &= \sum_{l=l_s}^{l_e} b_l \left(\sum_{k=k_s}^{k_e} a_k x_{i+k,j+l} \right) && (1.10)\\ &= \sum_{l=l_s}^{l_e} \sum_{k=k_s}^{k_e} b_l a_k x_{i+k,j+l} && (1.11)\\ &= \sum_{k=k_s}^{k_e} \sum_{l=l_s}^{l_e} a_k b_l x_{i+k,j+l} && (1.12)\\ &= [(x_\eta)_\xi]_{i,j} && (1.13)\end{aligned}$$

This holds as long as the ξ derivative stencil has no η dependence and vice-versa. Near boundaries along $\eta = \text{const.}$, for instance, the η derivative stencils vary in η-direction but not in ξ-direction and the cancellation of the metric relations are conserved.

For 2-D problems the cancellation of the metric invariants is always ensured numerically. For 3-D problems, all metric derivatives must be computed using the same differencing stencils. For example when working with Mac Cormack schemes using a forward based and backward based stencil, the metrics have to be computed twice using a forward and a backward based stencil respectively. The method fails also for finite-difference schemes based on a Weighted Essentially Non-Oscillatory (WENO) reconstruction. As WENO schemes adapt the computational stencil for the derivative approximation locally to the flow field, a numerical cancellation of the metric invariants can not be ensured. Implementations of the WENO schemes in a more computationally expensive finite-volume approach are therefore more common and recommended.

1.6 Shock-capturing filtering

In regions with strong shocks, additional numerical dissipation is introduced in order to avoid the divergence of the numerical solution and to reduce the overshoots that occurs around the shock. Several shock-capturing schemes have been developed for that purpose. Among those the Jameson scheme [73], the Total Variation Diminishing (TVD) [65], Monotone Upstream-Centered Scheme for Conservation Laws (MUSCL) [135] and (Weighted) Essentially Non-Oscillatory ((W)ENO) [74] schemes are often used for aeronautical applications.

However for aeroacoustic problems classical shock-capturing schemes are less suitable due to an excessive dissipation and dispersion error. Also for Large-Eddy Simulations, those schemes written in the classical form are too dissipative and mask the diffusion provided by the subgrid scale model [55]. In the last decade, much work has been done to adapt shock-capturing schemes for the purpose of LES and CAA of transonic flows. Most of the approaches are based on a local increase of dissipation provided by the shock-capturing scheme, whereas dissipation is minimized in smooth regions. This makes the detection of the shock location to be a very important point for LES and CAA of transonic and supersonic flows.

In this section, first some recent developments of shock-capturing schemes towards CAA and LES found in the literature are summarized. Second, the implementation of the shock-capturing scheme used in the present work is explained. Third, the shock detection procedure is described.

1.6.1 Shock-capturing for LES and CAA

Originally Jameson *et al.* [73] proposed to discretize the Euler equations using a second-order finite-volume scheme. Second- and fourth-order dissipation terms with coefficients that depend on the local pressure gradient are added on the right hand side of the equations. The scheme writes in 1-D as

$$\left.\frac{\partial \mathbf{U}}{\partial t}\right|_i + \boldsymbol{\mathcal{F}}(\mathbf{U})|_i = -\frac{(\mathbf{D}_{i+\frac{1}{2}} - \mathbf{D}_{i-\frac{1}{2}})}{\Delta x},$$

where $\boldsymbol{\mathcal{F}}(\mathbf{U})|_i$ is the discretized flux term and the terms on the right have the form:

$$\mathbf{D}_{i+\frac{1}{2}} = \left[\epsilon^{(2)}_{i+\frac{1}{2}}(\mathbf{U}_{i+1} - \mathbf{U}_i) - \epsilon^{(4)}_{i+\frac{1}{2}}(\mathbf{U}_{i+2} - 3\mathbf{U}_{i+1} + 3\mathbf{U}_i - \mathbf{U}_{i-1})\right]$$

The weights $\epsilon^{(2)}_{i+\frac{1}{2}}$, $\epsilon^{(4)}_{i+\frac{1}{2}}$ of the smoothing terms are functions of the considered equations and are determined using a smoothness detector applied to the pressure field:

$$\Phi_i = \frac{|p_{i+1} - 2p_i + p_{i-1}|}{|p_{i+1} + 2p_i + p_{i-1}|}. \tag{1.14}$$

The weighting functions are defined as

$$\epsilon^{(2)}_{i+\frac{1}{2}} = \kappa^{(2)} \max(\Phi_i, \Phi_{i+1})$$

and

$$\epsilon^{(4)}_{i+\frac{1}{2}} = \max\left[0, \left(\kappa^{(4)} - \epsilon^{(2)}_{i+\frac{1}{2}}\right)\right],$$

where $\kappa^{(4)}$ and $\kappa^{(2)}$ are adjustable problem dependent values. In smooth regions of the flow, the smoothness detector is of second-order and the low-order dissipation is switched off thanks to $\epsilon^{(2)}_{i+\frac{1}{2}}$. In regions of strong pressure gradients, the smoothness detector reduces to first-order and the low-order dissipation dominates.

It has been observed by Jameson [73] that the low-order dissipation terms do not avoid some small high-frequency oscillations, which prevent the complete convergence of the solution to steady state. The fourth-order dissipation term is therefore introduced, which is switched on through the whole computational domain where the solution is smooth. In regions with strong gradients, the fourth-order dissipation term has shown to generate overshoots that are associated to the Gibbs phenomenon and are typical for high-order finite-difference schemes. This term is therefore switched off in shock regions thanks to $\epsilon^{(4)}_{i+\frac{1}{2}}$.

Following the idea of a locally introduced dissipation, Yee *et al.* [142] proposed to isolate the dissipative part of classical shock-capturing schemes and to apply it like a filtering operator in regions with strong non-linearities. They used those characteristic based filters in combination with high-order centered finite-difference schemes. Thus, in smooth regions where no non-linear filtering is applied, the accuracy of the high-order schemes can be maintained. Yee *et al.* [142] developed those filters for the TVD, MUSCL and ENO schemes. Garnier *et al.* [56, 57] applied characteristic based filter based on WENO schemes successfully for shock/turbulence and shock/boundary layer interactions.

Visbal and Gaitonde [137] developed a hybrid compact-Roe method, where a compact finite-difference scheme is used in smooth regions. In shock regions, the compact scheme is replaced by a third-order MUSCL based upwind-biased Roe scheme. The scheme performs very well in various test cases and has been used for a LES of a supersonic flow over a compression ramp [106].

Tam and Shen [125] proposed to use the DRP scheme [128] for the simulation of a non-linear acoustic pulse and to use a variable damping algorithm which introduces more numerical viscosity in regions with strong gradients. The shock regions are detected using $u_{\text{stencil}} = |u_{\max} - u_{\min}|$; the difference between the maximum velocity, $u_{\max}$, and the minimum velocity, $u_{\min}$, in the stencil. The

numerical viscosity is provided by a 7 point centered filter weighted by $u_{\text{stencil}}/R_{\text{stencil}}/\Delta x$, where the constant stencil Reynolds number $R_{\text{stencil}} \approx 0.06$ has been introduced.

Kim and Lee [78] have shown that this formulation does not fulfill conservativity and explain why the shock propagation velocity is not well predicted. Basing on the lecture notes of Leveque [88], they recasted the centered selective filter into a conservative form similar to the Jameson filter. Details about this can be found in appendix A. Additionally, Kim and Lee [78] combined this filter with the low-order shock-capturing term of the Jameson scheme. Furthermore, they proposed a self-adapting procedure determining automatically the problem depending parameters $\epsilon^{(2)}$ and $\epsilon^{(4)}$ of the original Jameson scheme. The scheme has been validated for 1-D and multi-dimensional CAA benchmark test cases.

Except the Jameson scheme, shock-capturing schemes exploit the hyperbolic nature of the Euler equations, making them more suitable for flows at very high Mach numbers. On the other hand, it is difficult to quantify the error as a function of the wave-number such as it is often done with schemes dedicated to LES and CAA. The error made by the Jameson scheme, that adds explicit selective smoothness terms to the governing equations, can be quantified using a linear error analysis. Furthermore, the Jameson type schemes are very simple in implementation and are computationally very efficient. The method used here follows the Jameson-type dissipation model and is similar to the dissipation model proposed by Kim and Lee [78].

1.6.2 Implementation of the shock-capturing filter

A shock-capturing filter based on the adaptive non-linear artificial dissipation model of Kim and Lee [78] has been implemented in the solver as follows. Only the low-order shock-capturing filter is applied to the conservative variables, that have already been filtered using the selective filter presented in section 1.4. The filtering operator writes in conservative form:

$$\hat{\mathbf{U}}_{i,j,k} = \hat{\mathbf{U}}_{i,j,k} - \Delta t(\hat{\mathbf{D}}_{i+\frac{1}{2},j,k} - \hat{\mathbf{D}}_{i-\frac{1}{2},j,k}),$$

where

$$\hat{\mathbf{D}}_{i+\frac{1}{2},j,k} = \frac{\Delta|\lambda|^{\text{stencil}}_{i+\frac{1}{2},j,k}}{\frac{1}{2}(J_{i+1,j,k} + J_{i,j,k})}\ \epsilon^{(2)}_{i+\frac{1}{2},j,k}\ \Delta t\left(\mathbf{U}_{i+1,j,k} - \mathbf{U}_{i,j,k}\right).$$

Similar to Swanson and Turkel [121], Kim and Lee uses the stencil eigenvalue $\Delta|\lambda|^{\text{stencil}}_{i+1/2,j,k}$ that denotes the difference between the maximum and the minimum eigenvalue

$$|\lambda|_{i,j,k} = \left(|U| + c\sqrt{\xi_x^2 + \xi_y^2 + \xi_z^2}\right)_{i,j,k}$$

within a stencil of variable size. The quantities U and c designate the contravariant velocity $U = u\xi_x + v\xi_y + w\xi_z$ and the speed of sound respectively. According to Kim and Lee, $\Delta|\lambda|^{\text{stencil}}_{i+1/2,j,k}$ is computed using a stencil width of 7 points:

$$\Delta|\lambda|^{\text{stencil}}_{i+\frac{1}{2},j,k} = \max_{m=-2}^{3}\left(|\lambda|_{i+m,j,k}\right) - \min_{m=-2}^{3}\left(|\lambda|_{i+m,j,k}\right).$$

In order to maintain the accuracy of the numerical scheme, the second-order filter may only be applied locally in the shock region. This is performed by the adaptive non-linear dissipation function given by

$$\epsilon^{(2)}_{i+1/2,j,k} = \kappa_{j,k} \max_{m=-2}^{3} (\Phi_{i+m,j,k})$$

where $\Phi_{i,j,k}$ is Jameson shock detector defined in equation (1.14) and $\kappa_{j,k}$ is the adaptive control constant. The latter is given by

$$\kappa_{j,k} = \frac{1}{\sigma_{j,k}^{R_{j,k}}}[1 + (\sigma_{j,k} - 1)\ \tanh\,(\frac{\alpha_{j,k}}{\beta_{j,k}} - 1)] \left(\sqrt{\hat{\alpha}_{j,k}\hat{\beta}_{j,k}}\right)^{1+\tanh\,(\sigma_{j,k}-1)},$$

where

$$\sigma_{j,k} = \frac{p^{\max}_{j,k}}{p^{\min}_{j,k}}, \quad \alpha_{j,k} = \frac{\lambda^{\max}_{j,k}}{\lambda^{\min}_{j,k}},$$

$$\beta_{i,j} = \frac{\left(\frac{|\lambda|}{\sqrt{\xi_x^2+\xi_y^2+\xi_z^2}}\right)^{\max}_{j,k}}{\left(\frac{|\lambda|}{\sqrt{\xi_x^2+\xi_y^2+\xi_z^2}}\right)^{\min}_{j,k}},$$

$$R_{j,k} = \frac{\alpha_{j,k} + \beta_{j,k}}{2\alpha_{j,k}\beta_{j,k}}, \quad \hat{\alpha}_{j,k} = \left[\frac{\alpha_{j,k}+1}{\alpha_{j,k}-1}\right]\tanh(\alpha_{j,k}),$$

$$\hat{\beta}_{j,k} = \left[\frac{\beta_{j,k}+1}{\beta_{j,k}-1}\right]\tanh\,(\beta_{j,k}-1)$$

The superscripts min and max are expressed in 3-D as

$$f^{\min}_{j,k} = \min_{i=1}^{i\ \max} f_{i,j,k}, \quad f^{\max}_{j,k} = \max_{i=1}^{i\ \max} f_{i,j,k}.$$

The paper of Kim and Lee [78] lacks in detailed derivations of each term. Following their paper, most of the terms have been implemented on the basis of various numerical tests and flow conditions. The validation of the test cases shows that the self-adapting procedure works well and provides stable and accurate results.

1.6.3 Detection of the shock location

Besides the Jameson-type dissipation switch [73] introduced in equation (1.14), other approaches has been used in the literature. Yee *et al.* [142] use an artificial compression method proposed by Harten (ACM) [64] and Visbal and Gaitonde [137] a WENO-type smoothness criterion based on a weighted sum of a first and second derivative operator that measures the slope and the curvature of the pressure field.

In this work, the shock position is detected by the Jameson sensor. Actually this sensor has shown to be too sensitive to pressure fluctuations. As a consequence, excessive filtering of turbulent structures has been observed by Ducros *et al.* [48] for instance. Those authors developed a modified sensor which is able to separate turbulent fluctuations from shocks. This is done by multiplying the Jameson sensor by a second sensor, that is

$$\Xi_{i,j,k} = \frac{\mathrm{div}(\mathbf{u}_{i,j,k})^2}{\mathrm{div}(\mathbf{u}_{i,j,k})^2 + \mathrm{rot}(\mathbf{u}_{i,j,k})^2},$$

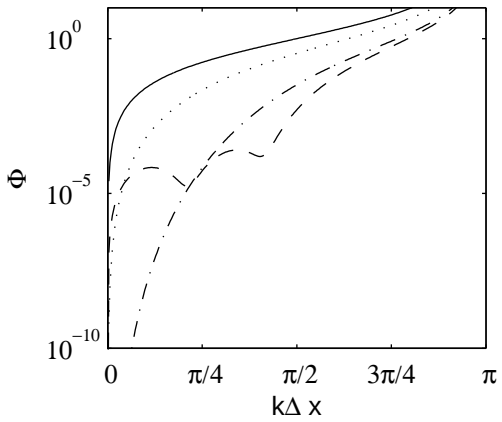

Figure 1.2: Generalized Jameson detector strength Φ_i^ξ of a plane wave $p = \exp(-ikx)$ as a function of the wave number $k\Delta x$ for different orders of the dissipation term: ——— second-order (classical Jameson); · · · · · · · fifth-order, · – · – · – tenth-order, - - - - - 11-point selective dissipation.

where $\mathbf{u}$ the velocity vector containing the Cartesian velocity components. This sensor has been applied in various applications in combination with the Jameson scheme [48] and with characteristic based filters [57]. The computation of the divergence and the rotational field is numerically expensive and is not used in this work.

An improvement of the detection procedure can be achieved by generalizing the Jameson detector using high-order selective filter operators instead of using the second derivative. The generalized Jameson detector can be written as:

$$\Phi^\xi_{i,j,k} = \frac{\left|\sum_{r=-N}^{N} d_r p_{i+r,j,k}\right|}{\left|p_{i,j,k} - \sum_{r=-N}^{N} d_r p_{i+r,j,k}\right|},\quad \Phi^\eta_{i,j,k} = \frac{\left|\sum_{r=-N}^{N} d_r p_{i,j+r,k}\right|}{\left|p_{i,j,k} - \sum_{r=-N}^{N} d_r p_{i,j+r,k}\right|},\quad \Phi^\zeta_{i,j,k} = \frac{\left|\sum_{r=-N}^{N} d_r p_{i,j,k+r}\right|}{\left|p_{i,j,k} - \sum_{r=-N}^{N} d_r p_{i,j,k+r}\right|},$$

where d_r are the coefficients for a filter of arbitrary order $2N$. The detector is first analyzed in 1-D, using a plane wave ansatz $p = \exp(-ikx)$, where k is the wavenumber, which yields:

$$\Phi^\xi_i(k\Delta x) = \frac{\left|\sum_{r=-N}^{N} d_r \exp(-irk\Delta x)\right|}{\left|1 - \sum_{r=-N}^{N} d_r \exp(-irk\Delta x)\right|},$$

where Δx the grid spacing width. Figure 1.2 gives the sensor strength Φ_i^ξ as a function of the wave-number for different filtering operators: the standard second- (classical Jameson filter $N = 1$), fourth-order ($N = 2$) and tenth-order ($N = 5$) ones and the 11-point optimized filter ($N = 5$). Figure 1.2 shows that using the high-order detectors leads to lower values in the low wave-number range whereas, for the high frequencies, the detector behaves as the classical Jameson detector ensuring the shock-capturing property of the scheme. A similar approach has been proposed by Lockard and Morris [90] using only the sixth-order filter operator, without the normalizing term in the denominator.

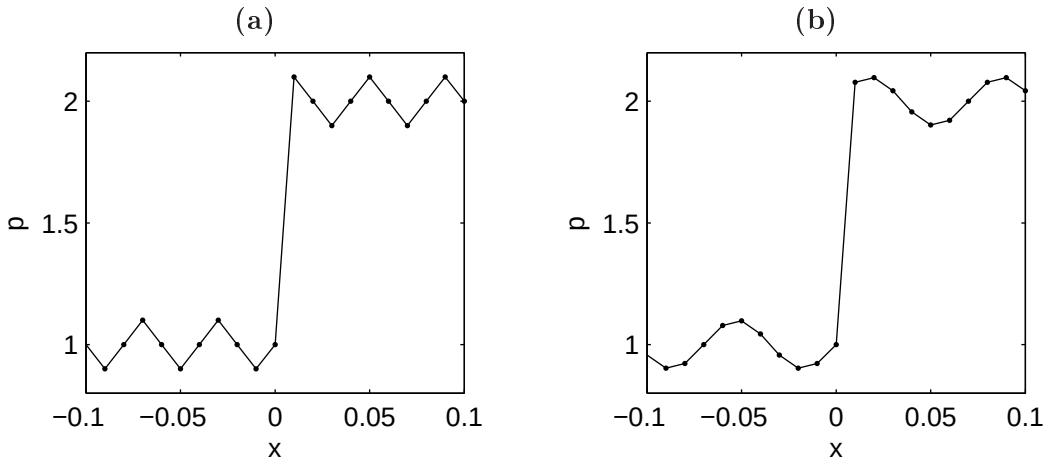

Figure 1.3: Model problem involving a discontinuity and a harmonic signal containing **(a)** high-frequency case (4 points per wave length); **(b)** low-frequency case (7 points per wave length).

In order to study the behavior of the generalized Jameson filter when a discontinuity and linear perturbations are present, the following test problem is considered. A signal of a shock-sound interaction problem is modeled as follows

$$p(x) = \begin{cases} 1 + 0.1 \ \sin(k_l x), & x \leq 0 \\ 2 + 0.1 \ \sin(k_l x), & x > 0. \end{cases}$$

where k_l is the wave number of the linear signal. Two wavenumbers are considered $k_l = \pi/(2\Delta x)$ and $k_l = 2\pi/(7\Delta x)$ corresponding to a wave that contains 4 and 7 grid points respectively. Note that 4 points per wave length is the accuracy limit of the present spatial differencing scheme and is the cut-off wave-length of the optimized low-pass filter. The two signals are plotted in Figure 1.3 **(a)** and **(b)**.

The computed sensor values are given in Figure 1.4 **(a)** and **(b)** respectively. All of the sensors reach their maximum at the shock position. In the linear region the detector value decreases of about one order of magnitude for the classical second-order detector, whereas for the 11-point detector the value drops four orders of magnitude. For the high-frequency case, all detectors have their maximum at the shock location and the curve has a similar shape as for the low-frequency case. The detectors of order 2 and 5 perform very poorly in the linear region. Their magnitude is of the same order as for the shock and would lead to an excessive damping. For the tenth-order filter, a value being one order of magnitude smaller is reported and for the 11-point optimized sensor, the detector is two orders of magnitude smaller, showing the benefit of the optimization. For the high-order filters, the peaks around the discontinuities are slightly more extended but more smooth. This is due to the large extension of the eleven-point stencils, that could be prevented by using compact stencils [86]. As Hixon [71] recommends a smooth introduction of the low-order Jameson dissipation term [71], this is rather a favorable property of the high-order detectors.

The behavior of the modified Jameson filter is studied in the following when shocks and turbulent perturbations are present. Since a vortex features a minimum in pressure located in its core, the classical second-order detector does not well distinguish a vortex and a shock wave as Ducros *et al.*

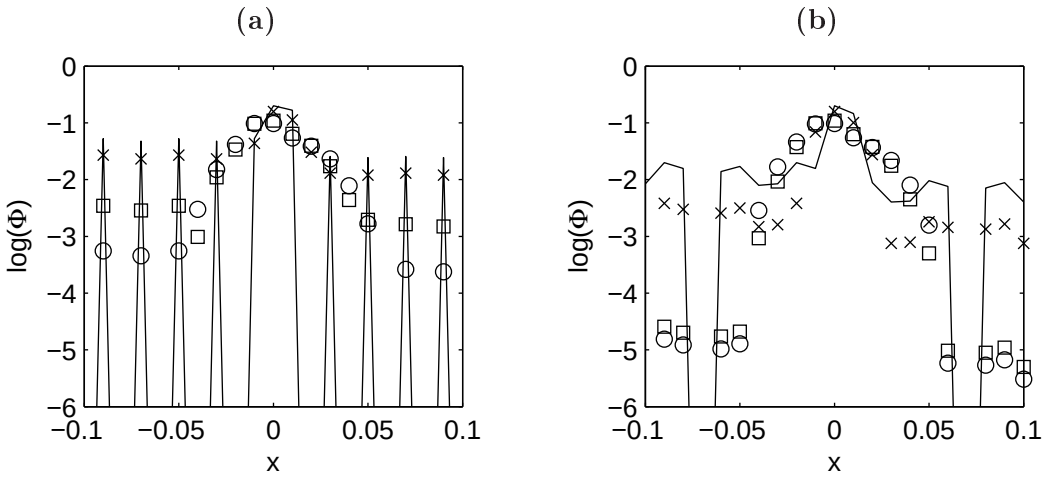

Figure 1.4: Computed detector Φ_i^ξ values for different filtering order: ——— second-order $N = 1$; $\times$ fourth-order $N = 2$; $\circ$ tenth-order $N = 5$; $\square$ optimized $N = 5$ **(a)** high-frequency case (4 points per wave length); **(b)** low-frequency case (7 points per wave length); See Figure 1.3.

[48] notice. Figure 1.5 **(a)** gives an example of a transonic confined jet such as presented in chapter 4. The flow field is visualized by the contours of the density gradient and exhibits a typical jet-like structure with three shock cells. The jet is attached to the upper wall. The detector strength fields computed using the second-order and 11-point optimized filter are plotted in Figure 1.5 **(b)**-**(e)**. The same trend as for the 1-D case can be observed. The low-order detector identifies regions without shocks as non-linear regions, whereas the high-order detector is limited principally on the shock regions. Even worse, the second-order detector detects instability waves developing in the shear layer, which can influence the development of instabilities seriously.

The modified Jameson detector based on the 11-point selective filter term are tested using 1-D cases such as for the convergent-divergent nozzle and the entropy wave/shock wave interaction in the validation chapter 2. Due to stability and computational limits, the 3-D transonic flow presented in chapter 4 are computed using a sensor with maximum fourth-order dissipation terms.

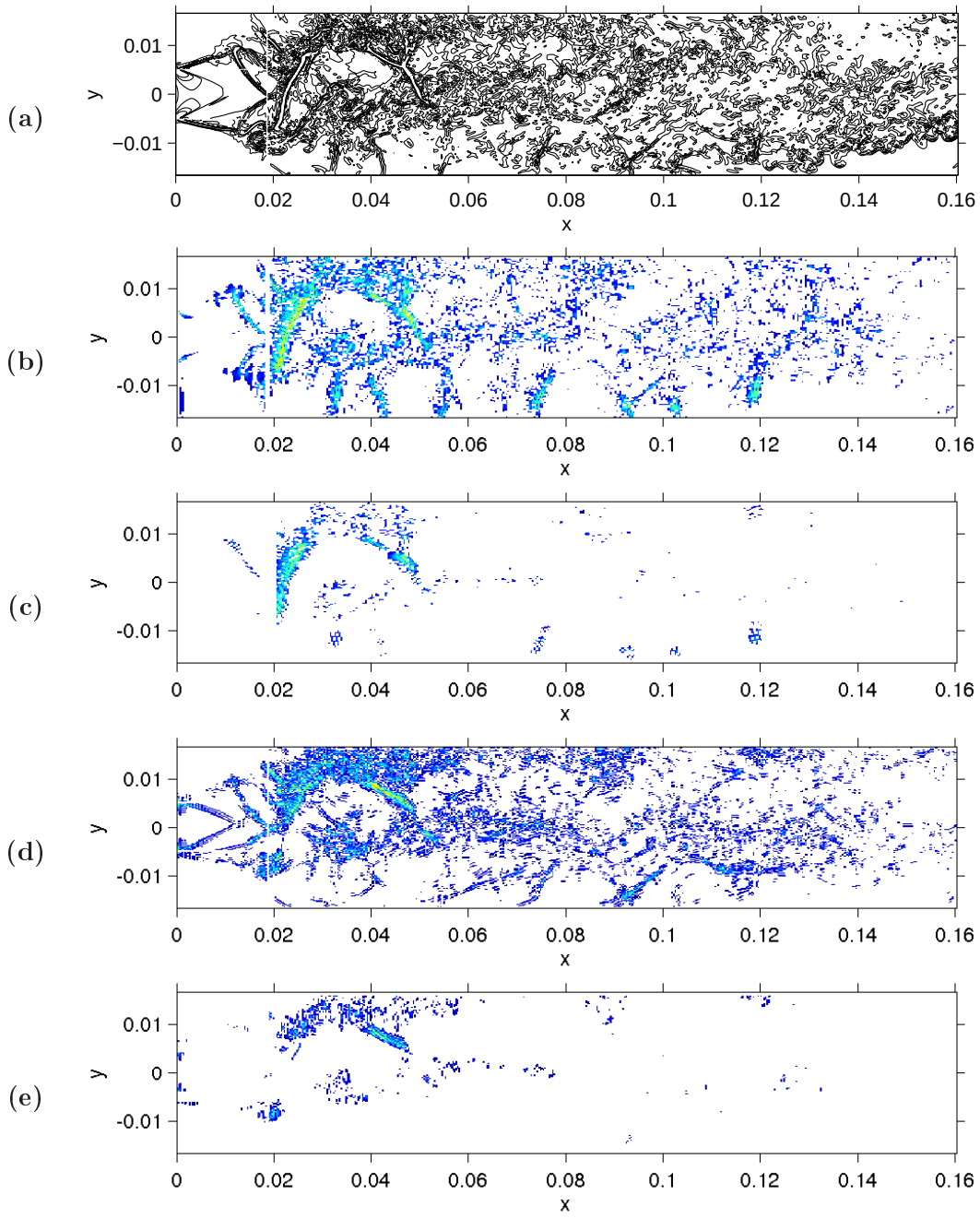

Figure 1.5: Test of generalized Jameson detector applied to a instantaneous pressure field of a flow that contains turbulent fluctuations and shocks. The flow field is visualized in **(a)** by the iso contours of the density gradient $|\nabla_x \rho|$. Detector values $\log(\Phi^{\xi}_{i,j,k})$ computed in i-direction using the classical Jameson detector **(b)** and using detector based on the 11-point optimized filter **(c)**. Detector values $\log(\Phi^{\eta}_{i,j,k})$ computed in j-direction using the classical Jameson detector **(d)** and using the detector based on the 11-point optimized filter **(e)**. Color scales from -5 to 0.

1.7 Consideration of viscous and heat conduction effects

When a viscous fluid is considered, the governing equations are the curvilinear Navier-Stokes equations. In 3-D they write:

$$\begin{aligned}\frac{\partial \hat{\mathbf{U}}}{\partial t} &+ \frac{\partial}{\partial \xi}\left\{\frac{1}{J}\left[\xi_x(\mathbf{E}-\mathbf{E_v})+\xi_y(\mathbf{F}-\mathbf{F_v})+\xi_{\mathbf{z}}(\mathbf{G}-\mathbf{G_v})\right]\right\} \\ &+ \frac{\partial}{\partial \eta}\left\{\frac{1}{J}\left[\eta_x(\mathbf{E}-\mathbf{E_v})+\eta_y(\mathbf{F}-\mathbf{F_v})+\eta_z(\mathbf{G}-\mathbf{G_v})\right]\right\} \\ &+ \frac{\partial}{\partial \zeta}\left\{\frac{1}{J}\left[\zeta_x(\mathbf{E}-\mathbf{E_v})+\zeta_{\mathbf{y}}(\mathbf{F}-\mathbf{F_v})+\zeta_{\mathbf{z}}(\mathbf{G}-\mathbf{G_v})\right]\right\} = 0,\end{aligned}$$

where the inviscid fluxes are given by equation (1.7) and the viscid fluxes write

$$\mathbf{E}_v = \begin{pmatrix} 0 \\ \tau_{xx} \\ \tau_{xy} \\ \tau_{xz} \\ u\tau_{xx}+v\tau_{xy}+w\tau_{xz}-q_x \end{pmatrix}, \quad \mathbf{F}_v = \begin{pmatrix} 0 \\ \tau_{xy} \\ \tau_{yy} \\ \tau_{yz} \\ u\tau_{xy}+v\tau_{yy}+w\tau_{yz}-q_y \end{pmatrix},$$

$$\mathbf{G}_v = \begin{pmatrix} 0 \\ \tau_{xz} \\ \tau_{yz} \\ \tau_{zz} \\ u\tau_{xz}+v\tau_{yz}+w\tau_{zz}-q_z \end{pmatrix}.$$

The viscous stress terms are given by

$$\tau_{xx} = \frac{2}{3}\mu[2(\xi_x u_\xi + \eta_x u_\eta + \zeta_x u_\zeta) - (\xi_y v_\xi + \eta_y v_\eta + \zeta_y v_\zeta) - (\xi_z w_\xi + \eta_z w_\eta + \zeta_z w_\zeta)],$$

$$\tau_{yy} = \frac{2}{3}\mu[2(\xi_y v_\xi + \eta_y v_\eta + \zeta_y v_\zeta) - (\xi_x u_\xi + \eta_x u_\eta + \zeta_x u_\zeta) - (\xi_z w_\xi + \eta_z w_\eta + \zeta_z w_\zeta)],$$

$$\tau_{zz} = \frac{2}{3}\mu[2(\xi_z w_\xi + \eta_z w_\eta + \zeta_z w_\zeta) - (\xi_x u_\xi + \eta_x u_\eta + \zeta_x u_\zeta) - (\xi_y v_\xi + \eta_y v_\eta + \zeta_y v_\zeta)],$$

$$\tau_{xy} = \mu(\xi_y u_\xi + \eta_y u_\eta + \zeta_y u_\zeta + \xi_x v_\xi + \eta_x v_\eta + \zeta_x v_\zeta),$$

$$\tau_{xz} = \mu(\xi_z u_\xi + \eta_z u_\eta + \zeta_z u_\zeta + \xi_x w_\xi + \eta_x w_\eta + \zeta_x w_\zeta),$$

$$\tau_{yz} = \mu(\xi_y w_\xi + \eta_y w_\eta + \zeta_y w_\zeta + \xi_z v_\xi + \eta_z v_\eta + \zeta_z v_\zeta),$$

where μ is the dynamic viscosity of the fluid. The heat fluxes are provided by the Fourier's law

$$\boldsymbol{q} = -\frac{\mu c_p}{Pr}\boldsymbol{\nabla}_{\boldsymbol{x}} T,$$

where c_p is the specific heat capacity at constant pressure, Pr the Prandtl number and T the temperature. The temperature is computed with the equation of state for a perfect gas, $T = p/(\rho r)$, with the specific gas constant for air $r = 287.05$ J.kg^{-1}.K^{-1}.

The temperature gradient $\boldsymbol{\nabla}_x T = (T_x, T_y, T_z)^T$ is computed using

$$T_x = \xi_x T_\xi + \eta_x T_\eta + \zeta_x T_\zeta,$$

$$T_y = \xi_y T_\xi + \eta_y T_\eta + \zeta_y T_\zeta,$$

$$T_z = \xi_z T_\xi + \eta_z T_\eta + \zeta_z T_\zeta,$$

in the physical domain. The dynamic viscosity is classically a function of the temperature and is determined by Sutherland's law:

$$\mu(T) = \mu_0 \sqrt{\frac{T}{T_0}} \frac{1 + \frac{C}{T_0}}{1 + \frac{C}{T}}, \tag{1.15}$$

where T_0 is a reference temperature [K], $\mu_0 = \mu(T_0)$ is the dynamic viscosity at the reference temperature and C is a fluid dependent parameter. Viscous and heat conduction terms are computed like the Eulerian fluxes and metric terms using the finite-difference schemes, presented in section 1.2.

1.8 Stability criteria

The time step Δt is governed by stability criteria that can be found for the convective, viscous and conductive terms.

For a curvilinear grid, the stability criterion for the convective terms is given by the Courant-Friedrichs-Lewy (CFL) number

$$\mathrm{CFL} = \Delta t \max \left(\frac{|U| + c\sqrt{\xi_x^2 + \xi_y^2 + \xi_z^2}}{\Delta \xi}, \frac{|V| + c\sqrt{\eta_x^2 + \eta_y^2 + \eta_z^2}}{\Delta \eta}, \frac{|W| + c\sqrt{\zeta_x^2 + \zeta_y^2 + \zeta_z^2}}{\Delta \zeta} \right) \leq 0.9.$$

At low Reynolds numbers, when viscous effects dominate, the stability criterion for the viscous fluxes is given by

$$C_\nu = \Delta t \max \left(\frac{\nu}{x_\xi^2}, \frac{\nu}{y_\eta^2}, \frac{\nu}{z_\zeta^2} \right) \leq 2.$$

The criterion for the thermal conduction terms is connected to the viscous terms criteria via the Prandtl number:

$$C_T = \frac{C_\nu}{Pr},$$

For high Reynolds number flows such as considered in this work convective terms will dominate and the time step is governed principally by the CFL-criterion.

1.9 LES strategy

Solving Navier-Stokes equations implies to capture an energy cascade from larger scales roughly characterized by the integral length scale L_f to smaller ones. This technique is called Direct Numerical Simulation (DNS). The cascade ends at the Kolmogorov scale l_η when turbulent energy is dissipated by the molecular viscosity. For isotropic homogenous turbulence [9], the disparity between L_f and l_η can be estimated using

$$\frac{L_f}{l_\eta} \sim \mathrm{Re}_{L_f}^{3/4}, \quad \text{where} \quad \mathrm{Re}_{L_f} = \frac{u' L_f}{\nu},$$

with u' being the scale of the velocity fluctuations in the flow. For 3-D applications, the total number of grid points required to simulate a volume of $O(L_f^3)$ therefore varies with $\mathrm{Re}_{L_f}^{9/4}$. Due to computational limits, only for flows at moderate Reynolds number, DNS can be applied. For Reynolds number higher then $\mathrm{Re}_{L_f} > 10^4$, only the largest flow scales can be computed whereas the effect of smaller scales that are not supported by the grid have to be modeled. This approach is called Large-Eddy Simulation (LES). In order to capture the principal physics of the flow, the flows are supposed to be rather characterized by the largest scales than by the smallest ones that are supposed to have a quasi-universal character.

In this section, the filtered Navier-Stokes equations are first presented. Then, the effect of the cut-off wave-number in LES is discussed and modeling approaches are recalled. Finally, the LES strategy adapted in this work is presented.

1.9.1 Filtered Navier-Stokes equations

To separate the large from the small scales, LES is based on the definition of a filtering operator. In practice, the discretization of a computational domain acts like a low-pass spatial filter applied to the Navier-Stokes equations which introduces extra terms describing the interaction between the resolved and the non-resolved scales. A filtered variable is obtained by convolution

$$\overline{f}(\mathbf{x}) = \int_D f(\mathbf{x}) G_\Delta(\mathbf{x} - \mathbf{x}') d\mathbf{x}',$$

where D is the computational domain, G_Δ is the filter kernel and $\Delta = \Delta\mathbf{x}$ the cut-off scale of the filter. By definition of the convolution operator, the filter $\overline{*} : f \rightarrow \overline{f}$ is linear. Classically, it is admitted that the filter commutates with the time and spatial derivatives, for more details refer to Sagaut [111], Lesieur *et al.* [87], Geurts [59]. The discretization of a computational domain means an irreversible loss of information about scales smaller than the cut-off scale of the filter.

In compressible flows, it is convenient to use Favre-filtering to avoid the introduction of a subgrid scale term in the equation of mass conservation. The Favre-filtered variable is defined as

$$\widetilde{f} = \frac{\overline{\rho f}}{\overline{\rho}},$$

where ρ is the density of the flow. In the following, f'' denotes the unresolved flow features and is defined as $f'' = f - \widetilde{f}$.

The filtered equations for mass and momentum write then in tensor form such as

$$\frac{\partial \overline{\rho}}{\partial t} + \mathrm{div}\left(\overline{\rho}\widetilde{\mathbf{V}}\right) = 0,$$

$$\frac{\partial \overline{\rho}\widetilde{\mathbf{V}}}{\partial t} + \mathrm{div}\left(\overline{\rho}\widetilde{\mathbf{V}} \otimes \widetilde{\mathbf{V}} + \overline{p}\mathcal{I} - \widehat{\mathcal{T}}\right) = \mathrm{div}\left(\mathbb{T} + \overline{\mathcal{T}} - \widehat{\mathcal{T}}\right),$$

where $\mathbf{V}$ is the velocity vector and the $\mathcal{I}$ the identity tensor and

$$\mathcal{T} = 2\mu(T)S, \text{ where } \quad S = \frac{1}{2}\left[\mathrm{grad}\mathbf{V} + \mathrm{grad}(\mathbf{V})^T - \frac{2}{3}I\mathrm{div}\mathbf{V}\right],$$

$$\widehat{\mathcal{T}} = 2\mu(\widetilde{T})\widehat{S}, \text{ where } \quad \widehat{S} = \frac{1}{2}\left[\mathrm{grad}\widetilde{\mathbf{V}} + \mathrm{grad}(\widetilde{\mathbf{V}})^T - \frac{2}{3}I\mathrm{div}\widetilde{\mathbf{V}}\right],$$

$$\mathbb{T} = \overline{\rho}\widetilde{\mathbf{V}} \otimes \widetilde{\mathbf{V}} - \widetilde{\overline{\rho}\mathbf{V} \otimes \mathbf{V}}$$

The term $\mathbb{T}$, called subgrid stress tensor, describes the effects of the unresolved scales and can not be determined using the resolved flow field. This term must therefore be modeled.

Following Vreman *et al.* [140], the filtered equation for the energy can be derived such as

$$\begin{aligned}\frac{\partial \overline{\rho}\widehat{e_t}}{\partial t} + \mathrm{div}\left[(\overline{\rho}\widehat{e_t} + \overline{p})\widetilde{\mathbf{V}} + \widehat{\mathbf{q}} - \widehat{\mathcal{T}} \otimes \widetilde{\mathbf{V}}\right] &= -\mathrm{div}\mathbf{Q} + \widetilde{\mathbf{V}} \cdot \mathrm{div}\mathbb{T} + \overline{\rho\epsilon} + \overline{\rho\pi} \\ &\quad + \mathrm{div}\left(\overline{\mathcal{T}} \otimes \widetilde{\mathbf{V}} - \widehat{\mathcal{T}} \otimes \widetilde{\mathbf{V}}\right) - \mathrm{div}(\overline{\mathbf{q}} - \widehat{\mathbf{q}}),\end{aligned}$$

where

$$\overline{\rho}\widehat{e_t} = \frac{\overline{p}}{\gamma - 1} + \frac{1}{2}\overline{\rho}\widetilde{\mathbf{V}}^2,$$

$$\mathbf{q} = \frac{c_p\mu(T)}{P_r}\mathrm{grad}(T),$$

$$\widehat{\mathbf{q}} = \frac{c_p\mu(\widetilde{T})}{P_r}\mathrm{grad}(\widetilde{T}),$$

$$\mathbf{Q} = \frac{\overline{p\mathbf{V}} - \overline{p}\widetilde{\mathbf{V}}}{\gamma - 1},$$

$$\overline{\rho\epsilon} = \overline{T : \mathrm{grad}\mathbf{V}} - \overline{T} : \mathrm{grad}\widetilde{\mathbf{V}},$$

$$\overline{\rho\pi} = \overline{p}\mathrm{div}\widetilde{\mathbf{V}} - \overline{p\mathrm{div}\mathbf{V}}.$$

The quantity $\widehat{e_t}$ is the total energy of the resolved flow field. $\mathbf{Q}$ is the vector of the pressure-velocity subgrid correlation, $\overline{\rho\epsilon}$ corresponds to the turbulent subgrid dissipation and $\overline{\rho\pi}$ is the pressure dilatation subgrid correlation.

The filtering of the Navier-Stokes equations adds terms that have to be modeled. Those terms are the subgrid stress tensor $\mathbb{T}$ which is present both in the momentum and energy equations and the two other terms $\mathbf{Q}$ and $\overline{\rho\pi}$. According to Vreman *et al.* [138], the other terms are neglected. Most of subgrid scale models are based on the isotropic homogenous turbulence context as the subgrid scales are supposed to have an isotropic behavior [111, 87].

1.9.2 Overview over the subgrid-scale models

Many subgrid scale models have been proposed in order to model the effect of the unresolved scales. In the following, the most popular models are recalled and the classification of the LES strategy realized in this work is given at the end of this section. For further lecture, refer to the book of Sagaut [111]

Models based on the subgrid viscosity

Most of the models are based on the energetic interpretation of the effect of subgrid scales. This is the reason why the subgrid viscosity concept is introduced to model the subgrid stress tensor. This concept has an analogy to the turbulent viscosity of Boussinesq for the Reynolds-Averaged Navier-Stokes (RANS) equations.

Introducing ν_t the subgrid viscosity in order to model the subgrid stress tensor.

$$\mathbb{T} = 2\overline{\rho}\nu_t\widetilde{S} - \frac{2}{3}\overline{\rho}\widetilde{k}_{\text{sgs}}I, \text{ with } \quad \bar{\rho}\widetilde{k}_{\text{sgs}} = \frac{1}{2}\bar{\rho}\widetilde{\mathbf{V}''\cdot\mathbf{V}''}$$

where k_{sgs} is the subgrid kinetic energy. This term can be modeled, but is often neglected as Erlebacher *et al.* [51] states. Finally, the problem reduces to the estimation of the subgrid viscosity.

Smagorinsky was one of the first to propose a model for ν_t. For incompressible flows, across a tube bundle in nuclear applications for example [7, 19], the Smagorinsky model is well adapted. However, this model introduces in general too much dissipation in laminar zones as it assumes the presence of turbulence when the flow has a velocity gradient. At the example of the development of a mixing layer, Vreman *et al.* [139] demonstrated that the Smagorinsky subgrid-scale model is less suited for transition problems. An improved approach of this model is the dynamic Smagorinsky model proposed by Germano *et al.* [58] which adapts the constant of the model locally to the flow field. The model reproduces transitional flows in a satisfying way but are computationally expensive [27].

For the terms $\mathbf{Q}$ and $\overline{\rho\pi}$ in the energy equation, a turbulent heat flux can be introduced through the subgrid viscosity concept introduced previously

$$-\text{div}\mathbf{Q} + \overline{\rho\pi} = -\text{div } \mathbb{Q},$$

with

$$\mathbb{Q} = -\frac{\overline{\rho}\nu_t c_p}{Pr_t}\text{grad}\widetilde{T},$$

where Pr_t is the turbulent Prandtl number. Finally, with this approach the filtered Navier-Stokes equations are similar to the classical Navier-Stokes equations with the addition of $\overline{\rho}\nu_t$ to its molecular counterpart [96]. The models based on the subgrid viscosity risk therefore to increase artificially the viscosity of the fluid. In conclusion, the effective Reynolds number of the flow is modified [47], which can play an important role for jet noise computations for example [27].

Model based on deconvolution

An alternative way to determine the subgrid terms is to compute them directly from the filtered field. This is obtained by a deconvolution of the filtered field for wave-numbers up to the grid cut-off wave-number. This takes into account non-linear interactions between scales beyond the accuracy limit of the numerical scheme and up to the cut-off wave-number of the grid. This method are known under the name of Approximate Deconvolution Method (ADM) and has been proposed by Stolz and Adams [120]. Furthermore, the energy transfer from resolved to non-resolved scales is modeled by a relaxation term that drains energy of the non-resolved scales preventing an accumulation of energy in the high-frequency range.

Implicit LES

For the implicit LES, the numerical dissipation is used to model the effect of the subgrid scales. In fact, the numerical dissipation provides the damping effect of the non-resolved scales: the subgrid stress tensor have not to be computed. The numerical dissipation is provided classically by a shock-capturing scheme [31]. Garnier *et al.* [55] have been observed that shock-capturing schemes introduces too much dissipation even for large scales. Additionally, the damping effect of dissipation is not sufficiently selective and can not be controlled due to the numerical complexity of the shock-capturing schemes.

LES based on explicit selective filtering

In this work, the selective filter used to remove grid-to-grid oscillations such as presented in section 1.4 plays the role of a eddy viscosity model by removing properly the fluctuations at wavenumbers greater than the scheme resolution. This method bears some similarities to the Approximate Deconvolution Model (ADM) [120]. As demonstrated by Mathew *et al.* [93], the effect of convolution with an explicit selective filter is similar to the effect of ADM. Moreover, the selective filtering induces a regularization similar to that used in the ADM procedure. This approach has been applied successfully in various applications [93, 105, 26, 20]

The equations to be solved write

$$\frac{\partial \overline{\rho}}{\partial t} + \mathrm{div}(\overline{\rho}\widetilde{\mathbf{V}}) = 0$$

$$\frac{\partial (\overline{\rho}\widetilde{\mathbf{V}})}{\partial t} + \mathrm{div}\left(\overline{\rho}\widetilde{\mathbf{V}} \otimes \widetilde{\mathbf{V}} + \overline{p}I - \widehat{\mathcal{T}}\right) = 0$$

$$\frac{\partial (\overline{\rho}\widehat{e_t})}{\partial t} + \mathrm{div}\left[(\overline{\rho}\widehat{e_t} + \overline{p})\widetilde{\mathbf{V}} + \widehat{\mathbf{q}} - \widehat{\mathcal{T}} \otimes \widetilde{\mathbf{V}}\right] = 0,$$

where

$$\widehat{\mathcal{T}} = 2\mu(\widetilde{T})\widehat{\mathcal{S}}$$

$$\widehat{\mathcal{S}} = \frac{1}{2}\left[\mathrm{grad}\widetilde{\mathbf{V}} + \mathrm{grad}(\widetilde{\mathbf{V}})^T - \frac{2}{3}I\mathrm{div}\widetilde{\mathbf{V}}\right]$$

$$\rho\widehat{e_t} = \frac{\overline{p}}{\gamma - 1} + \frac{1}{2}\overline{\rho}\widetilde{\mathbf{V}}^2$$

$$\widehat{\mathbf{q}} = -\frac{c_p \nu(\widetilde{T})}{P_r} \mathrm{grad}\widetilde{T}$$

Those equations are identical to the non-filtered ones. Therefore, they are written under strong conservation form which is suitable to deal with discontinuities. For simplification, notations associated with the filtering are dropped in the following.

1.10 Non reflective boundary conditions

Due to computational limitations the computational domain involving open domain boundaries has to be kept as small as possible and special boundary conditions have to be used in order to take into account the truncated domain. This is not a trivial task in particularly in CAA where perturbations have to leave properly the computational domain without generating non-physical perturbations [38].

In CAA there exist two families of non-reflective boundary conditions: the characteristic based boundary conditions and conditions based on far-field expressions of the governing equations. Both have been used in this work and are presented in the following.

1.10.1 Characteristic-based boundary conditions

The first one is based on characteristics developed by Thompson [131, 132] and by Poinsot and Lele [99]. The idea is to recast the Euler equations in the characteristic form projected on the direction normal to the boundaries of the computational domain. For a boundary perpendicular to the x-direction, the characteristic form writes:

$$\begin{array}{rcl} \frac{\partial \rho}{\partial t} + \frac{1}{c^2}\left[L_2 + \frac{1}{2}(L_5 + L_1)\right] & = & 0 \\ \frac{\partial u}{\partial t} + \frac{1}{2\rho c}(L_5 - L_1) & = & 0 \\ \frac{\partial v}{\partial t} + L_3 & = & 0 \\ \frac{\partial w}{\partial t} + L_4 & = & 0 \\ \frac{\partial p}{\partial t} + \frac{1}{2}(L_5 + L_1) & = & 0 \end{array} \quad \text{where} \left\{ \begin{array}{rcl} L_1 & = & (u-c)\left(\frac{\partial p}{\partial x} - \rho c \frac{\partial u}{\partial x}\right) \\ L_2 & = & u\left(c^2 \frac{\partial \rho}{\partial x} - \frac{\partial p}{\partial x}\right) \\ L_3 & = & u \frac{\partial v}{\partial x} \\ L_4 & = & u \frac{\partial w}{\partial x} \\ L_5 & = & (u+c)\left(\frac{\partial p}{\partial x} + \rho c \frac{\partial u}{\partial x}\right). \end{array} \right.$$

The quantities L_i, $i = 1..5$ are called invariants of the Euler equations system. They remain constant when they are propagated in the flow. L_1, L_5 describe the upstream and downstream traveling acoustic modes, L_2 the convected entropy mode and L_3 and L_4 the convected vortical mode. For a non-reflective boundary condition in x-direction, all invariants that propagate into the computational domain are set to be zero. The invariants that leave the computational domain are computed with non-centered finite-difference schemes. The characteristic equations have been implemented in Cartesian coordinates and applied only to 1-D flows. Formulations for generalized coordinates can be found in the work of Kim and Lee [77, 79] for instance.

1.10.2 Far-field boundary conditions

The second approach consists in designing boundary conditions for far-field radiation such as proposed by Bayliss and Turkel [15]. Tam and Webb developed radiation conditions by using far-field asymptotic expressions of the Euler's equations linearized around a uniform mean flow [128]. Tam and Dong [127] extended this approach to arbitrary mean flows. A 3-D formulation is given by Bogey and Bailly [28]. The set of equations solved on the last three points of the computational domain writes

$$\frac{1}{V_g}\frac{\partial}{\partial t}\begin{pmatrix}\rho\\u\\v\\w\\p\end{pmatrix}+v_g\left(\frac{\partial}{\partial r}+\frac{1}{r}\right)\begin{pmatrix}\rho-\rho_0\\u-u_0\\v-v_0\\w-w_0\\p-p_0\end{pmatrix}=0,$$

where v_g is the speed of wave propagation given by

$$v_g=(\bar{\mathbf{u}}+\bar{\mathbf{c}})\cdot\mathbf{e}_r.$$

The radius can be computed once a reference point (x_0,y_0,z_0) is determined. Thus r computes

$$r=\sqrt{(x-x_0)^2+(y-y_0)^2+(z-z_0)^2}$$

In the curvilinear domain the derivatives in r-direction are computed by

$$\frac{\partial}{\partial r}=\frac{\partial}{\partial\xi}\frac{\partial\xi}{\partial r}+\frac{\partial}{\partial\eta}\frac{\partial\eta}{\partial r}+\frac{\partial}{\partial\zeta}\frac{\partial\zeta}{\partial r}$$

The quantities $\partial\xi/\partial r$, $\partial\eta/\partial r$ and $\partial\zeta/\partial r$ are computed by

$$\begin{aligned}\frac{\partial\xi}{\partial r}&=\xi_x\frac{\partial x}{\partial r}+\xi_y\frac{\partial y}{\partial r}+\xi_z\frac{\partial z}{\partial r},\\\frac{\partial\eta}{\partial r}&=\eta_x\frac{\partial x}{\partial r}+\eta_y\frac{\partial y}{\partial r}+\eta_z\frac{\partial z}{\partial r},\\\frac{\partial\zeta}{\partial r}&=\zeta_x\frac{\partial x}{\partial r}+\zeta_y\frac{\partial y}{\partial r}+\zeta_z\frac{\partial z}{\partial r},\end{aligned}$$

where

$$\begin{aligned}\frac{\partial x}{\partial r}&=\frac{x-x_0}{r},\\\frac{\partial y}{\partial r}&=\frac{y-y_0}{r},\\\frac{\partial z}{\partial r}&=\frac{z-z_0}{r}.\end{aligned}$$

This formulation takes into account only acoustic perturbations. A similar formulation can be found for vortical and entropic modes but is not used in this work [128].

Due to their mono-dimensional character, characteristic based boundary conditions are preferred when perturbations impinge normally to the boundary condition. In general far-field radiation boundary condition behave better in the multidimensional case. As they are based on linearized Euler equations, a drawback is that they require a good guess of the mean quantities.

1.10.3 Sponge zone

Both approaches perform very poorly as outflow boundary condition, when vortical structures exit the computational domain. Thanks to a sponge zone vortical structures are damped out before they reach the boundary. The sponge zone used in this work consists of a strong grid stretching and of the application of an explicit Laplacian filter, introduced smoothly in order to avoid reflections. The filter is separately applied in each coordinate direction after each time iteration. A sponge zone applied at a outflow boundary perpendicular to the x-direction writes

$$\mathbf{U}_{i,j,k} = \mathbf{U}_{i,j,k} - \alpha \left(\frac{x_{i,j,k} - x_{i_\mathrm{e},j,k}}{x_{i_\mathrm{b},j,k} - x_{i_\mathrm{e},j,k}} \right)^{\beta} \left[\frac{1}{4}(\mathbf{U}_{i-1,j,k} + \mathbf{U}_{i,j-1,k} + \mathbf{U}_{i,j,k-1}) - \frac{3}{2}\,\mathbf{U}_{i,j,k} + \frac{1}{4}(\mathbf{U}_{i+1,j,k} + \mathbf{U}_{i,j+1,k} + \mathbf{U}_{i,j,k+1}) \right],$$

where the parameters $\alpha = 0.3$ and $\beta = 1.5$ ensure a smooth introduction of the filter [28]. The integers i_b and i_e designate the beginning and the end of the sponge zone respectively.

Finally a relaxation term as proposed by Poinsot and Lele [99] is applied in order to avoid numerical drift of the mean flow. For instance the pressure is updated such as

$$\mathbf{U}_{i,j,k} = \mathbf{U}_{i,j,k} + \alpha(\mathbf{U}_{i,j,k} - \mathbf{U}_t), \tag{1.16}$$

where $\mathbf{U}_t$ is the target value of the boundary condition. The term is applied to the pressure and the density at radiation and outflow boundaries. Near inflow boundaries this term is also applied to the velocity field. The coefficient $\alpha = 0.005$ has to be kept small in order to avoid reflections of acoustic waves.

1.11 Solid wall boundary

In this work, arbitrary bodies are discretized using body-fitted grids. Body-fitted grids are structured grids where the body boundary alines with a line in 2-D (or a surface in 3-D), characterized by a constant curvilinear coordinate. A 2-D body-fitted grid is shown in Figure 1.6 **(a)** for $\eta = \text{const}$. As indicated in the sketch, the slip wall conditions used in this work do not require orthogonal meshes and are valid for any arbitrary curvilinear grids.

In the following the solid wall boundary conditions are presented for inviscid flows where the flow slips around the solid body. Then, the wall boundary condition for Navier-Stokes equations are presented where the flow must satisfy the adherence condition and appropriate thermal conditions.

1.11.1 Slip wall conditions

A flow around an inviscid, non-moving and solid wall has to satisfy the condition $\mathbf{u}.\mathbf{n} = 0$ where $\mathbf{n}$ designates the vector normal to the wall as Figure 1.6 **(a)** illustrates for a wall, expressed by

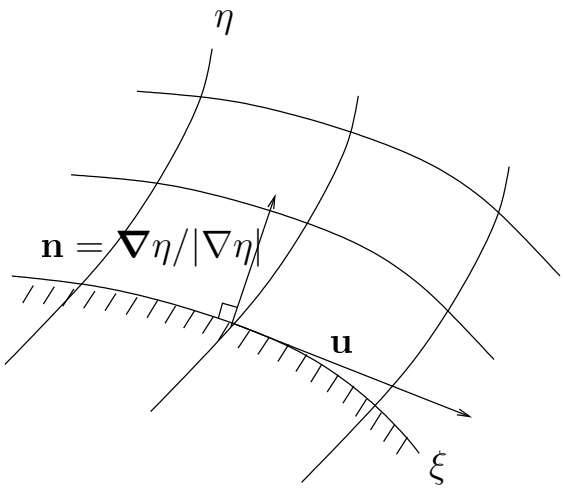

Figure 1.6: Body fitted grid for $\eta = const.$ The contravariant velocity $V = 0$ for the condition for a slip wall. For a no slip condition the flow velocity field has to satisfy $\mathbf{u} = \mathbf{0}$ at the wall.

η = const. In general, the normal vector $\mathbf{n}$ coincides with the normalized gradient of η, defined by $\nabla_x \eta = (\eta_x, \eta_y, \eta_z)^T$,

$$\mathbf{n} = \frac{\boldsymbol{\nabla}_x \eta}{|\boldsymbol{\nabla}_x \eta|}.$$

Thus, the slip wall condition can be expressed by the contravariant velocity such as

$$V = \boldsymbol{\nabla}_x \eta . \mathbf{u} = 0.$$

Different implementations of slip wall conditions are proposed in the literature [68]. Most of the approaches, in particular finite-volume methods, require an estimation of the pressure gradient $\partial p/\partial \eta$ at the wall in order to determine the pressure at the wall. For a 3-D inviscid flow, $\partial p/\partial \eta$ can be computed by projecting the momentum equations onto the wall normal direction. For that, the momentum equations are recasted in primitive form by using the chain rule, the mass conservation equation and the metric invariants (1.8):

$$\rho\frac{\partial u}{\partial t} + \rho U\frac{\partial u}{\partial \xi} + \rho V\frac{\partial u}{\partial \eta} + \rho W\frac{\partial u}{\partial \zeta} + \xi_x\frac{\partial p}{\partial \xi} + \eta_x\frac{\partial p}{\partial \eta} + \zeta_x\frac{\partial p}{\partial \zeta} = 0,$$

$$\rho\frac{\partial v}{\partial t} + \rho U\frac{\partial v}{\partial \xi} + \rho V\frac{\partial v}{\partial \eta} + \rho W\frac{\partial v}{\partial \zeta} + \xi_y\frac{\partial p}{\partial \xi} + \eta_y\frac{\partial p}{\partial \eta} + \zeta_y\frac{\partial p}{\partial \zeta} = 0,$$

$$\rho\frac{\partial w}{\partial t} + \rho U\frac{\partial w}{\partial \xi} + \rho V\frac{\partial w}{\partial \eta} + \rho W\frac{\partial w}{\partial \zeta} + \xi_z\frac{\partial p}{\partial \xi} + \eta_z\frac{\partial p}{\partial \eta} + \zeta_z\frac{\partial p}{\partial \zeta} = 0.$$

These equations are projected on the wall normal direction and leads to:

$$\begin{aligned}
&\rho\frac{\partial V}{\partial t} + \rho U\frac{\partial V}{\partial \xi} + \rho V\frac{\partial V}{\partial \eta} + \rho W\frac{\partial V}{\partial \zeta} \\
&+(\xi_x\eta_x + \xi_y\eta_y + \xi_z\eta_z)\frac{\partial p}{\partial \xi} + (\zeta_x\eta_x + \zeta_y\eta_y + \zeta_z\eta_z)\frac{\partial p}{\partial \zeta} + (\eta_x^2 + \eta_y^2 + \eta_z^2)\frac{\partial p}{\partial \eta} \\
&- \left[\rho U(u\frac{\partial \eta_x}{\partial \xi} + v\frac{\partial \eta_y}{\partial \xi} + w\frac{\partial \eta_z}{\partial \xi}) + \rho V(u\frac{\partial \eta_x}{\partial \eta} + v\frac{\partial \eta_y}{\partial \eta} + w\frac{\partial \eta_z}{\partial \eta}) + \rho W(u\frac{\partial \eta_x}{\partial \zeta} + v\frac{\partial \eta_y}{\partial \zeta} + w\frac{\partial \eta_z}{\partial \zeta})\right] = 0.
\end{aligned}$$

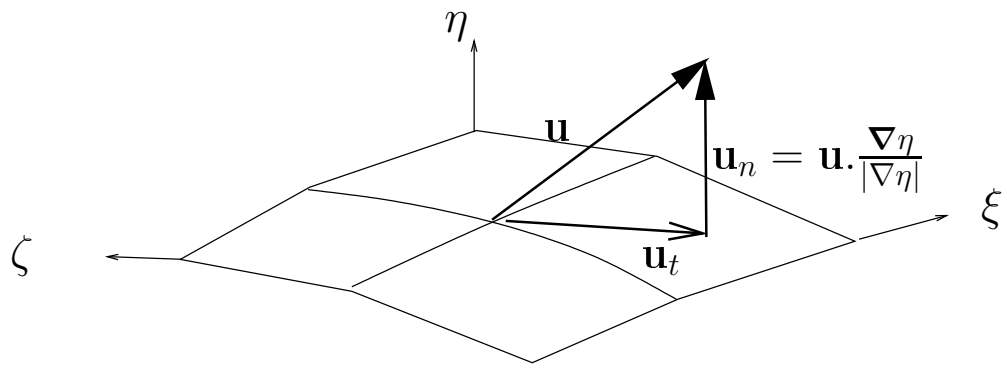

Figure 1.7: Update of velocities at a 3-D slip wall ($\eta = const$). The fluid is forced to be tangential to wall.

All terms multiplied by V or its derivative in ξ-direction $\partial V/\partial\xi$ vanish at the wall. The derivative of the pressure along η can be expressed by terms that only contain derivatives in the ξ-direction and ζ-direction:

$$\begin{aligned}\left.\frac{\partial p}{\partial \eta}\right|_{V=0} &= \frac{-1}{\eta_x^2+\eta_y^2+\eta_z^2}\Big[(\xi_x\eta_x+\xi_y\eta_y+\xi_z\eta_z)\frac{\partial p}{\partial \xi}+(\zeta_x\eta_x+\zeta_y\eta_y+\zeta_z\eta_z)\frac{\partial p}{\partial \zeta}\\ &\quad -\rho U(u\frac{\partial \eta_x}{\partial \xi}+v\frac{\partial \eta_y}{\partial \xi}+w\frac{\partial \eta_z}{\partial \xi})-\rho W(u\frac{\partial \eta_x}{\partial \eta}+v\frac{\partial \eta_y}{\partial \eta}+w\frac{\partial \eta_z}{\partial \eta})\Big].\end{aligned}$$

The first two bracket terms would vanish for (curvilinear) orthogonal grids, as $\nabla_x\xi.\nabla_x\eta = \nabla_x\zeta.\nabla_x\eta = 0$. The last two bracket terms relate the pressure gradient to the fluid velocity and to the curvature of the wall. Those terms also vanish when the fluid is at rest or the wall is plane. Finally, the determination of $\frac{\partial p}{\partial \eta}$ is quite complicated and a simplified wall treatment has been adapted in this work.

For the wall $\eta = \text{const.}$, the fluxes in the ξ- and ζ-direction are solved by centered schemes. The flux in η-direction is computed first by setting $V = 0$ and derivated by applying non-centered (or by applying centered with reduced stencils) finite-difference schemes. Additionally, the velocities are updated after every time step, by subtracting from the velocity vector $\mathbf{u}$ the normal velocity vector component $\mathbf{u}_n$:

$$\mathbf{u}_{\text{wall}} = \mathbf{u} - \mathbf{u}_n = \mathbf{u}_t,$$

where $\mathbf{u}_t$ is the tangential vector such as represented in Figure 1.7.

The no-slip boundary condition is successfully applied in purely acoustic test cases (with fluid in rest) as well as the computation of a 3-D transonic inviscid flow in a convergent divergent nozzle.

1.11.2 No-slip wall conditions with heat flux

A viscous flow around a solid body has to fulfill the adherence condition $\mathbf{u}_{\text{wall}} = 0$. The additional viscid fluxes of the Navier-Stokes equations contribute to the pressure gradient $\frac{\partial p}{\partial \eta}$ such as:

$$\begin{aligned}\frac{\partial p}{\partial \eta} = \left.\frac{\partial p}{\partial \eta}\right|_{V=0} + \frac{1}{\eta_x^2+\eta_y^2+\eta_z^2} \quad \cdot \quad & \left\{\eta_x \frac{\partial}{\partial \xi}\left[\frac{1}{J}(\xi_x\tau_{xx}+\xi_y\tau_{xy}+\xi_z\tau_{xz})\right]\right. \\ + \quad & \eta_y \frac{\partial}{\partial \eta}\left[\frac{1}{J}(\eta_x\tau_{xy}+\eta_y\tau_{yy}+\eta_y\tau_{yz})\right] \\ + \quad & \left.\eta_z \frac{\partial}{\partial \zeta}\left[\frac{1}{J}(\zeta_x\tau_{xz}+\zeta_y\tau_{yz}+\zeta_z\tau_{zz})\right]\right\}.\end{aligned}$$

The pressure derivative in the η-direction is not required since the momentum conservation equations are not needed to be solved for wall points. Only the mass and energy conservation equations are solved. The wall flux term for the η-direction becomes:

$$\frac{\partial \boldsymbol{F}}{\partial \eta} = \begin{pmatrix} \rho \frac{\partial}{\partial \eta}\left(\frac{V}{J}\right) \\ 0 \\ 0 \\ 0 \\ \frac{\gamma}{\gamma-1} p \frac{\partial}{\partial \eta}\left(\frac{V}{J}\right) - \frac{\partial}{\partial \eta}[\frac{1}{J}(\eta_x E_{v,5} + \eta_y F_{v,5} + \eta_z G_{v,5})] \end{pmatrix}$$

Note that the total energy ρe_t at the wall is proportional to the pressure p as the velocities vanish $\rho e_t = p/(\gamma - 1)$. Advancing the energy equation in time gives directly the pressure at the wall.

For isothermal walls the imposed temperature is prescribed and ρ can be computed by the ideal gas law using the pressure p, obtained by the energy equation. When a heat flux q is imposed, the components of the vector $\mathbf{q} = (q_x, q_y, q_z)^T$ are expressed as follows:

$$\mathbf{q} = q\mathbf{n}$$

For adiabatic walls the latter term is set to be zero. The temperature is not predicted correctly by setting the heat flux normal to the wall equal q for long time simulations and the solution tends to diverge. Therefore the temperature is updated in a such a way that the identity $\mathbf{q}.\mathbf{n} = q$ is fulfilled. In this work only, adiabatic walls are considered and the gradient of the temperature writes using Fourier's law

$$\boldsymbol{\nabla}_x T . \boldsymbol{\nabla}_x \eta = 0.$$

Now, $\partial T/\partial \eta$ can be determined explicitly using

$$\frac{\partial T}{\partial \eta} = \frac{1}{\boldsymbol{\nabla}_x \eta \boldsymbol{\nabla}_x \eta} \left(T_\xi \boldsymbol{\nabla}_x \xi \boldsymbol{\nabla}_x \eta + T_\zeta \boldsymbol{\nabla}_x \zeta \boldsymbol{\nabla}_x \eta\right).$$

Finally, the temperature at the wall is updated such as

$$T_{i,j,k} = \frac{1}{a_0}\left(\left.\frac{\partial T}{\partial \eta}\right|_{i,j,k} - \sum_{r=1}^{N-1} a_r T_{i,j+r,k}\right),$$

where a_r are the coefficients of a non centered finite difference scheme of stencil width N. For strongly non-linear problems the use of high-order non-centered finite-difference schemes exhibited stability problems. In this work only first-order approximations are therefore used:

$$T_{i,j,k} = T_{i,j+1,k} - \left.\frac{\partial T}{\partial \eta}\right|_{i,j,k}$$

The adiabatic wall boundary conditions are validated in chapter 2 for a plane Couette flow as well as for the flow around the cylinder.

1.12 Multidomain approach for complex geometries

Due to the complexity of industrial configurations and the requirement to handle moving body problems, the overset or Chimera grid approach is used in this work. First introduced by Benek *et al.* [18] this approach uses a set of overlapping structured grids to decompose the domain of interest.

The Chimera grid scheme offers the following advantages: a) the use of structured grids allows the use of efficient block structured flow solvers and the associated boundary conditions; b) the use of interpolation for communication between overlapping grids allows grids to be moved relative to each other. Although the communication between overlapping grids must be reestablished whenever a grid is moved, this is computationally less expensive than the recomputation of the whole grid as it is often done for unstructured grids. The process of establishing communication between overlapping grids is referred to as grid assembly. The Chimera approach was originally developed for second-order accurate solvers. Delfs [43] who was the first using the overset grid technique for CAA concluded that high-order interpolation has to be used in order to maintain the global accuracy of the high-order schemes. As high-order interpolation involves larger stencils and therefore larger overlap regions, the order of interpolation is a very important parameter in the generation of overset grids and its complex data structure is done by a so called grid assembly software.

There exists several teams working about this problem since the last two decades. A nice review can be found in [100]. The first and more widely used code is called PEGASUS5 [109]. The grid assembly has been automated and a minimum amount of user input is required to generate overset grids. PEGASUS5 is used by Sherer to generate high-order overset grids using a preprocessing tool called BELLERO [116]. A recent software is the SUGGAR code which stands for Structured, Unstructured, Generalized overset Grid AssembleR. SUGGAR illustrates that the Chimera grid approach is not restricted to structured grids any more. This shows the new trend to combine structured grids with unstructured grids resulting in so called hybrid grids. Schwartzkopff *et al.* [114] work on this methods mixing ADER methods for the unstructured grids and DRP schemes for the structured grids.

Another assembly software mentioned here is *Overture*. *Overture* is an object-oriented code framework for solving partial differential equations developed by W. Henshaw [35] at the Center for Applied Scientific Computing of the Lawrence Livermore National Laboratory (LLNL). The library is written in C++ and has Fortran kernels for computationally intensive tasks. The *Overture* software consists of the grid generator *ogen*, the flow solver *overBlown* and the visualizer *plotStuff*.

The grid generator is able to create overlapping grids in 2-D and 3-D for interpolation of arbitrary order. An example of an overset topology is given in Figure 1.12 showing a cylinder embedded in a Cartesian grid. The grid has been generated by *Overture* for fourth-order explicit finite difference schemes requiring a 5 point stencil. In order to recover overall fourth-order accuracy, fourth-order interpolation polynomials involving a 4 point stencil have to be used. In order to avoid an interpolation stencil to extend into the zone where the block receives interpolated data from other grids, a sufficiently large overlap region has to be generated as shown in Figure 1.12. Additionally, *Overture* features the useful task of hole cutting, cutting out useless points that are cut by the cylindrical grid. To make *Overture* to cut holes in the grids of demand a hierarchy between the component grids have to be specified by the user. *Overture* prepares a mask array marking all interpolation, computational and hole points which can be exploited by the solver.

Contrary to the first two softwares, *Overture* is freely available and can be downloaded without restrictions from the LLNL homepage. Although *Overture* is not as optimized as PEGASUS5, its well defined algorithms are very stable [100]. *Overture* is well documented and effort is done for the generation of grids starting from CAD-files in order to minimize the user input.

Since no stable parallel version of *Overture* exists, only the grid assembly abilities are exploited in this work. A new code, called SAFARI (Simulation Aéroacoustique de Fluides Avec Resonances et Interactions), has been developed that prepares an overset grid, generated by *Overture*, for parallel computation. SAFARI has been written in Fortran90 in order to benefit of derived types like *structures* in order to handle more complex data structures. The programming model used for SAFARI is referred to single process multiple data (SPMD). This means that the same source is compiled and executed on each processor while manipulating its own data. Communication between the processors is realized by using functions issued from the MPI-library.

The box bounded by the solid line in Figure 1.13 illustrates schematically the tasks that can be done by SAFARI such as it is developed in this work. First an overset grid is created by the user in form of a script file with the extension *.cmd*. This file contains informations about the geometry of each component grid, their hierarchy, the order of interpolation between the component grids and the order of discretization used on each component grid. In order to create an overlapping grid the .cmd file has to be compiled by *ogen*, that creates and saves the geometry and the interpolation data in a .hdf file (HDF4). SAFARI reads the .hdf file using functions provided by *Overture*. Each single component grid is then subdivided into blocks that are distributed to a single processor. It distributes the interpolation data computed by *ogen* according to the domain decomposition in order to parallelize this computationally expensive operation.

To treat Fluid Structure Interaction (FSI) problems, SAFARI will be able to tackle with grids that move relative to each other due to moments and forces that act on solid bodies. For that it will be necessary to call grid assembler functions during the time integration loop. This task should be easy to implement thanks to the conception of *Overture* as library.

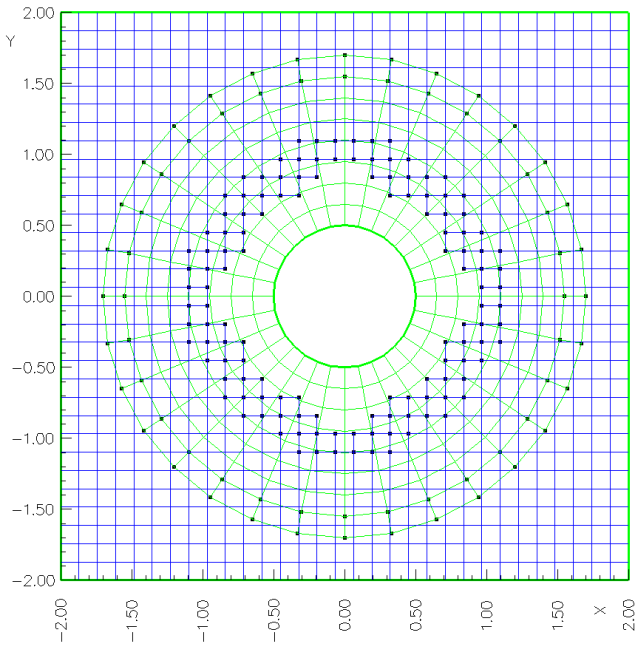

Figure 1.8: Example of an overset grid generated by *ogen*. The cylindrical grid is embedded in a Cartesian grid. The black squares designate where information has to be exchanged in order to compute a solution. Those values have to be interpolated as the grid points do not coincide in general.

1.13 Communication between processors

The solver for viscid and inviscid flows developed in the previous sections uses an explicit single-time stepping algorithm. Therefore grid points on each processor may be updated to the next time level simultaneously. In order to calculate the spatial derivatives via explicit finite-difference schemes only near processor domain boundaries data must be exchanged. For inviscid computations the flow variables $(\rho, \rho u, \rho v, \rho w, \rho e_t)^T$ must be transfered. Viscous computations require additionally the viscous terms and the heat conduction terms to be passed by MPI. As double precision is needed a fairly amount of data has to be transfered.

There are two kinds of communications implemented in the code: Inter-grid communication that consists of an interpolation procedure and a MPI send-receive procedure. Inter-block communications are handled by MPI routines only, since the points at the block boundaries coincide.

1.13.1 Inter-Grid communication

Inter-grid communication is affected by high-order interpolation schemes. Sherer and Scott [116] tested high-order interpolation methods. They considered a generalized Lagrangian polynomial method consisting of optimized or non-optimized methods in explicit and compact form. Furthermore they compared them with interpolation methods using B-splines. They concluded that classical Lagrangian

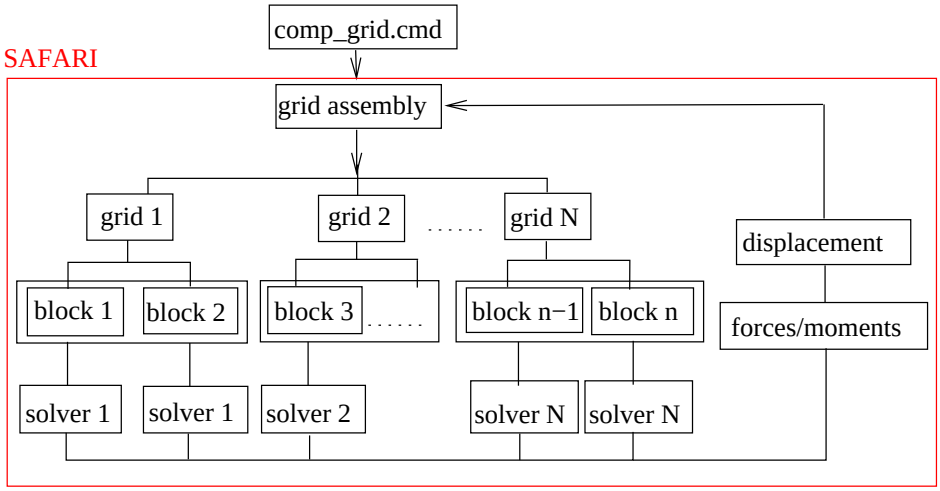

Figure 1.9: Schematic diagram of SAFARI: box bounded by —— describes the state of SAFARI such as developed in this work; box bounded by - - - describes the future state of SAFARI when FSI problems are addressed.

explicit interpolation methods offer the best compromise between accuracy, robustness and complexity in implementation. Although B-Splines methods can be constructed independently from the interpolation stencil size for arbitrary orders of accuracy, they are not preferred by Sherer and Scott as for those methods derivatives at the interpolation stencil extremities have to be specified. Interpolation schemes optimized for higher wave number were proposed by Tam [124] and Sherer and Scott [116]. The latter stated that optimized Lagrangian interpolation performs well in the high wave number range but can decrease in accuracy for lower wave number. Therefore high-order explicit Lagrangian polynomials are used in this work.

Lagrangian polynomials are implemented in SAFARI as follows. At a point P, the value ϕ_P of a function $\phi_{\xi,\eta}$ which is known in the curvilinear coordinate system (ξ,η) is given in 2-D by

$$\phi_P = \sum_{i=0}^{N_\xi-1}\sum_{j=0}^{N_\eta-1} R_i^\eta R_j^\xi \;\; \phi_{I_P+i,J_P+j} \quad \text{where} \quad R_i^\xi = \prod_{\substack{m=0 \\ m\neq i}}^{N_\xi} \frac{(\delta_\xi - m)}{(i-m)} \quad \text{and} \quad R_j^\eta = \prod_{\substack{m=0 \\ m\neq j}}^{N_\eta} \frac{(\delta_\eta - m)}{(j-m)},$$

where N_ξ and N_η are the number of interpolation points in the directions ξ and η respectively, as displayed in Figure 1.10 **(a)**. The point (I_P, J_P) is the first point at the lower, left corner of the interpolation stencil. The quantities δ_ξ and δ_η are the curvilinear coordinates of the point P relative to the point (I_P, J_P). The interpolation coefficients R_i^η and R_j^ξ are computed before entering in the time integration loop and are stored in a 1-D array of length $N_\xi + N_\eta$.

In the literature the quantities δ_ξ and δ_η are often called *offsets*. The accurate computation of these *offsets* is crucial for the overall accuracy of the interpolation. *Overture* computes the *offsets* with second-order accuracy, when it does not know the inverse mapping function $\boldsymbol{\xi} = \boldsymbol{\xi}(\mathbf{x})$ explicitly. Since the test cases computed in the validation chapter 2 of this work involve grid geometries with moderately skewed grids or simple geometries like cylinders and uniform grids, the high-order accurate computation of the *offset* have not been implemented in this work. If high-order accurate *offsets* are

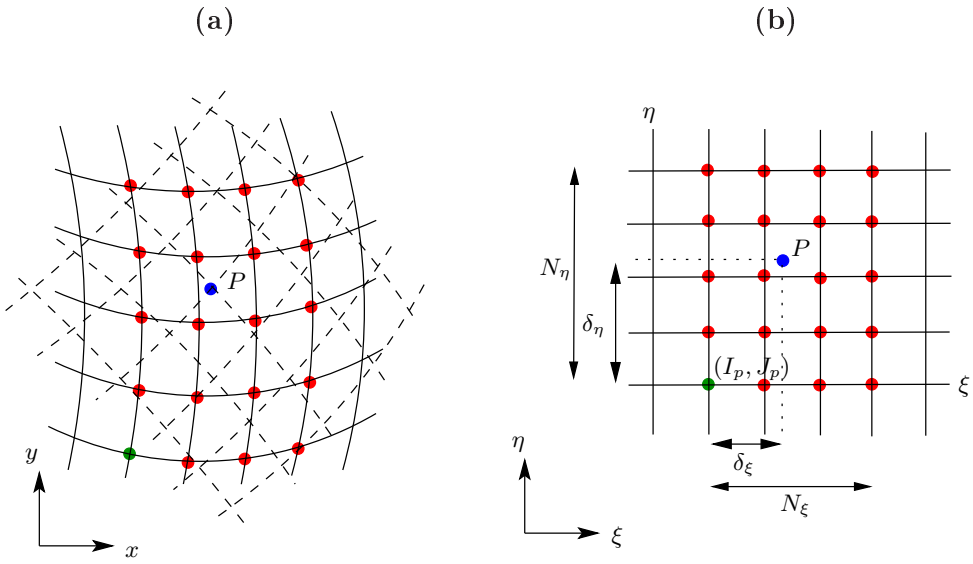

Figure 1.10: Example of a 2-D interpolation stencil in **(a)** physical space and **(b)** computational space. The point P on the grid – – – needs to be updated via interpolation using data of the grid ——— . In computational space the interpolation stencil is uniform. (I_p, J_p) is the lower left point of the interpolation stencil, N_ξ, N_η is the stencil width in ξ- and η-direction and δ_ξ, δ_η are the curvilinear distances between the point P and (I_p, J_p), the lower left stencil point.

required, Sherer [116] extended the inverse mapping problem for high-order schemes proposed by Benek *et al.* [18]. Another method has been proposed by Guénanff [63].

Note, that the maximum formal order of Lagrangian polynomials is related directly to the length of the interpolation stencil N_ξ. A multidimensional analysis of Lagrangian polynomials is given, for example by Tam and Hu [124] and Guénanff [63].

All data necessary for the interpolation are computed by *Overture* in a preprocessing step and are associated to the receiver grid. However interpolation should be done by the donor grid in order to minimize the amount of data to be transfered between the processors. Thus, the receiver grid sends all necessary data to the donor grid before time integration is started. This is not a trivial task since a grid is divided in a arbitrary number of blocks. This task is parallelized in SAFARI, resulting in a minimized computational overhead.

1.13.2 Inter-Block communication

SAFARI divides a component grid evenly in each coordinate direction ξ, η, ζ in blocks of grid points $N_{\text{block},\xi}, N_{\text{block},\eta}, N_{\text{block},\zeta}$. Figure 1.12 shows an example of a 2-D grid subdivided in $N_{\text{block},\xi} = 3$ blocks in ξ-direction and $N_{\text{block},\eta} = 2$ blocks in η direction. Periodic boundary conditions are also handled with inter-block communications routines.

The number of blocks per grid is estimated by a simple algorithm that requires as input the maximum number of grid points that should be computed on one processor. Under the assumption that all points need the same amount of operations, the algorithm determines the number of blocks needed for one grid in order to not exceed the maximum number of grid points and by minimizing the

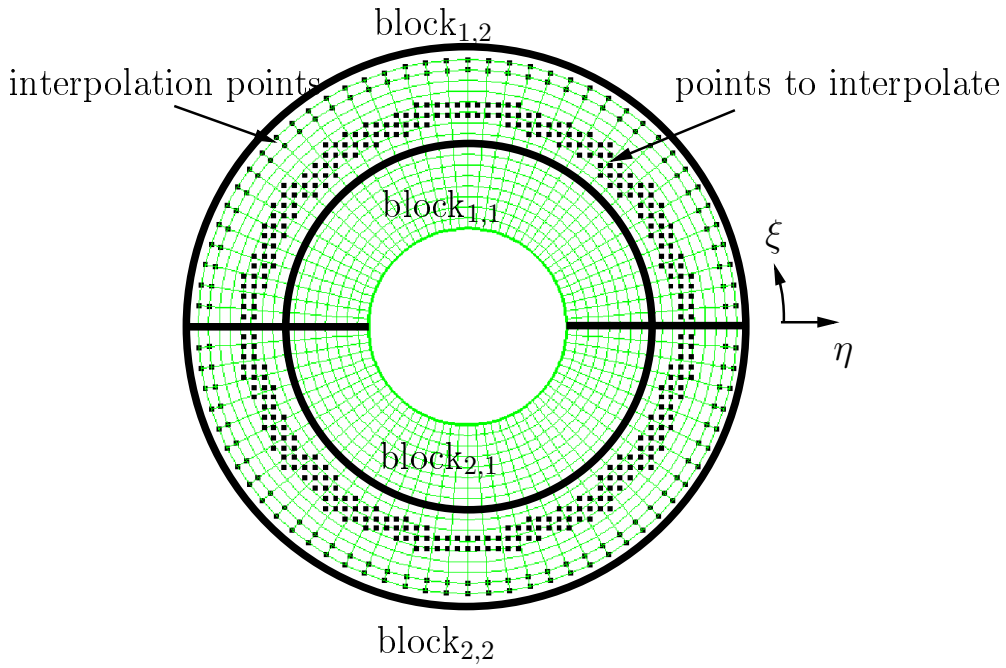

Figure 1.11: Example of a 2-D cylindrical grid subdivided in $N_{\text{block},\xi} \times N_{\text{block},\eta} = 2 \times 2$ blocks. Interpolation points receive data from blocks belonging to the background grid (not represented in this Figure). $\text{block}_{1,2}$ and $\text{block}_{2,2}$ also have to interpolate data and send it to the blocks of the background grid. $\text{block}_{1,1}$ and $\text{block}_{2,1}$ do not contribute to the grid communication.

number of communication points determined by

$$A_{\text{com}} = (N_{\text{block},\xi} - 1) \cdot N_\eta \cdot N_\zeta + (N_{\text{block},\eta} - 1) \cdot N_\xi \cdot N_\zeta + (N_{\text{block},\zeta} - 1) \cdot N_\xi \cdot N_\eta,$$

where N_ξ, N_η, N_ζ are the total number of grid points in each direction of component grid.

Figure 1.12 gives a schematical view of the layout on a local computational block used by a single processor. This shows that there are overlap regions on each side of the local domain where information must be obtained from neighboring processors. Likewise, this processor would also need to send some data to these neighbors. For the finite difference solver used in this work, where the spatial operators are applied in each direction separately no update of data at the corners is necessary. However it is possible that a multidimensional interpolation stencil lies within the corner region as shown in Figure 1.13. If this is the case, SAFARI also updates in the corner region.

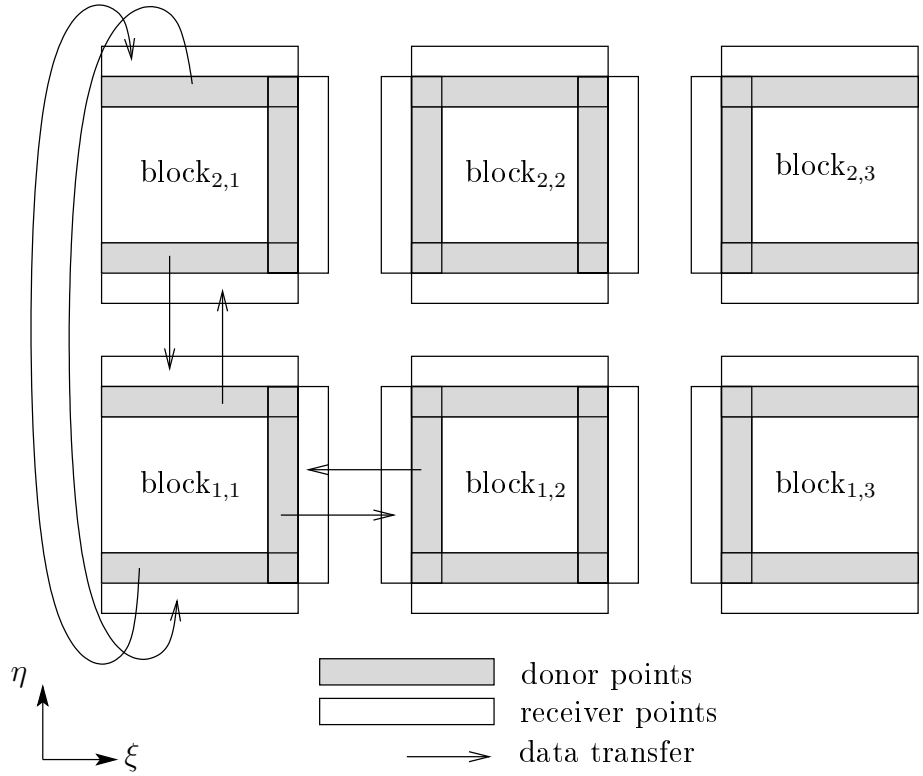

Figure 1.12: Inter-block communication in a 2-D grid with periodic boundary condition in η-direction subdivided in $N_{\mathrm{block},\xi} \times N_{\mathrm{block},\eta} = 3 \times 2$ blocks.

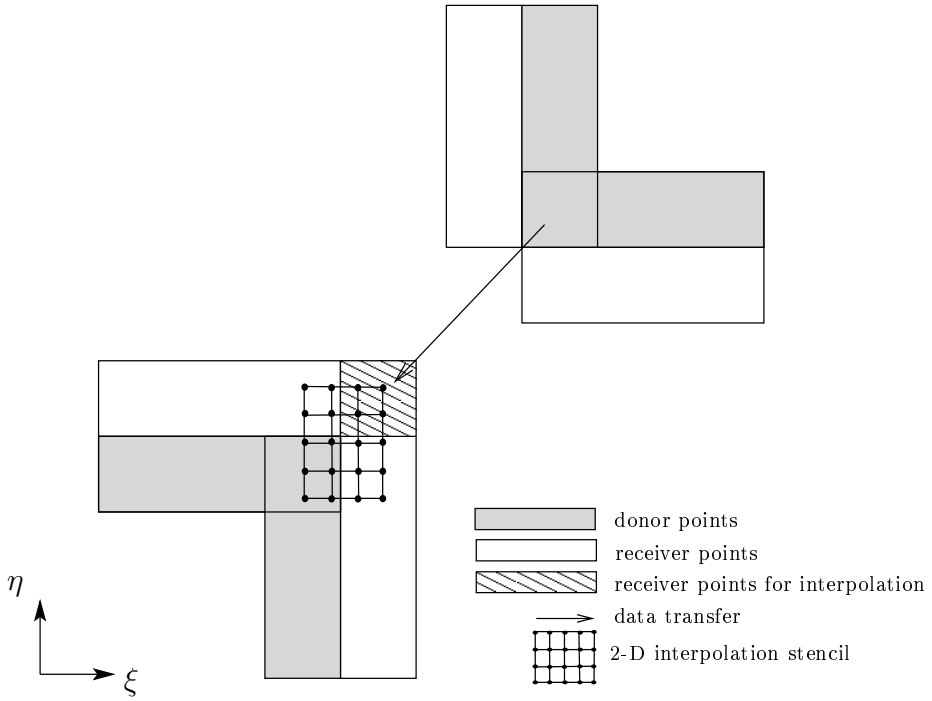

Figure 1.13: Detail of a block corner: Update of corner region when interpolation stencil includes points of this region.

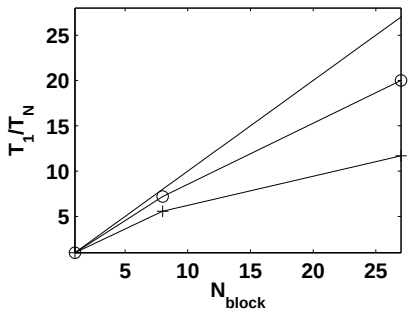

Figure 1.14: Scalability of SAFARI. T_N denotes the time needed to perform the task using N procesors. Speed-up curve for the case with constant total number of grid points N_{tot}: $\circ$ update only regions normal to boundaries; + additional update of corner regions.

1.13.3 Scaling test for inter-block communication

In this section scaling tests of the parallelization is provided for the examples of a cubic grid containing $N_{\text{tot}} = 100 \times 100 \times 100 = 1 \times 10^6$ grid points. The grid is generated by *Overture* and computed by SAFARI, using $N_{\text{procs}} = i^3, i = 1, 2, 3$ processors. This scaling test is very demanding because the ratio between the number of communication points and the number of computation points becomes very constraining and gives an idea of the limit of grid points per processor not to exceed. The results were obtained on the cluster *Tantale* of the CEA (CP 4000 DL 585 quadri processors AMD Opteron 1.8 GHz, Network Infiniband with a latence 5μs, 1 GByte.s^{-1}). The time of one iteration required for one grid point on a single processor is 8.6×10^{-6} s.

Figure 1.14 shows the parallel performance of the code compared with the ideal linear speedup curve for the first test case. Up to ten processors the code performs well. For cases with more than ten processors the actual performance deviates from the ideal because a large amount of data has to be exchanged due to the use of large 11-point computational stencils. For 3-D computations, using less then 1×10^5 per processor should be avoided.

As already mentioned only data normal to the communication boundaries have to be exchanged as displayed in Figure 1.14. However if a interpolation point is situated near a corner so that the interpolation stencil involves points in the corner regions data has to be updated. Figure 1.14 illustrates that for the 3-D case the parallel code performs very poorly due to a large communication overhead when the corners are updated. Therefore the update of the corners has to be avoided whenever it is possible.

The scaling test reveals that communications has to be minimized and optimized in the future especially for massively parallel computations. This can be achieved by non-blocking communications and a more sophisticated load balancing taking into account boundary conditions. Anyways the multidomain approach permits to access applications with a very large number of grid points. SAFARI is portable on several massively parallel platforms like HP Proliant, Bull 3045 and BlueGene.

1.14 Conclusion

The numerical algorithm SAFARI has been presented in this chapter. The associated flow solver is a high-order finite difference solver for the purpose of solving Euler and Navier-Stokes equations on structured grids. The implemented selective filter removes grid-to-grid oscillations. When solving Navier-Stokes equations, the selective filter plays the role of a sub-grid model by removing properly the not well resolved turbulent scales. In order to treat flows with shocks, a Jameson-type dissipation model has been implemented in the code. The associated wall boundary conditions and non reflective boundary conditions have been specified in this chapter.

To tackle with complex geometries using a structured grid solver, a high-order accurate overset grid approach has been implemented in the code. The code is parallelized using the MPI library and allows to access to high-Reynolds applications.

Chapter 2

Validation of SAFARI

In the following, several validation test cases are reported. These test cases involve classical problems encountered in computational aeroacoustics as well as in computational fluid dynamics. The test cases are destinated to check if the multi-domain approach and the shock-capturing technique implemented in this work are able to recover the accuracy of the high-order finite-difference schemes. Since the test cases involve also walls and open domain boundary conditions, the implemented boundary conditions are also validated in this chapter.

2.1 Convection of a vortex through interpolation zones

The passage of the wake generated by a cylinder through an overlap region generates spurious acoustic waves as it has been observed by Desquesnes *et al.* [45]. In this work, a strong influence of the polynomial order on the accuracy and on the generation of spurious acoustic waves have been observed when vortical structures are involved. The convection of a vortex by an inviscid uniform mean flow through a overset region is therefore considered first. By varying the interpolation order, the minimum order that is required to recover the accuracy of the optimized finite-difference schemes is determined in the following.

The overlapping grid, generated by *ogen*, is displayed in Figure 2.1. It is composed of three uniform grids connected by two overlap regions. The left and the right grids contain $N_\xi \times N_\eta = 51 \times 51$ points. The center grid consists of $N_\xi \times N_\eta = 51 \times 52$ and is shifted by half a grid size length in x-direction such as displayed in Figure 2.2 **(a)**. This avoids interpolation points to coincide with grid points in the zone where the vortex passes.

The vortex is defined by the initial conditions using dimensionless variables:

$$\rho = 1$$

$$\rho u = \rho \left\{ M + y\ \epsilon\ \exp\left[-\frac{\log(2)}{\alpha^2}(x^2 + y^2) \right] \right\}$$

$$\rho v = \rho\ x\ \epsilon\ \exp\left[-\frac{\log(2)}{\alpha^2}(x^2 + y^2) \right]$$

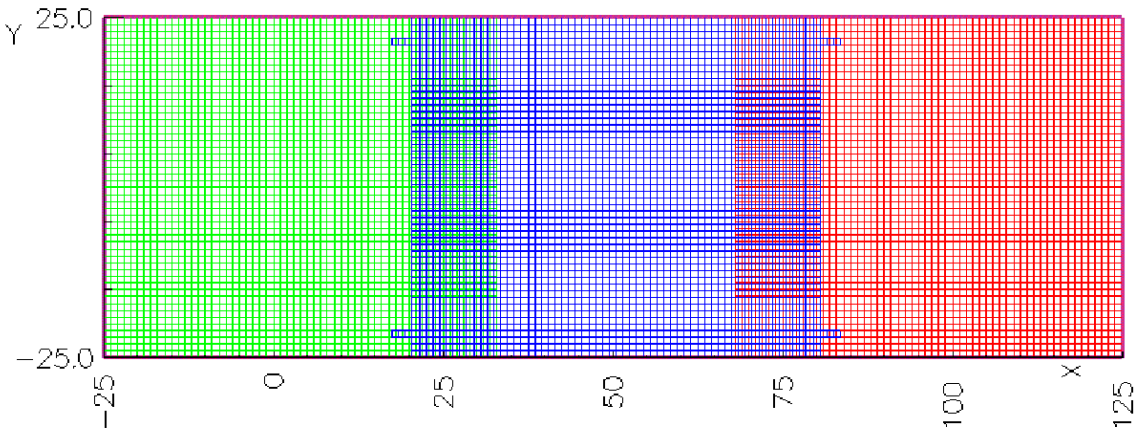

Figure 2.1: Overlapping grid generated by *ogen*. The grid is composed of three uniform grids connected by two overlap regions of variable width.

$$\rho e_t = \frac{1/\gamma}{\gamma - 1} + \frac{1}{2}\rho(u^2 + v^2),$$

where $M = 0.5$ is the freestream Mach number, $\epsilon = 0.01$ is the vortex strength and $\alpha = 3\Delta x$ the Gaussian half width. The Fourier transform of the swirl velocity (the transversal velocity component along the x-axis at $y = 0$) is given by:

$$\hat{v}(k) = -2i\sqrt{\frac{\pi}{a}}\frac{k}{4a}\exp\left[-\frac{k^2}{4a}\right],$$

where $a = \log(2)/\alpha^2$ contains the Gaussian half width. The normalized power spectral density is plotted in Figure 2.2 **(b)**. A dominant peak at $k\Delta x = \sqrt{2a} \approx 2\pi/16$ is observed. Most of the spectral content is located within the well resolved wave-number domain of the optimized finite-difference schemes.

The radiation boundary conditions of Tam and Dong [127] are applied to all boundaries. For all computations the CFL number is fixed to CFL = 0.25. The simulations are carried out for 800 iterations, the time required to convect the vortex $100\Delta x$.

Five simulations are done varying the order of interpolation $N_{\text{order}} = 2, 4, ...10$. Figure 2.3 displays a sequence of the instantaneous pressure field when the vortex, characterized by a pressure minimum, meets the first overlap region. Figures 2.3 **(a)**, **(b)** and **(c)** are obtained using Lagrangian polynomials of order $N_{\text{order}} = 2, 6$ and 10 respectively. The acoustic wave just leaving the computational domain at the first and second instant is due to an adaptation of the pressure field to the velocity field at the beginning of the simulation. It is a transitional artefact and was also observed by Bogey [25]. The sequence **(a)** using the second-order interpolation, strong acoustic disturbances are generated and contaminate the physical solution. Those parasite waves are significantly reduced when using sixth-order Lagrangian polynomials (sequence **(b)**) and disappears when a tenth-order interpolation scheme is used (sequence **(c)**).

In order to quantify the generation of spurious acoustic perturbation the residual pressure for the

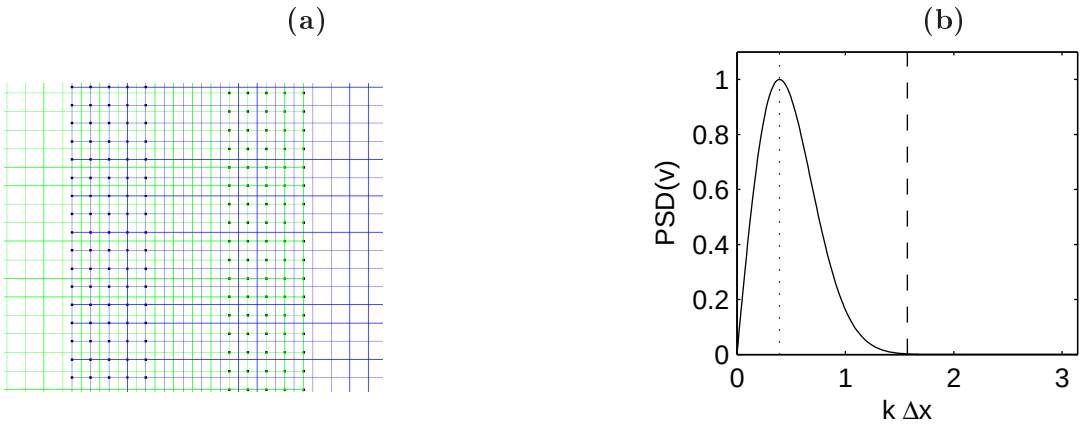

Figure 2.2: **(a)** Detail view of the center of an overlapping region ($y = 0$). The interpolation points do not match with the interpolation data. **(b)** Normalized spectral contents of the transversal velocity component of the initial vortex; ····· dominant wave length, − − − maximal resolution of optimized 11-points finite difference schemes $k\Delta x \approx \pi/2$ [30].

left grid is computed using the L_2 norm:

$$L_p = \sqrt{\frac{1}{N_\xi N_\eta} \sum_{i,j}^{N_\xi, N_\eta} p'_{i,j}}.$$

The residual obtained for the left grid is plotted in Figure 2.4 **(a)** as a function of the number of iterations. The solid line representing the pressure residual obtained with the single block computation is considered as a reference solution. The symbols in Figure 2.4 **(a)** represent the pressure residual obtained with the overlapping grid for varying polynomial orders. The first peak observed during the first 200 iterations for all setups is associated to the transitional pressure pulse. The decrease of the residual pressure, indicates that the pressure pulse leaves the computational domain without any spurious reflections. When the vortex hits the overlap zone, the residual pressure obtained with second-order polynomials shows a significant increase and confirms the generation of acoustic waves observed in Figure 2.3 **(a)**. Using fourth-order polynomials the reflection are only visible in a zoom on the last 600 iterations given in Figure 2.4 **(b)**. For orders higher than 6 the residual pressure evolves like in the single-block computation and the reflections are negligible.

The error of the aerodynamic field is estimated by computing the L_2 norm of the difference between the exact swirl velocity and the swirl velocity when the vortex has reached its final position at $x = 100\ \Delta x$. The error is computed along the x-axis at $y = 0$ such as:

$$L_v = \sqrt{\frac{1}{N_\xi} \sum_{i}^{N_\xi} v_i|^2_{y=0}}.$$

The values for L_v are given in Table 2.1 and are plotted in Figure 2.5, normalized by the single-block result. Figure 2.5 reveals that for polynomial orders higher than 6 the accuracy of the numerical algorithm is governed by the spatial and time integration errors and the interpolation error becomes

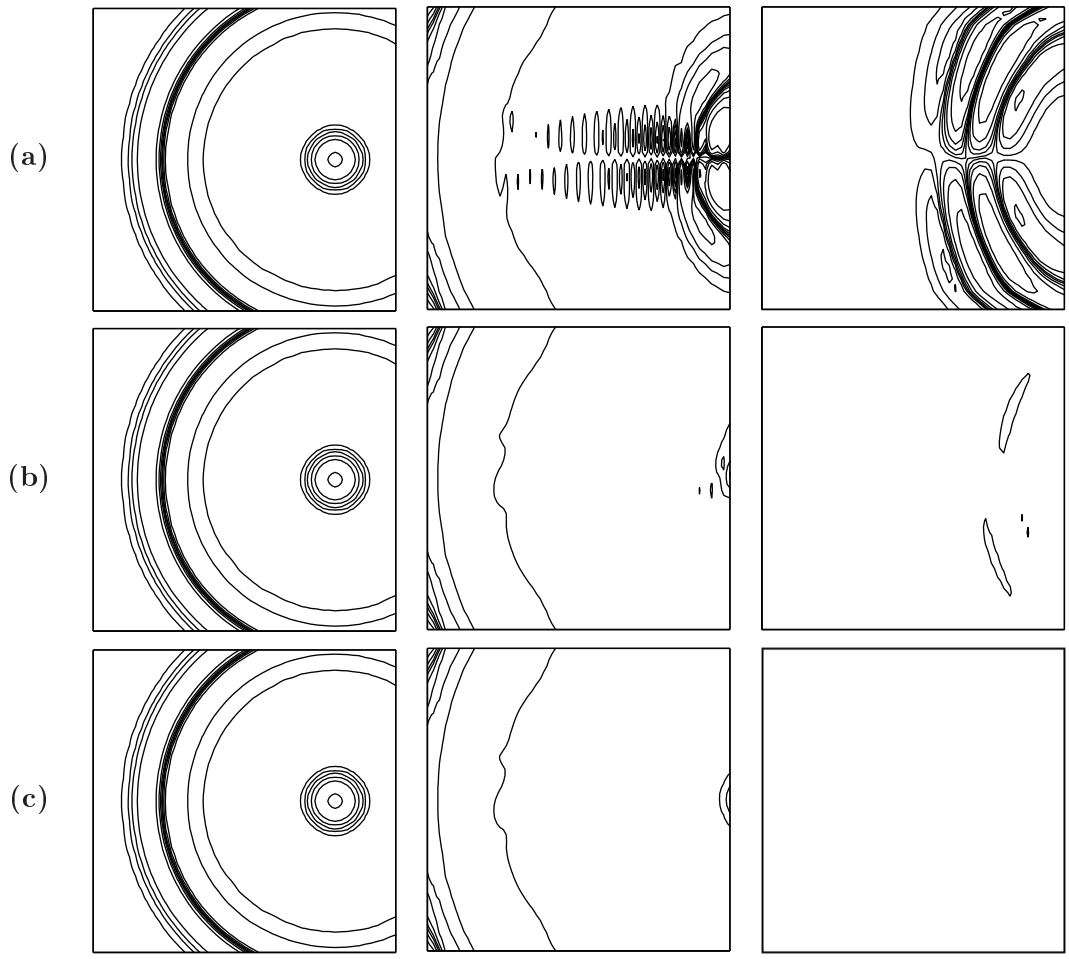

Figure 2.3: Iso-contours of the instantaneous pressure fields computed the left grid during the passage of the vortex through the overlapping region using Lagrangian polynomials of order **(a)** $N_{\text{order}} = 2$; **(b)** $N_{\text{order}} = 6$ and **(c)** $N_{\text{order}} = 10$.

N_{order}	2	4	6	8	10	single block
$L_2 \times 10^4$	7.637	1.630	1.164	1.104	1.097	1.096

Table 2.1: L_2 norm of error in swirl velocity after $N_{\text{it}} = 800$ iterations.

negligible. In order to reduce the effort in CPU and storage, the order of interpolation polynomials is limited to eighth-order for 2-D problems and to sixth-order for 3-D problems in this work.

2.2 Diffraction of monopolar acoustic source by a cylinder

This test case is issued from the second CAA workshop [1] and serves to check if sixth-order Lagrangian polynomials are sufficient to recover the accuracy of the high-order finite-difference schemes when only acoustic perturbations are involved. The numerical setup is represented in Figure 2.6. The test case solves the 2-D Euler equations in non-dimensional form. The reference length scale is the diameter of the cylinder d. A Gaussian shaped source, applied to the pressure after each Runge Kutta iteration,

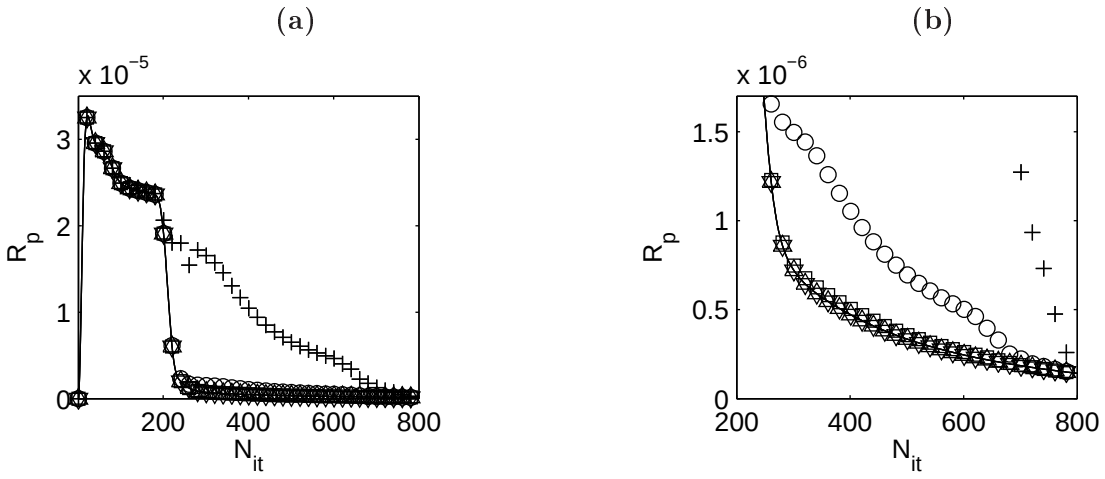

Figure 2.4: **(a)** Time evolution of the residual pressure L_p in left grid. **(b)** Detailed view on residual pressure L_p; ——— L_p of single block computation as reference solution; solution obtained with overset grid using interpolation of order + $N_{\text{order}} = 2$, ∘ $N_{\text{order}} = 4$, □ $N_{\text{order}} = 6$, △ $N_{\text{order}} = 8$, ▽ $N_{\text{order}} = 10$

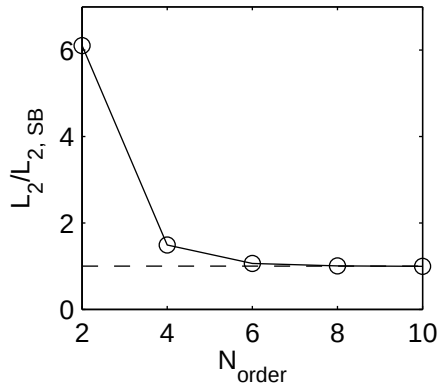

Figure 2.5: L_2 norm of the error of the swirl velocity normalized by the L_2 obtained for the computation on a single block.

is placed at $(x_s, y_s) = (4, 0)$:

$$S = \epsilon \sin(\omega t) \exp\left[\ln(2) \frac{(x - x_s)^2 + (y - y_s)^2}{b^2}\right],$$

where the frequency is given by $\omega = 8\pi$ and the Gaussian half-width by $b = 0.2$. Originally, the test case proposes to solve the linearized Euler equations. For the non-linear Euler equations a sufficiently small source strength ϵ has to be introduced, in order to avoid non-linear effects. In this work $\epsilon = 1. \times 10^{-6}$ has been chosen. For initial conditions air at rest at the pressure $p_0 = 1/\gamma$ and with the density $\rho_0 = 1$ is taken. The wave length associated to the source is $\lambda = c_0/4 = 0.25$. Since the wave length is of the same order as the source, the source is considered to be non compact.

A first simulation is done using a single cylindrical grid in order to validate for acoustic problems the slip wall condition developed in section 1.11. The grid consists of $N_r \times N_\theta = 781 \times 751 = 5.9 \times 10^5$ grid points and is spaced uniformly in r- and θ-direction. The number of points in azimuthal direction

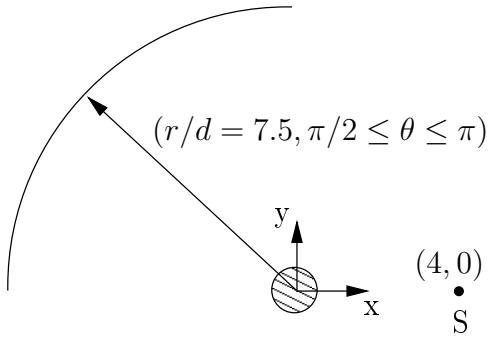

Figure 2.6: Configuration for the diffraction test cast: the time harmonic monopolar source is placed at point S. The directivity $D(\theta)$ will be measured on a arc at $r/d = 7.5$, $\pi/2 \leq \theta \leq \pi$.

N_θ is chosen to ensure a wave to be resolved by 7 points at $r/d = 7.5$. The number of points in radial direction N_r is taken to respect a ratio $\Delta r/\Delta\theta = 1.5$ at the cylinder wall.

Figure 2.7 **(a)** shows the simulated fluctuating pressure field. The acoustic waves coming from the non compact source generate a diffraction field. A silent zone behind the cylinder can be observed. The detailed view on the cylinder near region is given in Figure 2.8 **(a)**.

The directivity given by

$$D(\theta, r) = r\frac{1}{T}\int^{T} p'(\theta, r)^2 \, dt$$

is computed on a arc with $r/d = 7.5$ and $\pi/2 \leq \theta \leq \pi$ and is compared to the analytical solution of the problem [1]. In Figure 2.9 the directivity $D(\theta, r)$ obtained by computation is compared with the analytical solution. The computed curve and the analytical curve compare well.

In a second simulation, the same test case will be done using the overset-grid approach. By making several computations with different order of interpolation, the optimum interpolation order for the present numerical algorithm is determined.

The overset grid is composed of 2 grids: one cylindrical grid and one uniform grid. The uniform grid is generated to resolve acoustic wave with 7 points per wavelength $\Delta x = \Delta y = \lambda/7 = 1/28$. The uniform grid is extended $-10 \leq x, y \leq 10$. The cylindrical grid is spaced uniformly in azimuthal and radial direction and is limited by the outer radius $r_a/d = 1.5$. In the radial direction the grid length is chosen to be $\lambda/13$ and the number of grid points in azimuthal direction is taken to ensure that the aspect ratio of the radial and azimuthal grid spacing is $\Delta r/\Delta\theta = 1.1$. The overset grid contains 3.2×10^5 grid points, 45% less grid points than used for the single-block computation.

Figure 2.7 **(b)** shows the fluctuating pressure field for the overset grid using eighth-order interpolation polynomials. The diffracted field is very similar to the single-block computation. The detailed view on the cylinder near region is given in Figure 2.8 **(b)**. The acoustic waves propagates through the overlap region without generating spurious reflections.

In Figure 2.10 the quantity $D(\theta, r)$ along a line defined by $\theta = \pi/2$ and $0.5 \leq r/d \leq 10$ is compared with the analytical solution for the interpolation order of 2 and 6. Using second-order polynomials leads to large discrepancies in the near cylinder region. For polynomial orders higher than six, the error made by the interpolation procedure tends to zero.

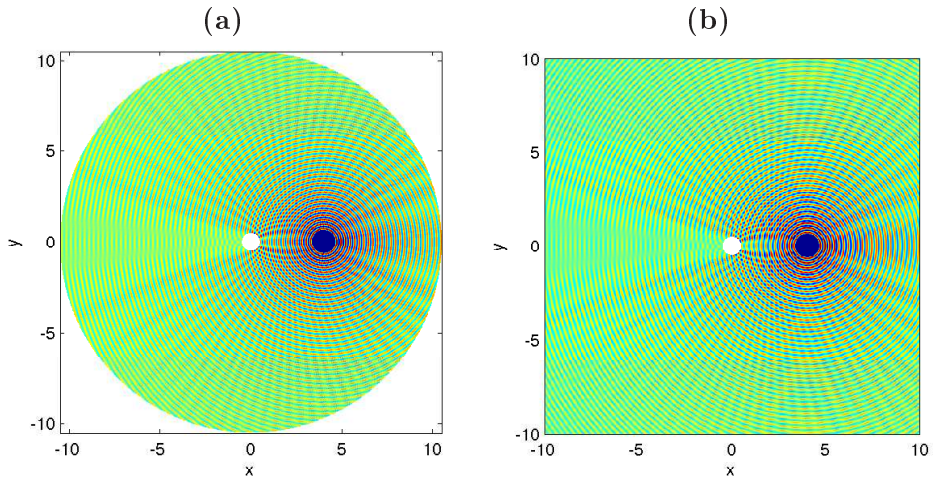

Figure 2.7: Diffraction of pressure source by cylinder: pressure fluctuations field (color scales $\leq 10^{-10}$ Pa) **(a)** obtained by single block computation; **(b)** obtained using overset grid approach and sixth-order interpoltion polynomials.

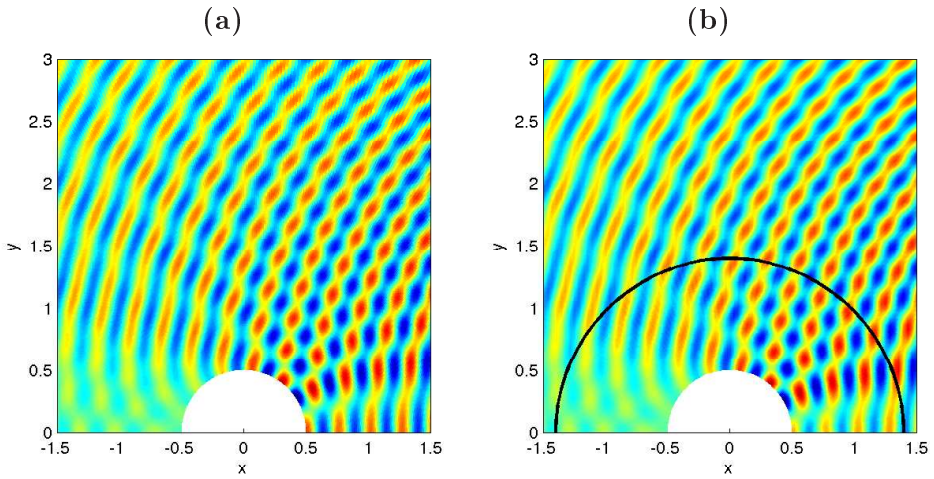

Figure 2.8: Diffraction of pressure source by cylinder: Detailed view pressure fluctuations field around the cylinder (color scales $\leq 10^{-10}$ Pa) **(a)** obtained by single block computation; **(b)** obtained using overset grid approach and sixth-order interpolation polynomials. The solid line presents the boundary of the cylindrical grid.

In this section, the overset approach has been successfully applied and the results compare very well with the analytical solution. The test cases reveals that sixth-order Lagrangian polynomials are sufficient when acoustic perturbations are involved in order to maintain the global accuracy of the 11-point finite-difference scheme.

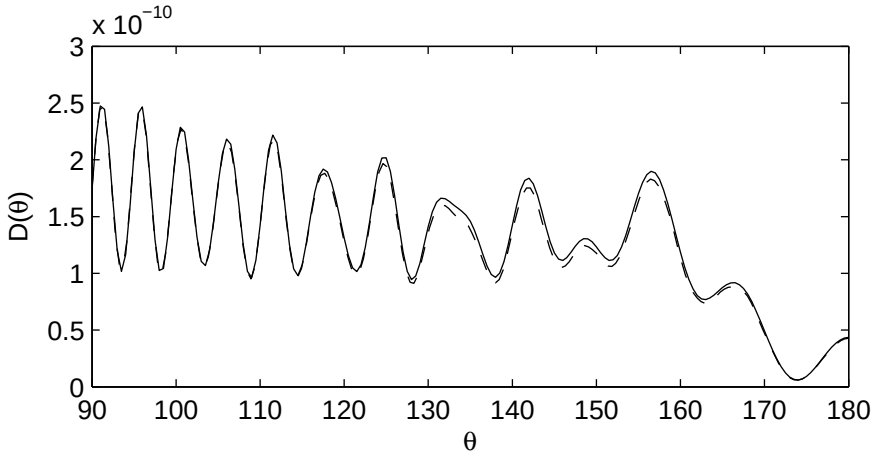

Figure 2.9: Directivity $D(\theta) = r < p'^2 >$ at $r/d = 7.5$: ——— computed solution; – – – analytical solution

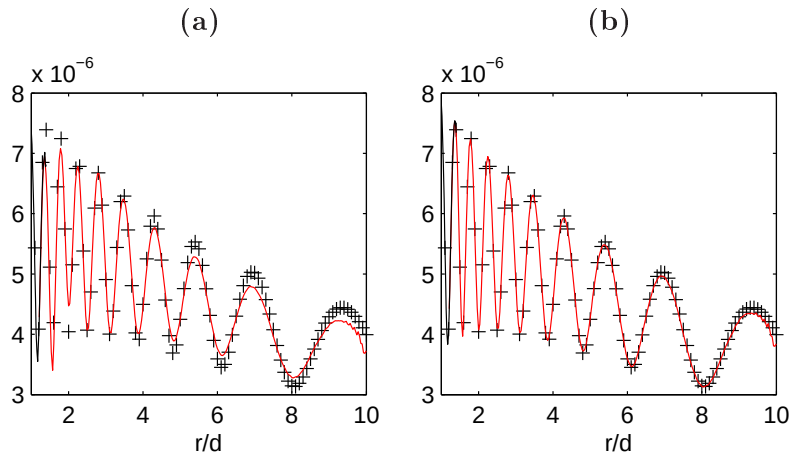

Figure 2.10: Directivity $D(\theta, r)$ at $0.5 \leq r/d \leq 10$ and $\theta = \pi/2$ for different order of interpolation: **(a)** 2 order **(b)** 8 order; —— computed solution; + analytical solution.

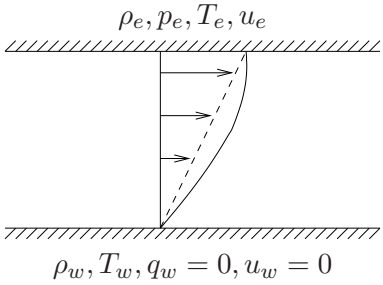

Figure 2.11: Sketch of the plane couette flow setup: the lower wall is adiabatic and at rest and the upper wall moves with a velocity u_e and is isothermal. $- - -$ Linear velocity profile for incompressible flows ——— Velocity profile for compressible flow with temperature dependent viscosity.

2.3 Plane compressible Couette flow

Following Gloerfelt [60] who computed a Poiseuille flow in 2-D, a compressible plane couette flow is considered. The test case allows to validate the implementation of the viscous and heat conduction terms as well as thermal boundary conditions, reported in section 1.11. At the same time this test case introduces some physical concepts encountered in compressible viscous flows.

The flow configuration is shown in Figure 2.11. Air flows between two parallel plates, where the upper plate moves at a constant velocity u_e relative to the lower plate. The other boundary conditions are as shown. The temperature at the upper and lower plate are designated T_e and T_w, respectively. A heat flux is imposed at the lower wall and the upper wall is isothermal. The 2-D flow is fully developed in x-direction so that $\partial/\partial x = 0$ and is steady $\partial/\partial t = 0$. The continuity equation writes

$$\frac{\partial(\rho v)}{\partial y} = 0.$$

The momentum equations give

$$\frac{\partial \tau_{xy}}{\partial y} = \frac{\partial}{\partial y}\left(\mu \frac{\partial u}{\partial y}\right) = 0,$$

$$\frac{\partial p}{\partial y} = 0.$$

Thus, shear stress and pressure in wall normal direction are constant. For incompressible flows, the viscosity is often taken to be constant [119] and integration leads to a linear profile. For compressible flows, variations in temperature produce variations in viscosity. The temperature distribution needs therefore to be known in order to integrate the momentum equation. This temperature is determined by means of the energy equation that reduces to

$$\frac{\partial}{\partial y}\left(\mu u \frac{\partial u}{\partial y} + k \frac{\partial T}{\partial y}\right) = 0,$$

showing that for the Couette flow the diffusion of kinetic energy and heat conduction are in equilibrium. The equation is integrated from the lower wall outwards:

$$\mu u \frac{\partial u}{\partial y} + \frac{\mu c_p}{Pr} \frac{\partial T}{\partial y} = -q_w.$$

By noting that the shear stress is constant and by assuming a constant Prandtl number, the equation is recasted in

$$\frac{\partial}{\partial y}\left(C_p T + \frac{1}{2} Pr\ u^2\right) = -Pr\ \frac{q_w}{\tau_w}\frac{\partial u}{\partial y}$$

and is integrated to obtain a relation between the temperature and the velocity distribution.

$$C_p(T - T_w) + \frac{1}{2} Pr\ u^2 = -Pr\ \frac{q_w}{\tau_w} u.$$

The lower wall is taken adiabatic ($q_w = 0$) which allows to determine the temperature at the lower wall directly by the expression

$$T_w = T_e + \frac{1}{2}\frac{Pr\ u_e^2}{C_p}.$$

The adiabatic wall temperature is called the recovery temperature and is for the stationary wall equal to the total temperature. When the Prandtl number is not equal to 1 the total temperature of the outer flow is not recovered entirely at the lower wall in form of heat. The momentum and energy equations are integrated numerically from the lower wall outwards to the upper wall leading to an exact temperature and velocity distribution. The temperature dependency of the viscosity is taken into account by Sutherland's law given by (1.15).

In order to study the grid convergence, three computations on a 2-D uniformly spaced grid are carried out with different numbers of grid points. The number of grid points in x-direction is kept constant $N_x = 10$, whereas the grid points in y-direction are taken $N_y = 21, 50$ and 100. Note that for the coarsest grid, only ten points are computed with the centered finite-difference scheme. The boundary points are computed using the non-centered finite-difference schemes and selective filters proposed by Berland *et al.* [21].

The conditions at the upper wall are taken to be ambient $p_e = 1.0 \times 10^5$ Pa and $\rho_e = 1.2\text{kg.m}^{-3}$. A Reynolds number based on the height H and the upper velocity u_e, and the viscosity measured at the upper wall is $Re = 800$. The Mach number is taken to be $M_e = 2.33$. Adiabatic no-slip boundary conditions and constant temperature conditions reported in section 1.11 are applied at the lower wall and upper wall respectively. Periodic boundary conditions are applied in x-direction.

The computation is initialized using the linear incompressible velocity profile and a constant pressure and temperature profile at ambient conditions. The computations are carried out until the density residual reaches $|\rho^{n+1} - \rho^n|/\rho^n \leq 10^{-6}$. The convergence rate for the three cases are provided in Figure 2.12 **(a)**. Note for all computations, the time step is equal and is governed by the constant grid size in the x-direction.

The computed velocity profiles are given in Figure 2.12 **(b)**. In agreement with the exact solution, the computed velocity profiles exhibit a difference due to the variation of viscosity. The coarse grid solution reveals some discrepancies. By refining the grid, the computed solution converges to the exact solution. The same tendency can be observed for the temperature profiles given in Figure 2.13 **(a)**. It increases and converges to the recovery temperature near the wall. The error, defined by the absolute difference between the exact and computed recovery temperature, are plotted in Figure 2.13 **(b)** as a function of the grid size. The error scales with the grid size at the power of 6.2.

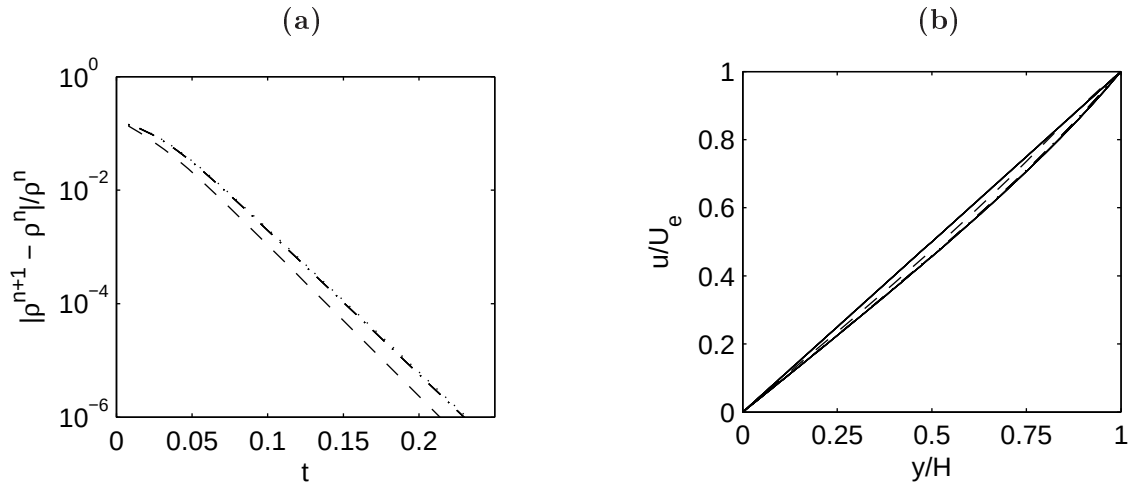

Figure 2.12: **(a)** Time evolution of density residual; **(b)** Comparison of velocity profiles computed with different grid sizes (– – – $\Delta y = 1/20$, – · – · $\Delta y = 1/50$, ····· $\Delta y = 1/100$) with the exact solution ———. The straight line $u/U_e = y$ represents the linear velocity profile for the incompressible case.

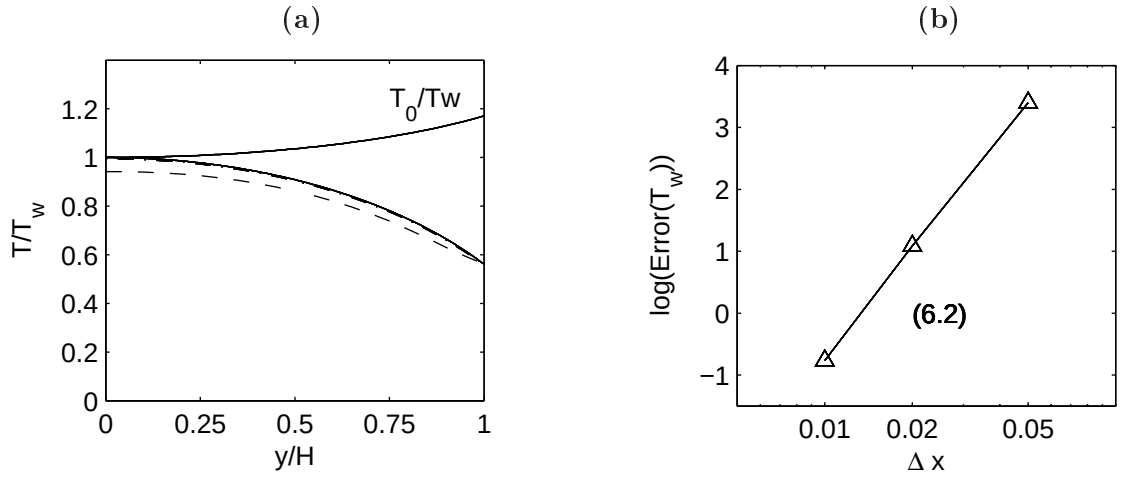

Figure 2.13: **(a)** Comparison of temperature profiles computed with different grid sizes (– – – $\Delta y = 1/20$, – · – · $\Delta y = 1/50$, ····· $\Delta y = 1/100$) with the exact solution ———. The upper solid lines represents the distribution of the total temperature $T_0 = T + 0.5u^2/C_p$; **(b)** Difference between computed and exact adiabatic wall temperature T_w.

The computation of the plane Couette flow demonstrates that compressible viscous and thermal interactions governed by the Prandtl number are predicted correctly by the numerical code. The implementation of the adiabatic boundary conditions is robust and predicts the recovery temperature correctly.

2.4 Flow around cylinder at low Reynolds and low Mach number

In this section, the simulation of a 2-D flow around a cylinder at low Reynolds and Mach number is presented. This flow configuration has been studied by Marsden *et al.* and Inoue and Hatakeyama

[92, 72] using a single cylindrical grid. The flow is solved using the overset-grid approach and compared with the computed solution of the literature [72].

The diameter of the cylinder is $D = 2.0 \times 10^{-5}$ m and the flow Mach number is $M_\infty = 0.33$. For air at ambient conditions $p_\infty = 1.0 \times 10^5$ Pa and $\rho = 1.2$ kg.m^{-3} the Reynolds number based on the cylinder diameter is computed $Re_D = 150$. In the experiments, no transition and no 3-D effects are observed [144] for this Reynolds number and the problem can be simulated using a 2-D mesh.

The grid generated by *ogen* is shown in Figure 2.14. It consists of 5 component grids: the grid around the cylinder, the grid in the wake of the cylinder, a highly stretched grid at the outflow boundary and a far-field grid in order to propagate the acoustic field. The minimum grid size is governed by the boundary layer that develops along the cylinder wall. A grid size in radial direction of $\Delta r = D/36$ is used. With this grid resolution the boundary layer near the stagnation contains 4 grid points. In azimuthal direction 251 uniformly spaced grid spacing are used. The grid size of the wake grid has been adapted to cylindrical grid in order to avoid great variation of cell sizes in the wake of the cylinder. The wake grid spreads in y-direction and matches the height of outflow. The outflow grid is highly stretched with exponential functions provided by *ogen*.

The grid size for the acoustic grid is determined as follows. A Strouhal number of $St_D = f\ D/U_\infty = 0.18$ is expected, giving a wavelength of $\lambda_a = (1/M_\infty - 1)/St\ D = 11.3D$ for upstream traveling perturbations. The 11-point optimized scheme is able to propagate perturbations over far distances with 7 points per wavelength imposing a grid size of $\Delta x = \lambda_a/7 = 1.6D$. The dimensions of the far-field grid are chosen such as 5 wavelengths fit between the cylinder and the computational boundaries in upstream direction.

Additionally, one intermediate grid is used in order to avoid large variation of grid sizes in the overlap zones due to the large disparity between the grid around the cylinder and its wake and the coarse far-field grid. A detailed view on the near cylinder region provided in Figure 2.15 shows the cylindrical grid and the wake grid embedded in the intermediate grid. The grid characteristics are detailed in Table 2.2.

At the wall adiabatic non-slip conditions are applied and a simulation time corresponding to 100 vortex shedding periods is affected. The chosen CFL = 0.4 results in a time step of $\Delta t = 4.28 \times 10^{-10}$ s.

	N_x	N_y	N_{tot}	N_{procs}
Cylinder grid	251	60	7530	2
Wake grid	945	164	14089	11
Outflow grid	359	235	10545	8
Far field grid	168	168	9408	3
Intermediate grid	429	133	11411	5

Table 2.2: Grid characteristics for the computation of the flow around a cylinder. The total number of 3.4×10^5 grid points have been computed by $N_{\text{procs}} = 29$ processors.

Figure 2.16 shows the instantaneous plot of the pressure fluctuation field $p - p_\infty$. The dipole

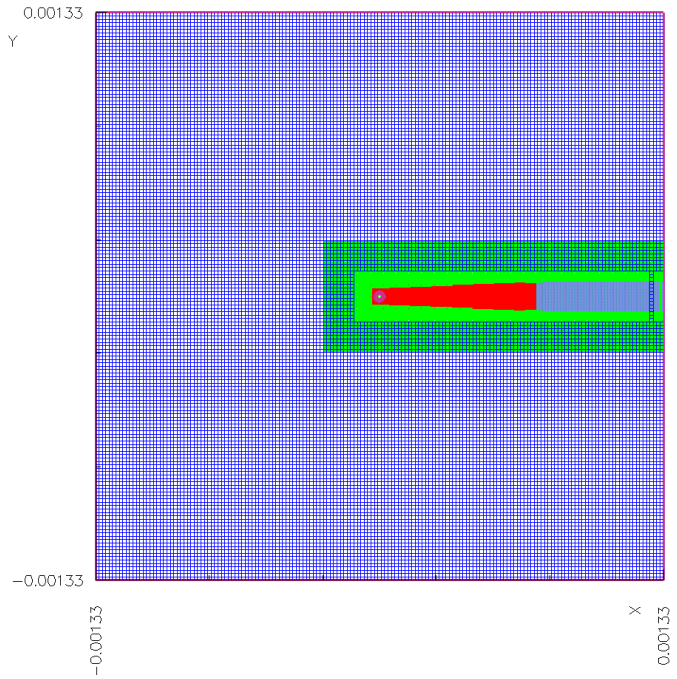

Figure 2.14: Overset grid generated by *ogen*. The grid is composed of 5 component grids: cylindrical grid (magenta), wake grid (red), outflow grid (blue), intermediate grid (green), acoustic grid (blue).

character of the noise source is observed. The presence of a mean flow leads to the compression of acoustic wave length in the upstream direction, similar to the Doppler effect. Figure 2.17 shows the instantaneous vorticity field. The Von Kármán vortex street is visible.

The mean pressure coefficient defined by

$$C_p = \frac{p - p_\infty}{1/2\rho_\infty v_\infty^2}$$

is compared to the solution obtained by Inoue *et al.* [72] in Figure 2.18. The solution compares well with the solution obtained by Inoue. Some discrepancies can be observed in the stagnation point and on the forward facing cylinder side where the flow separates.

The drag coefficient based on the pressure forces is computed such as $C_d = 1.25$ and compares well with the experimental values $C_d = 1.32$. The error is 5.3% and is associated to the coarse grid used for the grid in the computation. Slight deviation of 5% can be observed for the Strouhal number that is found to be 0.193 which is caused to by the underresolution of the flow.

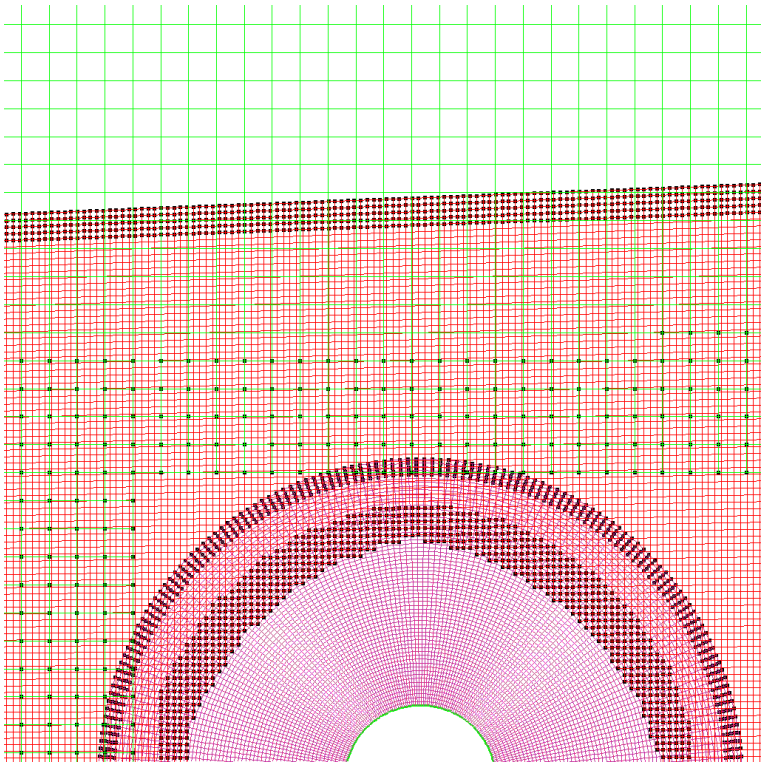

Figure 2.15: Overset generated by *ogen*. The detailed view on the cylinder region shows cylindrical grid embedded in the wake grid. Additionally, an intermediate grid is added in order to avoid large changes in grid size. Black markers visualize interpolation points.

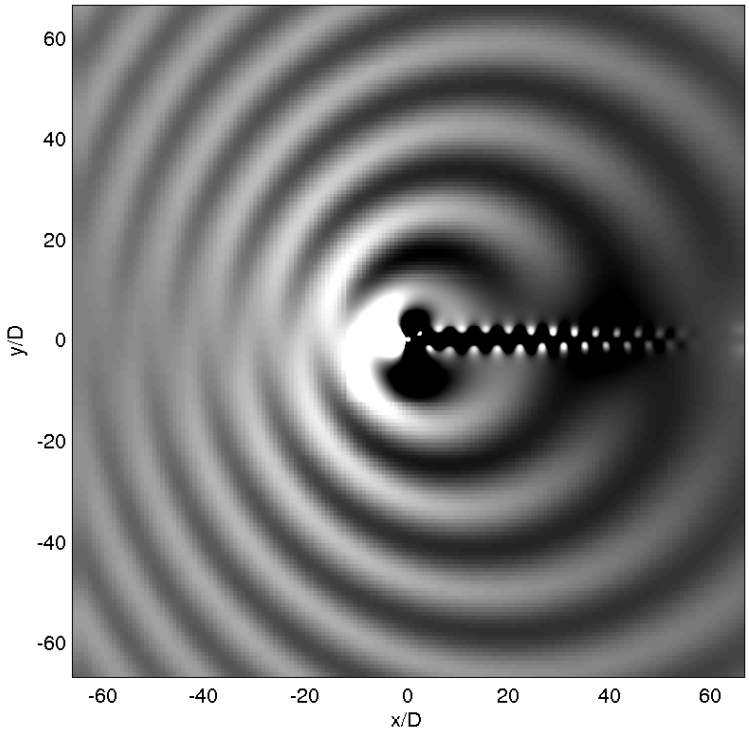

Figure 2.16: Instantaneous pressure fluctuations field (gray scales $|p'| \leq 200$ Pa).

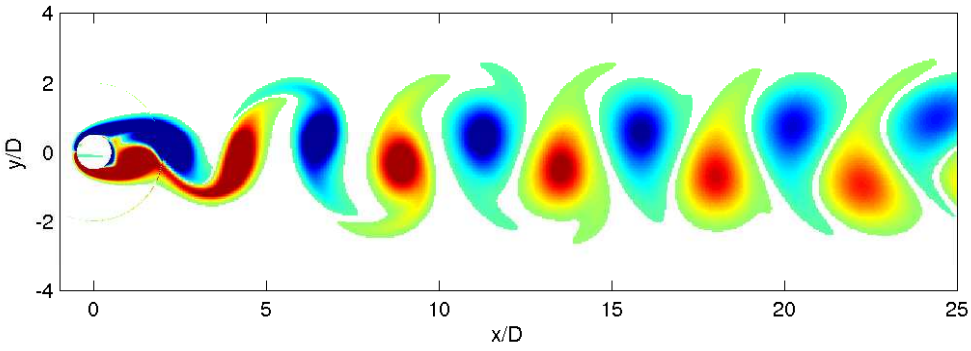

Figure 2.17: Instantaneous vorticity fluctuations field (color scales $0.1 \leq |\omega| \leq 6.6 \times 10^6$ s^{-1}).

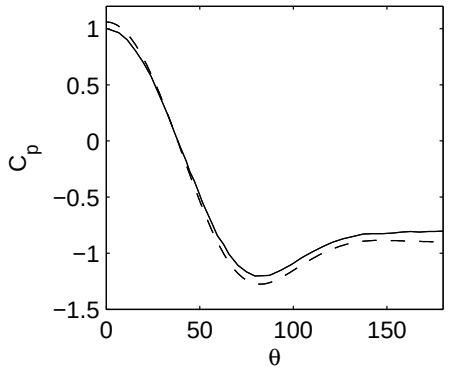

Figure 2.18: Pressure coefficient along the cylinder surface: —— solution provides by Inoue *et al.* [72]; - - - - computed solution.

2.5 1-D Shock/Entropy Wave Interaction

The next example considers the 1-D inviscid flow proposed by Shu and Osher [117] as a model problem for shock-turbulence interaction. This test case, which incorporates both fine-scale and strong nonlinear features, consists of a moving Mach 3 shock wave interacting with a density fluctuation. The domain extends from $-5 \leq x \leq 5$. The initial condition is specified as follows.

$$[\rho, u, p] = \begin{cases} [3.857143, 2.629369, 10.333333] & \text{for} \quad x < -4, \\ \\ [1 + 0.2\sin(5x), 0, 1]] & \text{for} \quad x \geq -4 \end{cases}$$

The solution is advanced in time until $t = 1.8$ and the density distribution obtained with the present numerical algorithm on a 1601 point mesh is displayed in Figure 2.19 as well as the initial condition. A courant number of CFL $= 0.1$ is used in order to minimize the error form the Runge-Kutta scheme. This solution is considered as the reference solution.

Figures 2.20 **(a)** and **(b)** show the solution obtained on a 401 points mesh and 201 points mesh respectively. Three computations have been carried out with different filtering strategies. One computation is done using the centered selective filter scheme alone. Two further computations are carried out applying the shock capturing filter presented in section 1.6 after each time iteration with the Jameson detector and with the modified Jameson detector based on the 11-point selective filter.

The solution computed with the selective filtering only compares well with the reference solution on both grids even if a small dispersion error is observed. The use of the shock-capturing filter leads to a slight underestimation of the density perturbations which becomes more obvious for the coarse mesh computation. The solution obtained with the modified Jameson detector leads to lower amplitude error due to a smaller peak value of the detector in the shock region.

This test case shows that the numerical scheme is able to treat problems with strong non-linearities. Using the selective filter is sufficient to ensure stability and to provide an high-order accurate solution. An influence of the shock-capturing filter can be observed, but can be minimized by using the modified Jameson detector. Comparisons with computations found in the literature show that the implemented scheme is competitive with more sophisticated shock-capturing filters based on MUSCL or WENO schemes for example considered recently by Visbal and Gaitonde [137] or Lo *et al.* [89].

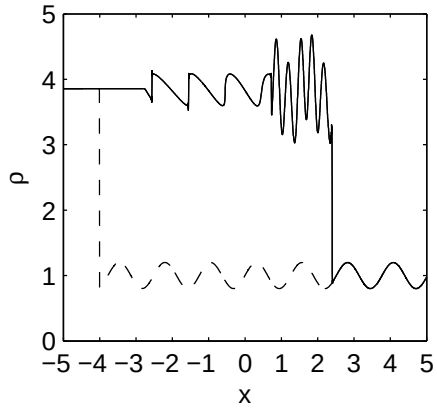

Figure 2.19: 1-D entropy wave/ shock interaction problem: – – – initial condition and ——— solution at $t = 1.8$ obtained on 1601 point mesh.

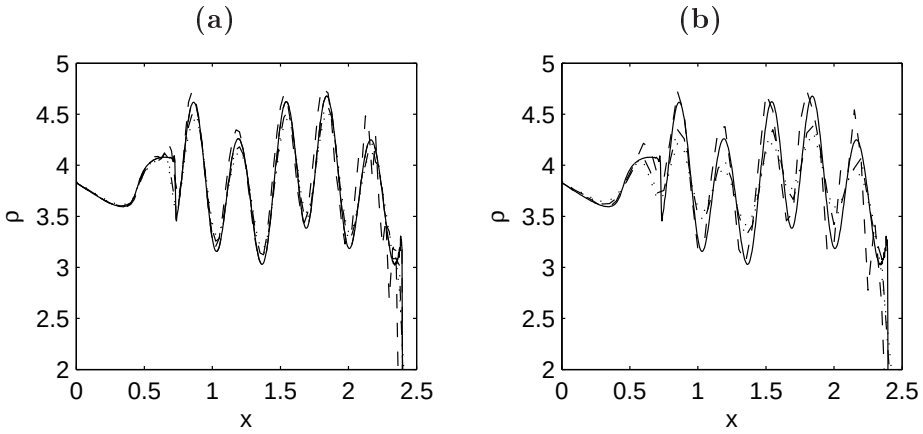

Figure 2.20: 1-D entropy wave/shock interaction problem at $t = 1.8$: **(a)** 401 point mesh; **(b)** 201 point mesh; ——— reference solution, – – – selective filtering, ····· selective filtering + shock capturing, – ·– · selective filtering + shock capturing + modified Jameson detector.

2.6 1-D shock/sound interaction in a convergent divergent nozzle

The flow in a convergent-divergent nozzle is simulated. The test case is taken from the third CAA workshop [2] and proposes to solve the 1-D Euler equations with variable cross-section. The equations in conservative form can be written as

$$\frac{\partial(A\mathbf{Q})}{\partial t} + \frac{\partial(A\mathbf{E})}{\partial x} + \mathbf{H} = 0, \tag{2.1}$$

where the vector $\mathbf{Q} = [\rho, \rho u, \rho e]^T$ contains the unknowns, $\mathbf{E} = [\rho u, \rho u^2 + p, (\rho e + p)u]^T$ is the flux vector and $\mathbf{H} = \ dA/dx \times [0, p, 0]^T$ is the source vector that takes into account the variation of the cross-section area. The equations are non-dimensionalized by the flow properties at the duct inflow. In the same way, the cross-section area $A(x)$ is scaled by its value at the inflow and is given by:

$$A(x) = \begin{cases} 1.0 - 0.661514 \exp\left[-(\ln 2)(x/0.6)^2\right], & x < 0 \\ \\ 0.536572 - 0.198086 \exp\left[(-(\ln 2)(x/0.6)^2\right], & x \geq 0. \end{cases}$$

The equations are solved on a uniform grid that contains 351 points and the solution is advanced in time with CFL=0.1 in order to make the error of the time integration scheme negligible. Non-reflecting boundary conditions are implemented using characteristic boundary conditions at the inflow and the outflow. The Mach number is fixed at the inflow of the duct ($M_{\text{in}} = 0.2006533$). Imposing weakly the pressure at the outflow ($p_{\text{out}} = 0.6071752$) using using a relaxation term given in equation (1.16), leads to a normal shock in the divergent part of the duct.

Three simulations are carried out using the selective filter only, using the selective filter in combination with the shock capturing filter with the classical Jameson detector and using the modified Jameson detector based on the 11-point selective filter. Figure 2.21 gives the mean flow quantities for the three computations. Using no shock-capturing terms generates overshoots around the discontinuities. They are associated with the classical Gibbs phenomenon, which is typical for high-order methods. The use of the shock-capturing filter removes the overshoots and the shock is well captured. The overshoots for the modified Jameson detector are more present than with the classical Jameson detector indicating that less dissipation is introduced.

Once the mean field is converged after about 100000 iterations, a harmonic acoustic perturbation (10^{-5} order of magnitude, $\omega = 0.6\pi$) is superimposed at the inflow in order to study shock-sound interaction. Figure 2.22 displays the fluctuating pressure field for the three cases. All solutions compare well with the solution given by Hixon [2]. The overshoots observed in the mean flow profile when no shock-capturing scheme is used have no impact on the acoustic signal. Furthermore, no influence of the low-order shock-capturing terms can be observed. This is not surprising because the acoustic perturbations are resolved with about 25 mesh points per wavelength.

Pushing the test case to its limits reveals the influence of the shock-capturing term. For that, the computations are repeated involving a signal which contains only 7 points per wavelength. The fluctuating field is given in Figure 2.23. Provided that 4 points per wavelength are the accuracy limit of the finite-difference scheme, the solution obtained without shock-capturing is considered as a reference

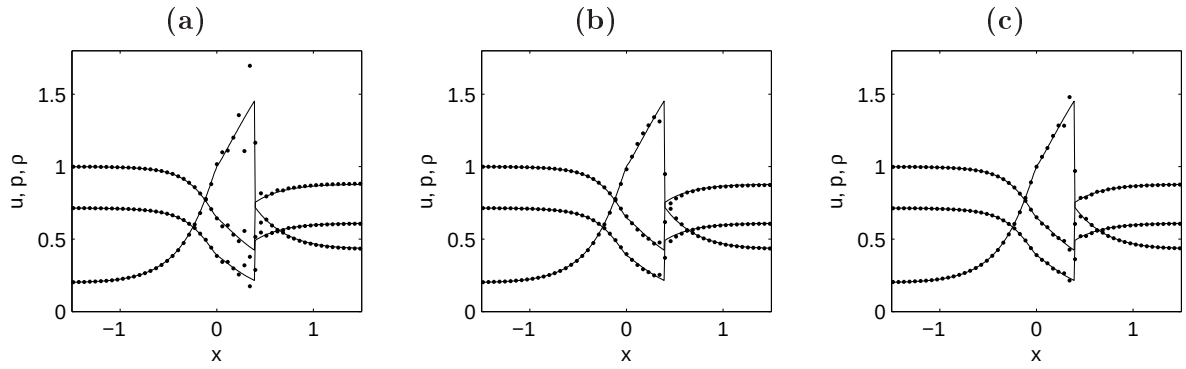

Figure 2.21: Acoustic wave/shock interaction problem in a convergent divergent nozzle: mean properities (ρ, p, u) obtained **(a)** with selective filter, **(b)** with selective filter + shock capturing filter, **(c)** with selective filter + shock capturing filter + modified Jameson detector.

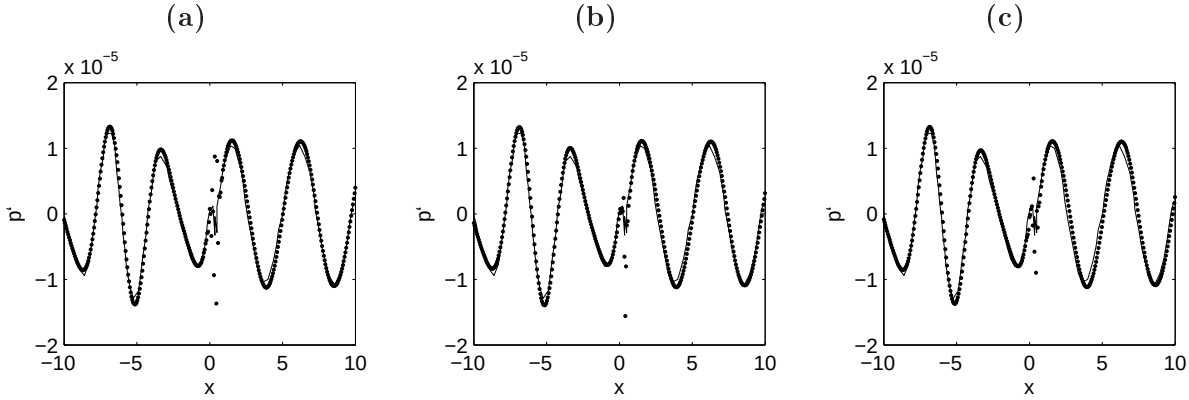

Figure 2.22: Acoustic wave/shock interaction problem in a convergent divergent nozzle: fluctuating pressure obtained **(a)** with selective filter, **(b)** with selective filter + shock capturing filter, **(c)** with selective filter + shock capturing filter + modified Jameson detector.

solution. Applying the shock-capturing leads to the damping of the signal downstream of the shock. The computation using the shock-capturing filter with the modified Jameson filter gives a slightly less damped signal thanks to less dissiption that is introduced in the shock region.

The computation of sound/shock wave interactions in a 1-D divergent convergent nozzle has shown that the present algorithm is able to deal with problems involving several orders of magnitude.

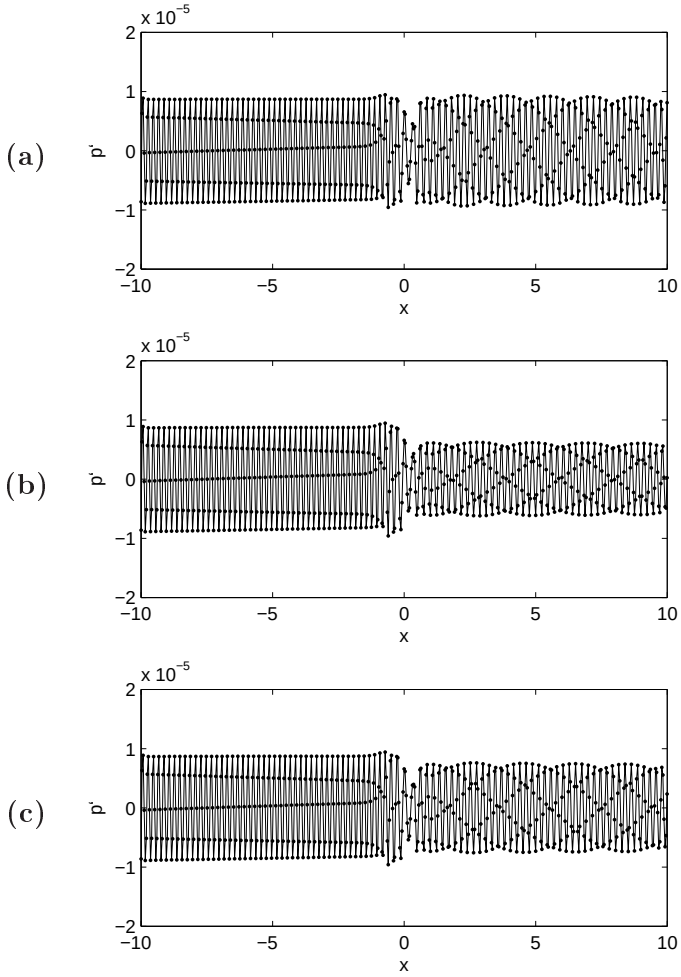

Figure 2.23: Acoustic wave/shock interaction problem in a convergent divergent nozzle: fluctuating pressure field for the high frequency case obtained (acoustic wave is resolved with approximately 7 points per wave length) **(a)** with selective filter, **(b)** with selective filter + shock capturing filter, **(c)** with selective filter + shock capturing filter + modified Jameson detector.

2.7 Inviscid flow in 3-D circular shock tube

The transonic flow of section 2.6 is now studied in a 3-D circular duct. The grid generated by *ogen* is represented in Figure 2.24 **(a)**. For cylindrical grids a singular point arises in the center ($r = 0$). The overset-grid approach can easily avoid such singularity problems by decomposing the geometry in two component grids.

A first axis-symmetric grid with varying cross-section is generated. The centerline at $r = 0$ is omitted by this grid. The external radius is given by $r_{ex}(x) = \sqrt{A(x)/\pi}$ and internal radius by $r_{in} = 0.3 r_{ex}(0)$. A second Cartesian is embedded at the centerline of the cylindrical grid as displayed in Figure 2.24 **(b)**. The overlap is built for a interpolation of order 6. The cylindrical grid contains $301 \times 50 \times 80 \approx 1.2 \times 10^6$ points and the Cartesian grid $301 \times 31 \times 31 \approx 0.3 \times 10^6$ points. At wall the slip condition of section 1.11 is applied and characteristic boundary conditions are applied at the in- and outflow.

The simulation is carried out for 1×10^5 iterations with a CFL number of CFL $= 0.9$. The non-linear shock-capturing filter described in section 1.6 is applied, in order to maintain numerical stability. The computation is performed on 30 processors.

The Mach number field computed in a $x - r$ plane is represented in Figure 2.25. The iso-contours of the Mach number match very well in the overlap region. The normal shock passes the overlap region without any spurious oscillations. The mean flow properties u, ρ, p along the centerline are compared in Figure 2.26 with the analytical solution of the 1-D problem given by Hixon [2]. They are in good agreement. In particular, the shock location is correctly predicted indicating the good conservativity of the scheme.

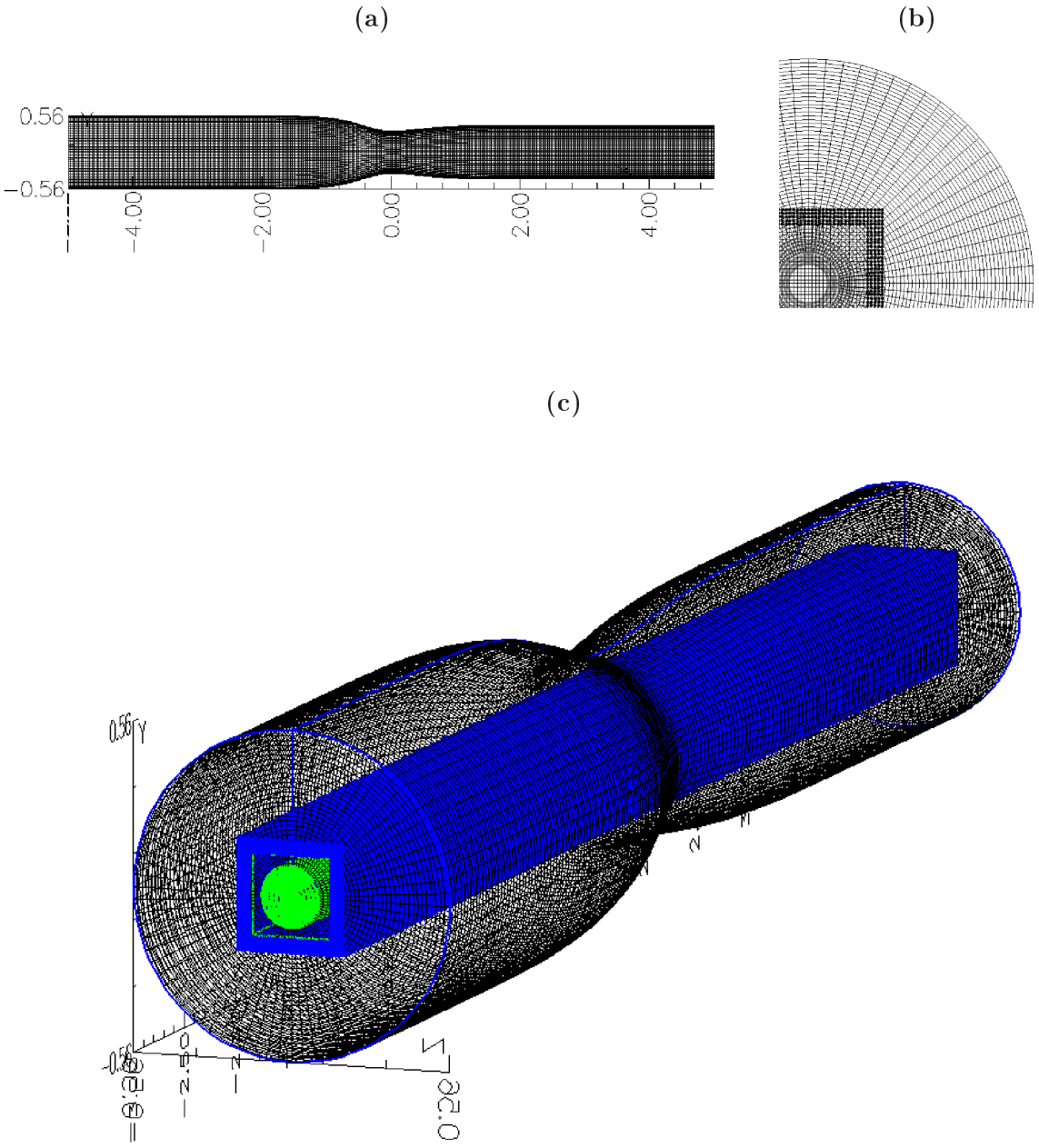

Figure 2.24: Grid of the circular convergent divergent nozzle: **(a)** Side view; **(b)** Sectional view at $x = -5$: black and gray squares indicate the interpolation points of the Cartesian grid and the cylindrical grid respectively; **(c)** Grid of the circular convergent divergent nozzle: 3-D view

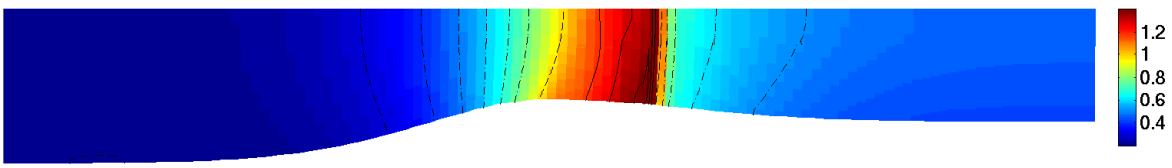

Figure 2.25: Mach number profile in a $x - r$ plane for $-2 \leq x \leq 2$. Iso-contours of the Mach number $M > 1$, $- \cdot - \cdot -$ $M = 1$, $- - -$ $M < 1$.

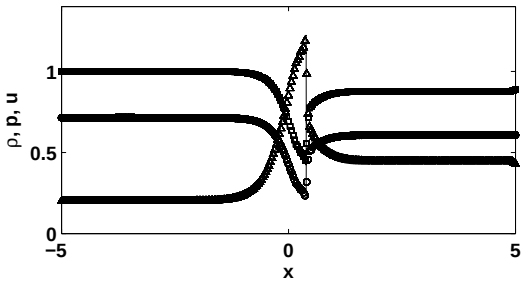

Figure 2.26: Centerline profiles of u, p ρ (top down). The symbols correspond to the numerical solution and the solid line to the analytical solution.

2.8 Conclusion

In this chapter, SAFARI has been validated with various classical test cases given in the literature.

The test case of the convection of a vortex through an overlap region has shown that the accuracy of the optimized finite-difference scheme can be recovered using at least sixth-order or better eighth-order Lagrangian polynomials. The case of the diffraction of the monopolar source by a cylinder demonstrates that sixth-order polynomials are sufficient when only acoustic perturbations are involved. Using *ogen* the user is able to specify polynomial order for each inter-grid communication, this study allows to minimize communication costs due to interpolation by using very high-order interpolation in non-linear zones such as wakes or shock regions and to use smaller interpolation stencils linear regions without passing vortical structures.

The second part of validation is concerned to the shock treatment. For that a Jameson-type dissipation model has been implemented. This scheme has very good shock-capturing properties. The example of a 1-D entropy/ shock wave interaction reveals that the nonlinear filtering terms risk to damp out small scale perturbations. The same is observed for acoustic/shock wave interaction problems. The dissipation can be minimized by using a modified Jameson detector based on high-order dissipation terms. The computational efficiency of the Jameson-type filter schemes have made them to the prefered shock treatment in this work.

Using the overset-grid approach complex geometries can be treated now in a autmated manner. In this work, the grid assembler package *ogen* has been used to generate the complex data structure required for the overset-grid approach. This is demonstrated for the 2-D low Reynolds number flow as well as for the computation of a 3-D circular shock tube. The latter example shows the grid flexibilty that SAFARI offers now.

Chapter 3

Aeroacoustic simulation of a ducted cavity flow

The configuration of the present ducted cavity has been studied in the context of an industrial application. Tonal noise has been measured on the power steam line of a nuclear power station and the cavity located at the bottom of a gate valve, as shown in Figure 1 **(b)**, has been identified as the main noise source. This cavity has two specific characteristics from more classical cavities studied in the literature: it is confined in a duct and partially covered.

Due to the geometrical complexity of the cavity, a simplified planar model has been first studied numerically and experimentally by Lafon *et al.* [81]. The retained geometry is reported in Figure 3.1. The cavity is a shallow cavity since the aspect ratio is $L/h = 2.5 > 1$ [112].

Confined cavities can not be only found in pipe systems with flow control devices but also in organ pipes or flutes for instance. They generate discrete tones that can be either disturbing when they excite the natural modes of pipe structure or desirable for musical instruments.

In this chapter the simulation of a confined cavity is presented. First, the physics of the cavity flow is summarized and the experimental results of the studied cavity configuration are discussed. Then, the results of the simulation are presented and validated with the experiments.

3.1 Introduction to cavity flow

Cavity flow can be found in many applications and many experimental studies about the self-sustained oscillations of cavity flow have been carried out in the last 50 years. Review articles are provided by Rockwell and Naudascher [108], Komerath *et al.* [80], Colonius [37] and Tadeka and Shieh [122].

The self-sustained oscillations is based on a feedback mechanism that can be decomposed in two phases. First vortical structures are triggered at the upstream angle of the cavity. Due to Kevin-Helmholtz instability, vortical structures develop and grow in the turbulent or laminar shear layer above the cavity.

Vortices are convected over the cavity and interacts with the downstream angle. The impact of the eddies on the downstream angle leads to perturbations that trigger further instabilities at the upstream

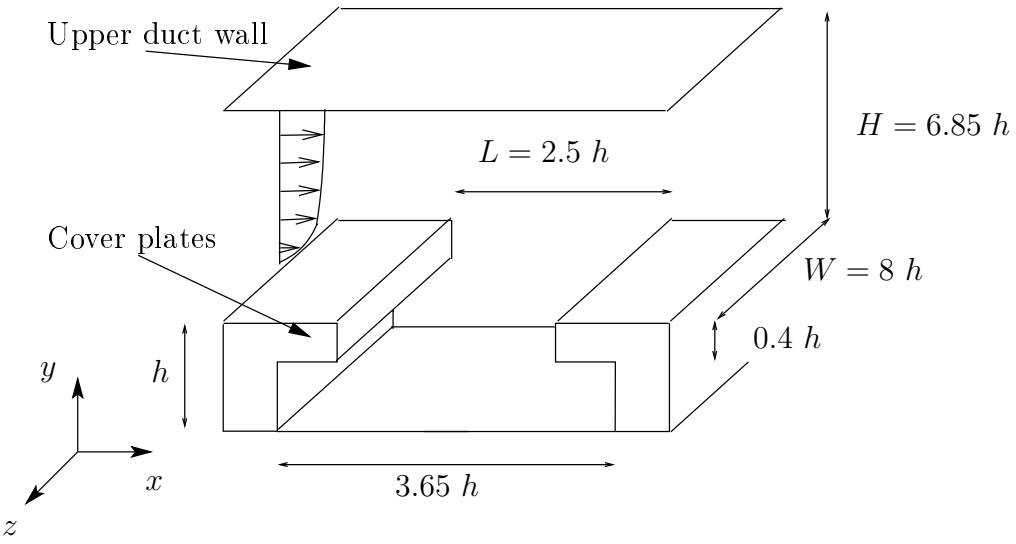

Figure 3.1: Ducted cavity: sketch of the geometry and notations $h = 0.02$ m, $d = 0.05$ m, $H = 0.137$ m, $L = 0.073$ m and $W = 0.16$ m. The aspect ratio of the cavity is $L/D = 2.5$. U_0 is the free stream velocity.

cavity angle resulting in phase-locked frequencies. Note that for incompressible flows (water or air at small Mach number $M < 0.3$) the feedback loop closes rather via a hydrodynamic mechanism. Using the Biot and Savart law, vortex deformation can be associated with a perturbation at the upstream cavity angle [9]. For compressible flows ($M > 0.3$), the wavelength of acoustic perturbations is of the same order as the cavity length L. The instability is triggered by an acoustic wave that is generated by the impact of the vortical structure on the downstream angle. The emission of acoustic waves have been visualized by Karamcheti [76].

Many models have been designed to predict the frequencies of the self-sustained oscillations. Models for the estimation of the amplitude are rare due to the number of parameters that comes into play. For example, Karamcheti [76] found that self-sustained oscillations occur for cavities exceeding a characteristic length L and that the frequencies scale with the reciprocal of the cavity length L. Furthermore the incoming boundary layer thickness has an influence on the sound pressure level. For laminar boundary layers, the amplitude of the resonance frequencies are increased. For turbulent boundary layers, the spectral content features more peaks. Sahoria [112] found that oscillations of cavity flows occur above a certain value of the ratio L/δ_θ, where δ_θ is the momentum thickness of the incoming boundary layer. The influence of width W has been examined by Ahuja and Mendoza [3] and found small influence of the width on the pressure spectra. However Tracy and Plentovich [133] confirm this only for deep cavities with $L/D < 2$. For shallow cavities $L/D > 2$, they observed an increase of peak levels for small width W. The same authors found that for subsonic cavity flows the broadness of the peak of the pressure spectra increases which is due to a decrease of flow coherence. Cavity flow at supersonic speeds are not considered in this work. For further lecture refer to the work of Heller and Bliss [66] and Larchevêque [85] for example.

In the past, several analytical investigations about cavities have been done. The most important

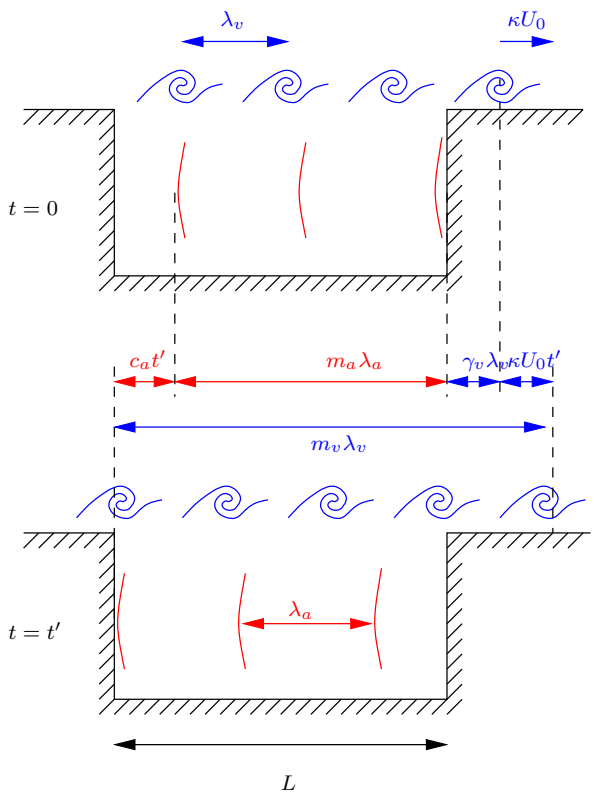

Figure 3.2: Vortex convection and acoustic wave propagation in the cavity at two different times $t = 0$ and $t = t'$.

model is the one proposed by Rossiter [110] which is the basis of many more sophisticated models.

Rossiter model:

Rossiter [110] was the first to propose a model to estimate the frequency of the self-sustained oscillations. The observation that the peaks in the pressure spectra are not related harmonically, gave the motivation for this model. A relation for the frequencies can be found by considering separately the two components of the feedback mechanism at two different time instants $t = 0$ and $t = t'$.

Figure 3.2 shows the vortex convected with the speed κU_0 in the shear layer and the acoustic wave traveling in upstream direction with the speed of sound c_a in the cavity. At instant $t = 0$, a pressure wave is emitted when the vortex impacts on the downstream edge. Introducing arbitrarily a time lag between the impact of the vortex and the emission of sound, the vortex has thus been convected over a distance of $\gamma_v \lambda_v$ from the cavity leading edge. At instant $t = 0$, the length between the pressure wave that is located nearest to the upstream angle and the downstream angle contains m_a acoustic wave lengths λ_a. At instant $t = t'$, this pressure wave has reached the upstream angle and triggers the development of a new vortex. The length between the new vortex triggered at the leading edge and the vortex that has been emitted the acoustic wave at $t = 0$ is $m_v \lambda_v$, where λ_v is the distance between two vortices.

Two relations can be found in order to determine the characteristic wavelengths of the vortex

convection and the acoustic wave propagation:

$$m_v\lambda_v = L + \gamma_v\lambda_v + \kappa U_0 t'$$

and

$$L = m_a\lambda_a + c_a t'.$$

Eliminating t', leads to

$$\frac{m_v\lambda_v - L - \gamma_v\lambda_v}{\kappa U_0} = \frac{L - m_a\lambda_a}{c_0}.$$

Defining a characteristic frequency for the vortical mode and the acoustic mode $f = \kappa U_0/\lambda_v = c_a/\lambda_a$ gives

$$f = \frac{U_0}{L}\frac{m_v + m_a - \gamma_v}{M_0\frac{c_0}{c_a} + \frac{1}{\kappa}}.$$

For subsonic cavities, the sound celerity in the cavity and in the free-stream are nearly the same ($c_0 = c_a$). Defining a mode number such as $n_R = m_a + m_v$, gives the Rossiter's formula:

$$f = \frac{U_0}{L}\frac{n - \gamma_v}{M_0 + \frac{1}{\kappa}} \tag{3.1}$$

The Rossiter's formula is a very efficient way to estimate the resonance frequencies of cavities in subsonic and transonic regime. The formula contains two parameters κ and γ_v; $\kappa \equiv U_c/U_0$ represents the dimensionless convection velocity and γ_v is the time lag between the impact of the vortex and the emission of an acoustic wave, a parameter that is difficult to access experimentally.

The fact that the feedback cycle is closed with an upstream traveling acoustic wave is not valid for incompressible and low Mach number flows where the feedback is rather based on a pure hydrodynamic phenomenon. Experiences have shown that for the present cavity flow at $M \approx 0.2$, the Rossiter's model is well adapted to predict the peak frequencies. A short overview over some extensions of the Rossiter's model are given in the following.

Classical Extension:

More sophisticated models have been proposed in the literature for the supersonic and subsonic regime. Block [22] includes the effects of the cavity depth L/D as a model parameter and proposes a value for λ_v. The frequencies can be estimated by the formula

$$f_n = \frac{U_0}{L}\frac{n}{M(1 + \frac{0.514}{L/D}) + \frac{1}{\kappa}}$$

Tam and Block [126] propose to include the analytical developments of a finite shear layer in order to take into account the excitation mechanism at the separation point. The model works well for low Mach number regimes from $0.2 < M < 0.4$.

The model of Sahoria [112] takes into account the theory of instabilities of a thickening mixing layer and derives a criteria to determine the dominant mode. Rockwell [107] refines the model in order to predict the resonance frequencies based on the characteristics of the mixing layer.

Numerical Simulations

Many numerical studies have been carried out since the first simulation in 1977 of Borland [32] based on the resolution of the 2-D Euler equations. Further simulations including turbulent effects using Reynolds Averaged Navier-Stokes equations in 2-D [145] and 3-D [104] followed. Sinha [118] notices that the use of averaged equations lead to an underprediction of the sound pressure levels due to an overestimation of the turbulent viscosity that damps pressure oscillations.

This observation initiated the use of Large Eddy Simulation for cavity flows. The first Very Large Eddy Simulation (VLES) has been made by Sinha [118]. Other computations followed using zonal hybrid methods that combine RANS methods to model the incoming boundary layer and LES methods for the shear layer zone [8].

A further way to simulate cavity flow is the Direct Numerical Simulation (DNS) of the Navier-Stokes equations. Being very demanding in computation power and storage, DNS is limited to small Reynolds number flow and have been simulated in most of the cases in 2-D [39, 62] and more recently in 3-D by Brès and Colonius [33]. Cavity flow simulations have also been carried out using the Lattice Boltzmann method [103] for subsonic flows for the purpose of automotive applications. Another numerical example is the use of 2-D Euler equations for the computation of the flow over deep cavities [44].

Larchevêque *et al.* [85, 84] demonstrates that LES is a very promising way to recover the physics of cavity flow at higher Reynolds numbers. Several computations of cavities flows with different aspect ratios L/D have been computed and reproduce the experimental results of Forestier [53] in an impressive way. In the same way, LES can reproduce the passive control of cavity flow using a spanwise rod such as demonstrated by Daude [42].

The confined and partially covered cavity considered here has already been studied in 2-D by using a second-order TVD-Euler code [81, 83]. Rossiter frequencies have been recovered, but turbulent aspects could not be considered due to the inviscid 2-D simulation. Gloerfelt [61] computed the flow using 2-D Navier-Stokes equations. He also could recover the frequencies and demonstrated the evidence of the aeroacoustic coupling between cavity and duct modes. Discrepancies in amplitude have been explained by artefacts due to the resolution of 2-D Navier-Stokes equations for this high-Reynolds number application.

3.2 Experimental observations

In the following, the results of experiments are recalled. The experimental data have been provided by the Institut Aérotechnique [81, 5] for the partially covered and ducted cavity, shown in Figure 3.1.

3.2.1 Influence of the upper wall

For unconfined cavities, the self-sustained oscillations remain weak for flows at low Mach numbers. For ducted cavities, the possible coupling between Rossiter Modes (RM) and acoustic Duct Modes (DM)

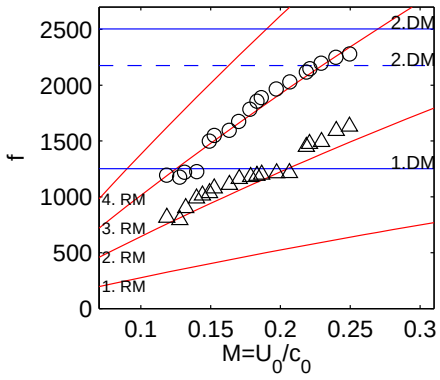

Figure 3.3: Frequency of dominant pressure spectra peaks (△, ○) measured inside the cavity compared to theoretical ones as a function of the Mach number U_0/c_0: —— theoretical Rossiter mode for $n_R = 1, 2, 3, 4$; —— acoustic transverse duct modes $n_D = 1, 2$ based on duct height H ; - - - - acoustic transverse duct modes $n_D = 2$ based on duct height and cavity height $H + h$.

can lead to high amplitude oscillations even at low speeds.

Pressure signals have been measured by using a microphone located at the bottom center of the cavity [81, 5]. The measured spectra exhibit peaks that can be associated with cavity modes. Plots of frequency and pressure level of these peaks as functions of the nominal Mach number $M_0 = U_0/c_0$ where c_0 denotes the sound velocity at reference conditions ($p_0 = 1.0 \times 10^5$ Pa and $\rho_0 = 1.2$ kg.m^{-3}), are shown in Figure 3.3 and 3.4 respectively.

The theoretical cavity modes can be estimated by Rossiter's formula given by equation (3.1), where $\gamma_v = 0.25$, $U_0/U_c = \kappa = 0.57$. They are plotted in Figure 3.3 for $n_R = 1,\ 2,\ 3,\ 4$. The transverse DM are given by

$$St_d = f_d \frac{d}{U_0} = \frac{n_D c}{2H_d} \frac{d}{U_0},$$

where n_D is the DM number and H_d the height of the wave guide. The DM frequencies are plotted in Figure 3.3 for $n_D = 1,\ 2$ and for the duct height, $H_d = H$. Additionally, the frequency of the second tranverse DM based on the sum of the duct height and the cavity height, $H_d = h + H$, is plotted in Figure 3.3.

The lock-in phenomenon can be observed when the frequencies of the cavity modes stops to scale with the theoretical RM evolution and continues to scale with the DM frequency. When lock-in occurs, the amplification of the pressure oscillations is maximum. This can be always observed when the RM approaches the DM. At $M_0 = 0.13$, the third RM locks with the first DM and at $M_0 = 0.18$, the second RM locks with the first DM. At $M_0 = 0.23$, the third RM locks with the second DM. In this case, the measured frequencies collapse with the frequencies of the second DM, based on the sum of the cavity and the duct heights.

3.2.2 Influence of the cover plates

The influence of the neck has been studied experimentally by the Institut Aérotechnique [4]. By filling the cavity under the edges with material, a noise reduction of 20 dB has been observed.

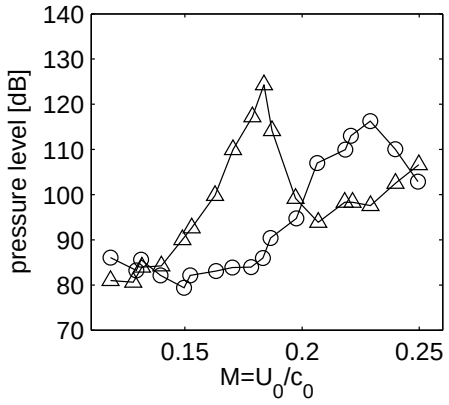

Figure 3.4: Level of pressure oscillations of dominant pressure spectra peaks (△, ○) measured inside the cavity as functions of the Mach number .

	N_x	N_y	N_z	N_{procs}
Duct	542	149	41	39
Neck	126	39	41	3
Cavity	180	61	41	5

Table 3.1: Grid statistics for the ducted cavity. The case has been computed by $N_{\text{procs}} = 47$ processors. The total number of grid points is 4×10^6. The neck is the region located between the cover plates.

A numerical study of a open cavity with cover plates has been carried out by Heo and Lee [67] and Gloerfelt [61]. They observed a change in directivity. The non-covered cavity emits noise in upstream direction. The covered cavity tends to emit less directive noise but with higher amplitudes.

The directivity is due to the destructive interference of noise emitted by the cavity directly when the vortex impacts at the downstream angle and the noise reflected at the cavity walls. For the covered cavity, the acoustic waves remain confined in the cavity and noise reduction via destructive interference does not occur. This is probably amplified by the resonance mechanism observed in the present configuration and explains the significant noise production of 20 dB. In the present work, only the cavity with cover plates is considered.

3.3 Simulation parameters

The entire overset grid generated by *ogen* is displayed in Figure 3.5. It consists of seven component grids. As the grid points of the communication interfaces coincide, no interpolation has to be used. The grid spacing is kept constant inside the cavity ($\Delta x = 4 \times 10^{-4}$ m and $\Delta y = 2 \times 10^{-4}$ m) and in the boundary layer ($\Delta y = 2 \times 10^{-4}$ m). In the duct, the grid is stretched in the y-direction near the upper wall with 3.0%. Upstream and downstream of the cavity, the grid is stretched in the x-direction with 1.0%.

The Reynolds number based on the duct height H and the velocity $U_0 = M_0 c_0$ is $Re_H \approx 5.6 \times 10^5$. The crucial point in cavity simulations is the boundary layer upstream the cavity, whose shape controls

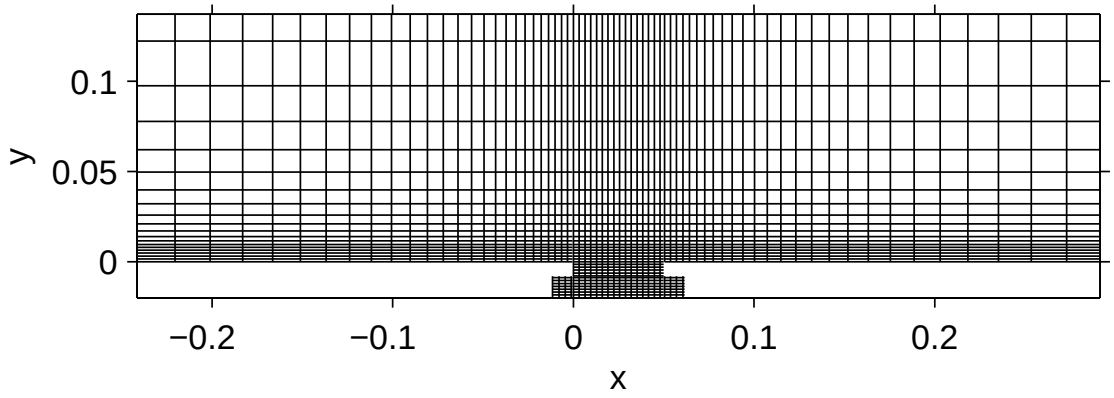

Figure 3.5: Overset grid generated by *ogen*. Every tenth line is represented.

the vortex shedding and the convection of the eddies in the shear layer. The boundary layer profile that has been measured experimentally is fitted by a $1/n$ profile (Schlichting [113]) :

$$\frac{u_(y)}{U_0} = \begin{cases} \left(\frac{y}{\delta}\right)^{\frac{1}{n}}, & y \leq \delta \\ 1, & y > \delta \end{cases}$$

where $\delta = 8.8$ mm and $n = 8.5$. For the power law the momentum thickness of the boundary layer computes such as:

$$\delta_\theta = \frac{n}{(n+1)(2+n)}\delta = 0.75 \text{ mm}.$$

The displacement thickness δ^* of the boundary layer is given for the power law by:

$$\delta^* = \frac{1}{1+n}\delta = 0.92 \text{ mm}.$$

The form factor gives $H = \delta^*/\delta_\theta = 1.24$ mm.

The friction velocity can be estimated by the universal law of friction that is given by equation (20.30) of reference [113]:

$$\frac{1}{\lambda} = 2\log\left(\frac{U_d\ d_H}{\nu}\sqrt{\lambda}\right) - 0.8,$$

where $\lambda = 8(u_f/U_d)^2$, $U_d = 52.5$ m s^{-1} [4] is the flux velocity and d_H is the hydraulic diameter. The latter is given by $d_H = 2WH/(W+H) = 0.148$ m. This equation has to be solved by a Newton solver and gives $\lambda = 0.013$. Finally, the friction velocity gives $u_f = 2.1$ m s^{-1}. The Reynolds number based on δ^* and $U_0 = 0.18c_0$ is thus $Re_{\delta^*} = 3771$. The grid size in wall units normal to the wall is computed $\Delta y^+ = \Delta y u_f/\mu = 28$. In order to avoid excessive filtering of the inflow velocity profile, only the fluctuating quantities are filtered. Upstream the cavity, the initial mean flow field is preserved during the whole simulation run.

The inflow velocity profile, density and the pressure are imposed in a weak manner to prevent possible numerical drift due to numerical diffusion and truncation effects of the inflow. As the flow Mach number lies in the low subsonic domain, the mean density and the mean pressure are taken constant over the whole height of the inflow and outflow ($p_{in} = p_{out} = p_0, \rho_{in} = \rho_{out} = \rho_0$). During the simulation, the inflow mean quantities are recalled along the inlet boundary condition with the

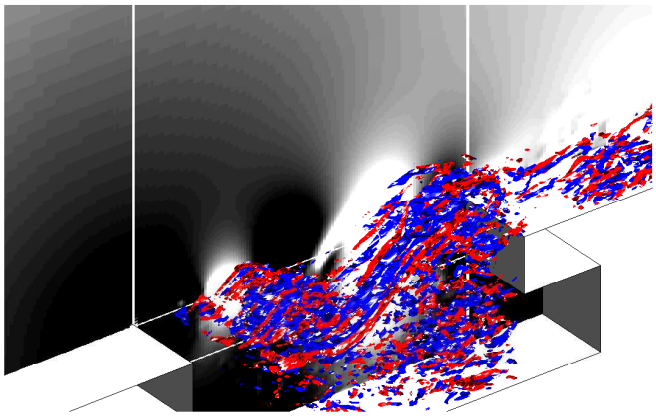

Figure 3.6: Computed instantaneous vorticity modulus field ($\omega_x = 25 \times 10^3$ s^{-1}, $\omega_x = -25 \times 10^3$ s^{-1}) for $M_0 = 0.18$; the instantaneous pressure field is shown in the background; gray scales $-100 < p - p_0 < 100$ Pa.

relaxation term of equation (1.16). In a similar way, the pressure and the density at the outflow are recalled. A sponge zone combining grid stretching and a Laplacian filter at the outflow are used to avoid reflections.

As the influence of the boundary layer on the upper duct wall can be neglected, slip conditions are applied. Otherwise no-slip adiabatic conditions have been implemented along the wall boundaries. In the spanwise direction, periodic conditions are applied.

The time step is $\Delta t = 4.5 \times 10^{-7}$ s. A number of 500000 iterations have to be run in order to pass the transition phase and obtain sufficiently long time signals for an accurate frequency domain analysis.

3.4 Results

First the results of the configuration with $M_0 = 0.13$, $M_0 = 0.18$ and $M_0 = 0.23$ are presented. The aerodynamic field of the computation with $M_0 = 0.18$ is considered in more detail. Then the results of a series of computation with different Mach numbers M_0 are presented in order to demonstrate the numerical evidence of the coupling mechanism between the RM and DM.

3.4.1 Aerodynamic field for $M_0 = 0.18$

Figure 3.6 shows the iso-surface of a snapshot of the vorticity modulus inside the cavity obtained for $M_0 = 0.18$. The incoming unperturbed boundary layer breaks down and generates coherent structures. Two coherent structures convected in the shear layer can be observed and indicate the dominance of the second Rossiter's mode. Secondary longitudinal vortex rolls can be observed.

A plot of the streamlines is given in Figure 3.7. Two main circulation zones can be observed. Two additional circulation zones can be found under the cover plates.

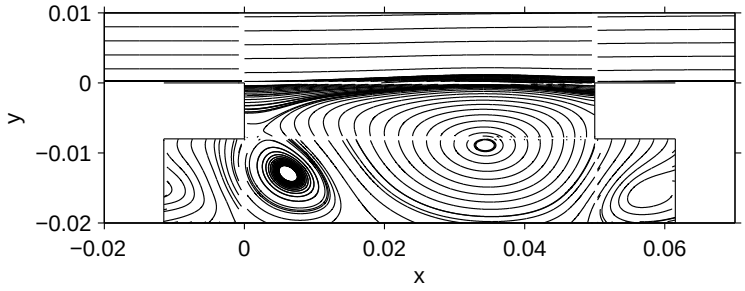

Figure 3.7: Computed streamlines for the Mach number $M_0 = 0.18$.

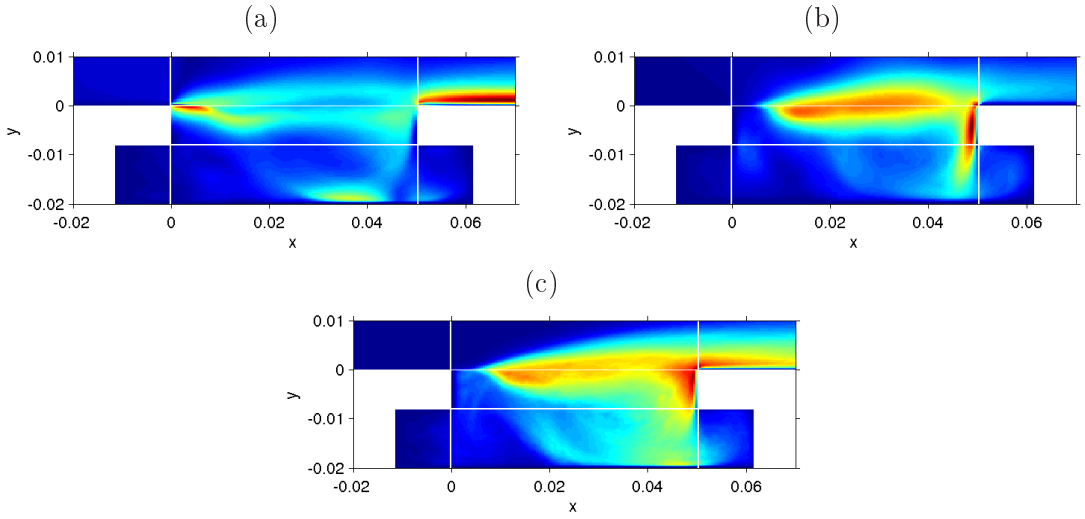

Figure 3.8: Dimensionless turbulent fluctuations: (a) u_{rms} color scales between 0 and 0.11; (b) v_{rms} color scales between 0 and 0.08 ; (c) w_{rms} color scales between 0 and 0.04.

The turbulent fluctuations of u_{rms}, v_{rms} and w_{rms} are given by

$$u_{\text{rms}} = \frac{\sqrt{u^2}}{U_0}, \; v_{\text{rms}} = \frac{\sqrt{v^2}}{U_0} \text{ and } w_{\text{rms}} = \frac{\sqrt{w^2}}{U_0}$$

and are plotted in Figure 3.8 (a), (b) and (c). The u_{rms} field features a double peak typical for excited shear layers [97] or for cavities with high values of L/δ_θ [53]. The origin of the double peak has been explained by Ziada and Rockwell [146] by the presence of Stuart vortices. The maximum value of u_{rms} and v_{rms} reaches a maximum value of 0.11 and 0.08 respectively. Those values are lower than the values of a mixing layer that are typically $0.16 < u_{\text{rms}} < 0.18$ and $0.12 < v_{\text{rms}} < 0.14$ [60].

The values of v_{rms} reach a saturation state. The two peaks merges near the downstream angle of the cavity. The fluctuations v_{rms} show a maximum at the downstream vertical wall indicating the presence of a plane jet in vertical direction. At the position where the jet reattaches, a maximum in u_{rms} can be observed. The jet is formed due to the impact of the coherent structures on the downstream angle and induces the recirculation zone in the cavity.

1-D frequency spectra of the velocity components and pressure are given at the location $(x, y, z) = (2h, 0, 0)$ in Figure 3.9. A dominant frequency in the spectra of pressure signal and of streamwise

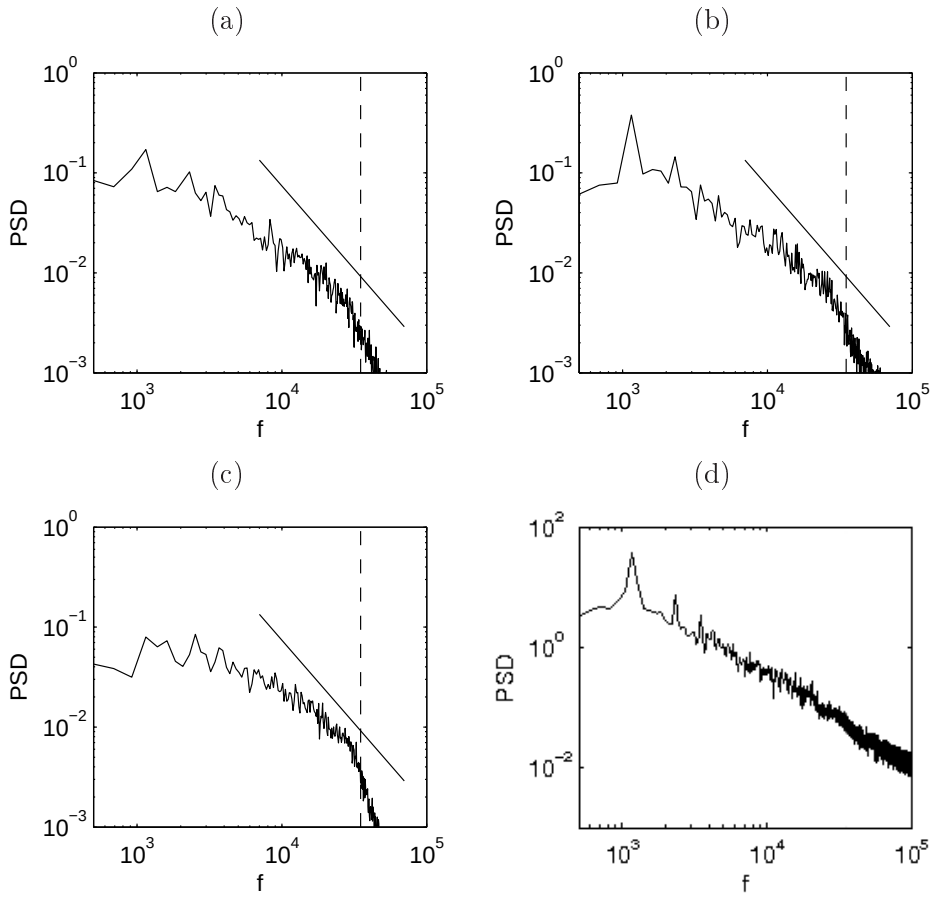

Figure 3.9: 1-D spectra of (a) u-velocity component [m.s^{-1}] ; (b) v-velocity component [m.s^{-1}]; (c) w-velocity component [m.s^{-1}]; (d) p-velocity component [Pa].- - - - designates the cut-off frequency.

velocity component signal can be observed at around 1200 Hz corresponding to the resonance frequency of the cavity. The cut-off frequency of the selective filter is found behind the beginning of the energy cascade. This indicates that the largest structures of the cavity flow are captured. No accumulation of energy can be observed in the high frequency domain of the simulation so that the energy of not well-resolved scales are removed properly by the selective filter.

The pressure spectrum obtained for a signal recorded at the cavity bottom is compared with the measured pressure spectrum in Figure 3.10. The computed spectrum is globally overestimated of about 10 dB. For cavity flow simulations this discrepancy is non typical since in general the pressure levels are not recovered due to excessive damping of the numerical algorithm. Preliminary 2-D computations have also given overestimations of broad-band noise [81, 61]. This might be an indication that a wrong scaling of the sound pressure levels has been affected on either the side of the experimental results or of the present simulation. Cavity flow measurement are very sensitive. Even small geometrical irregularities can influence its resonance properties and lead to large changes in sound pressure level. Furthermore the dynamic gap between the peak frequency and the broad-band noise, found in the experiences is surprisingly large.

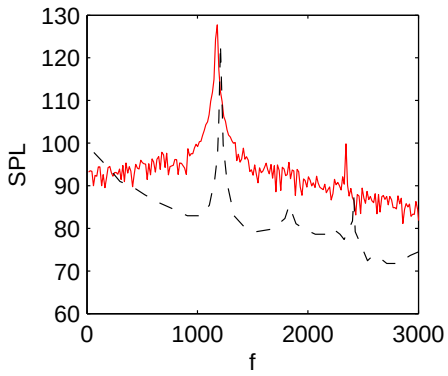

Figure 3.10: Sound pressure level [dB] measured at the bottom of the cavity: —— computation; - - - - experiments.

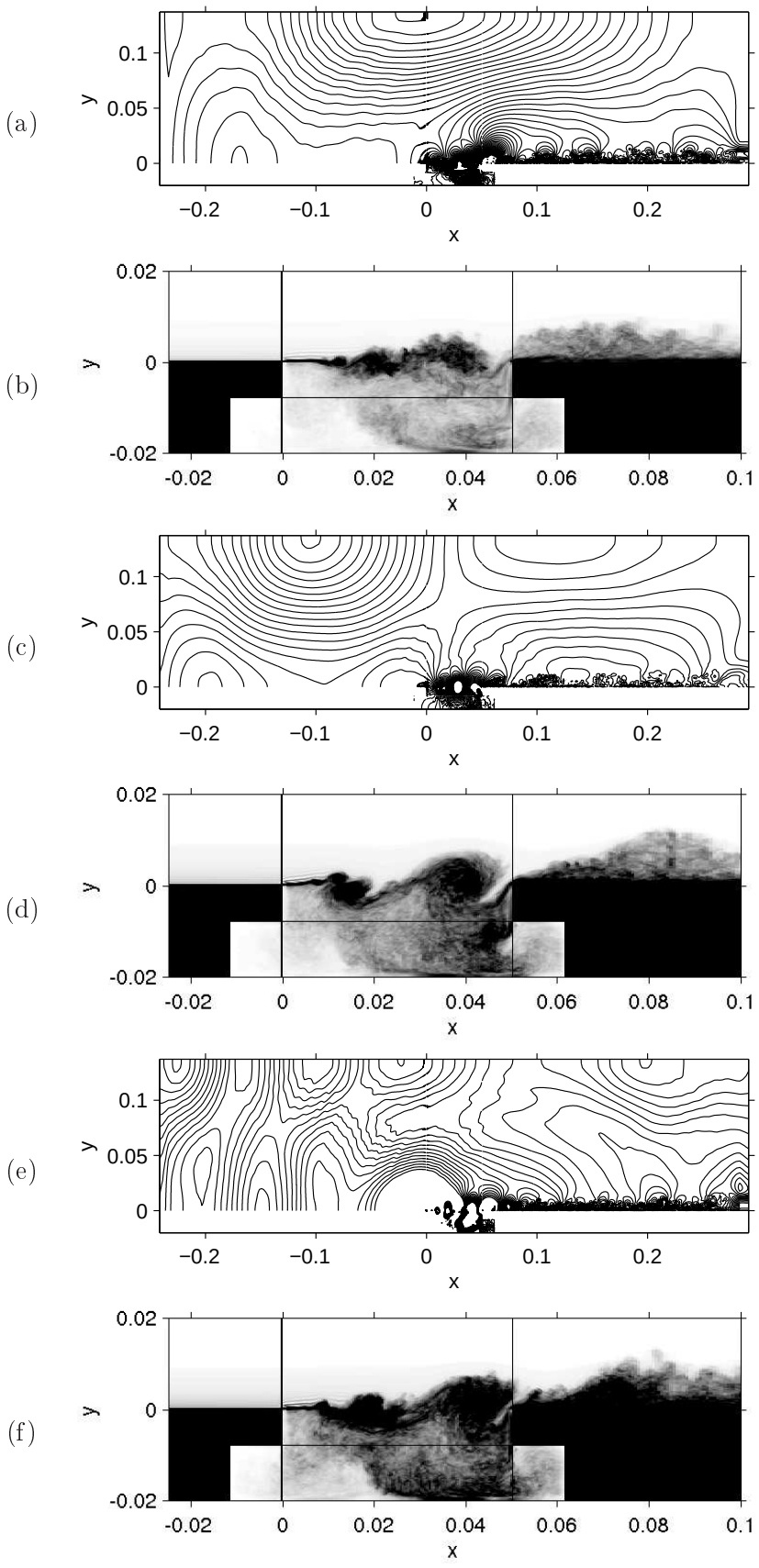

Figure 3.11: Computed instantaneous pressure field (contours $|p-p_0| < 100$ Pa) and spanwise averaged vorticity modulus in the cavity for different Mach: (a) (b) $M_0 = 0.13$, (c) (d) $M_0 = 0.18$, (e) (f) $M_0 = 0.23$.

3.4.2 Acoustic data for $M_0 = 0.13$, $M_0 = 0.18$ and $M_0 = 0.23$

The acoustic fields of three selected computations with Mach numbers $M_0 = 0.13$, $M_0 = 0.18$ and $M_0 = 0.23$ are examined in the following. For those Mach numbers, maximum amplification of pressure oscillations due to coupling between RM and transverse DM have been observed experimentally.

An instantaneous plot of the pressure fluctuation field and the associated vorticity field for the three different Mach numbers are given in Figure 3.11 (a), (c) and (e). The presence of the first transverse DM that propagates in upstream and downstream direction can be observed for $M_0 = 0.13$ and $M_0 = 0.18$. For the $M_0 = 0.23$ case, higher transverse DMs superposed to the first transverse DM are observed.

The pressure signals for the three Mach numbers have been recorded in the bottom of the cavity and on the upper wall at $x = L/2$ and are given in Figure 3.12. For $M_0 = 0.18$ and $M_0 = 0.23$, the numerical solution converged fast. For $t > 0.02$ s, after only 4×10^4 iterations, regular oscillations can be observed in the duct and in the cavity. The $M_0 = 0.13$ case converges after 4×10^5 iterations ($t = 0.2$ s). For all computations, the pressure fluctuations are regular and the amplitude at the upper wall are lower than in the cavity due to the absence of hydrodynamic pressure fluctuations. For time signals obtained with $M_0 = 0.23$, low-frequency modulations can be observed.

The spectra of the signals at the cavity bottom and the upper wall computed with $M_0 = 0.18$ are compared in Figure 3.13. The amplitude difference of the two spectra is about 5 dB in the peaks and can be up to 12 dB in the broad-band noise range. The experience measured a difference of 15 dB between the peaks of the two signals.

The cross power spectral density of the two signals obtained for the three Mach numbers have been computed. Its phase and coherence are given in Figure 3.14 (a), (b) and (c) respectively. For $M_0 = 0.13$ the two signals are correlated with a phase shift of π at the frequency of the first transverse DM. This confirms the observation made for the instantaneous pressure field. For $M_0 = 0.18$ the first DM is also dominant as expected. For the flow at $M_0 = 0.23$, maximum coherence can be observed at three frequencies corresponding to the first and to second DM and to the frequency of the second RM. The first DM is shifted by π and the second DM is not shifted in phase confirming the presence of the first and second transverse duct modes respectively. As already observed in the snapshot of the pressure fluctuations field for $M_0 = 0.23$, the first and second transverse DMs are present in the duct.

3.4.3 Amplification of the cavity modes

In order to demonstrate the numerical evidence of the coupling between the RMs and DMs, further calculations have been carried out for several nominal Mach numbers M_0: 0.13, 0.16, 0.18, 0.20, 0.21, 0.23 and 0.25.

The numerical spectra obtained from signals recorded at the bottom center of the cavity (as for the experiments) provides the frequency and the amplitude of the peaks associated with the second and third cavity modes. Figure 3.15 compares the evolution of the computed and measured frequencies of the modes. The frequency of the different modes are well retrieved. At $M_0 = 0.13$, lock-in between

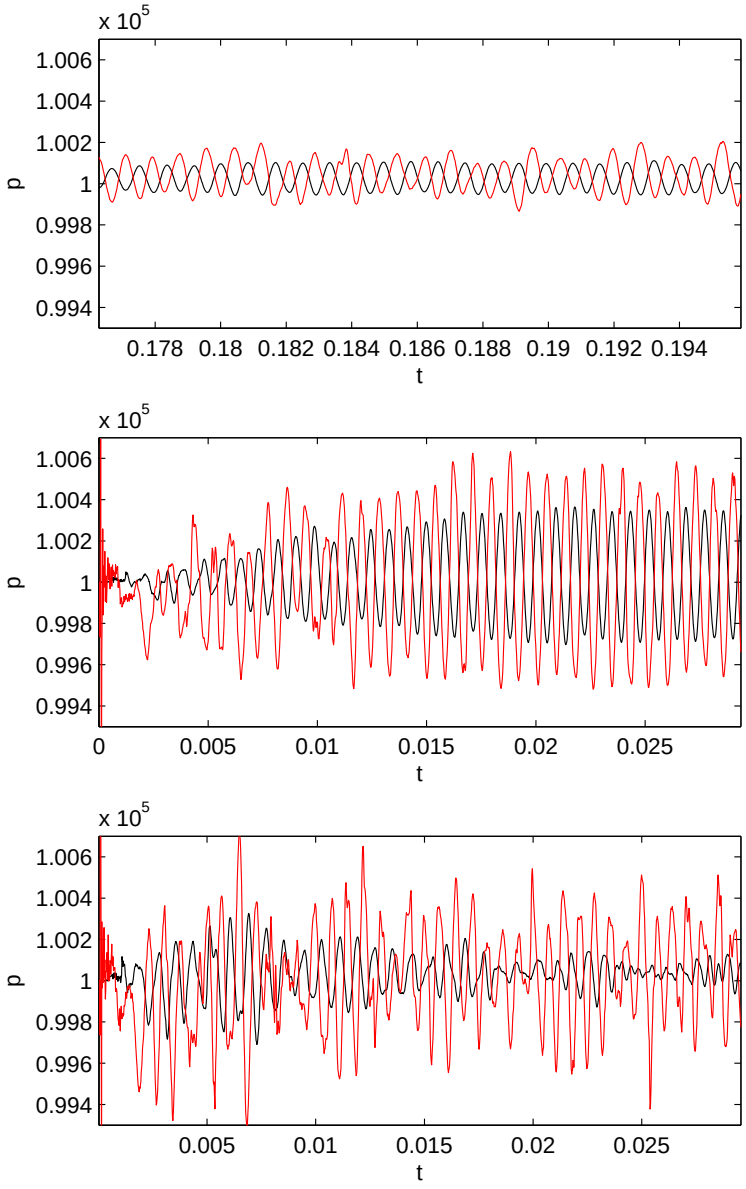

Figure 3.12: Pressure signals [Pa] recorded at $x = L/2$ and $z = 0$: —— on the cavity bottom; —— on the upper wall for different Mach numbers: (a) $M_0 = 0.13$ (b) $M_0 = 0.18$ and (c) $M_0 = 0.23$.

the third RM and the first DM, at $M_0 = 0.20$, lock-in between the second RM and the first DM and at $M_0 = 0.23$, lock-in between the third RM and the second DM occurs. In agreement with the experiments in the latter case, it is observed that the lock-in phenomenon occurs rather with the second DM mode based on the sum of the duct and cavity height. The frequency of third Rossiter mode computed for $M_0 = 0.16$, 0.18 and 0.20 is invariant. The origin of this numerical artefact is under consideration.

Figure 3.16 shows the evolution of the computed and measured amplitudes of the cavity modes. The comparison is qualitatively good. The second RM remains too high after lock-in having occurred at $M_0 = 0.20$. The amplitude of the third RM is overpredicted for low Mach numbers and underpredicted for higher Mach numbers. As a consequence, the crossing of the amplitude curves of the second RM

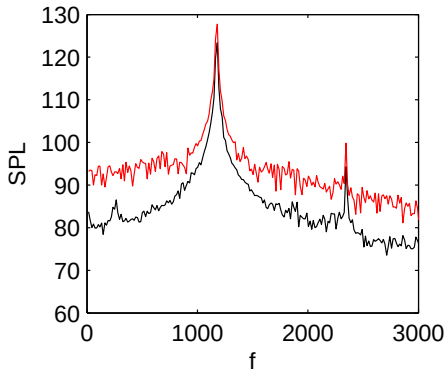

Figure 3.13: Sound pressure level [dB] measured at the bottom and —— at the upper wall ——.

and third RM at $M_0 = 0.2$ is not reproduced and no dominance of the third RM can be detected at higher Mach number such as $M_0 = 0.23$.

Figure 3.11 (b), (d) and (f) show snapshots of the instantaneous vorticity field in the cavity for three different Mach numbers $M_0 = 0.13$, $M_0 = 0.18$ and $M_0 = 0.23$ respectively. At $M_0 = 0.18$, two eddies appear very distinctly in the shear layer. This confirms the second RM to be dominant. In Figures 3.11 (b) and (f), no dominant third RM can be detected, because for these two Mach numbers, the second RM and third RM have similar amplitudes.

3.5 Influence of the simulation parameters

Preliminary 2-D computations [61] using a similar grid resolution have overestimated the broad-band noise as well as the second RM at $M_0 = 0.23$. The similar behavior found for the present 3-D computation with periodic conditions in spanwise direction suggests that 2-D artefacts might be the cause of the discrepancies. The number of points in spanwise direction have therefore been tripled ($N_z = 121$). The results of this computation did not influence the broad band noise as well as the peak levels and the third RM has not become dominant.

Therefore a second grid has been generated. In this case the grid size length have been halved in the cavity region which is a very easy task using the overset grid approach. The computation at $M_0 = 0.23$ is currently running. Figure 3.17 shows a snapshot of the vorticity modulus, reveal the dominance of a third RM.

3.6 Conclusion

Quantitative discrepancies, in particular the absence of a dominant third cavity mode at high Mach numbers and the overestimation of the broad band-noise, are currently under examination. The use of a finer grid shows very promising results and makes the third RM to emerge. The examination of the influence of a realistic turbulent boundary layer as the inflow condition should be considered in the future. However, the present numerical study shows the capability of the numerical algorithm to

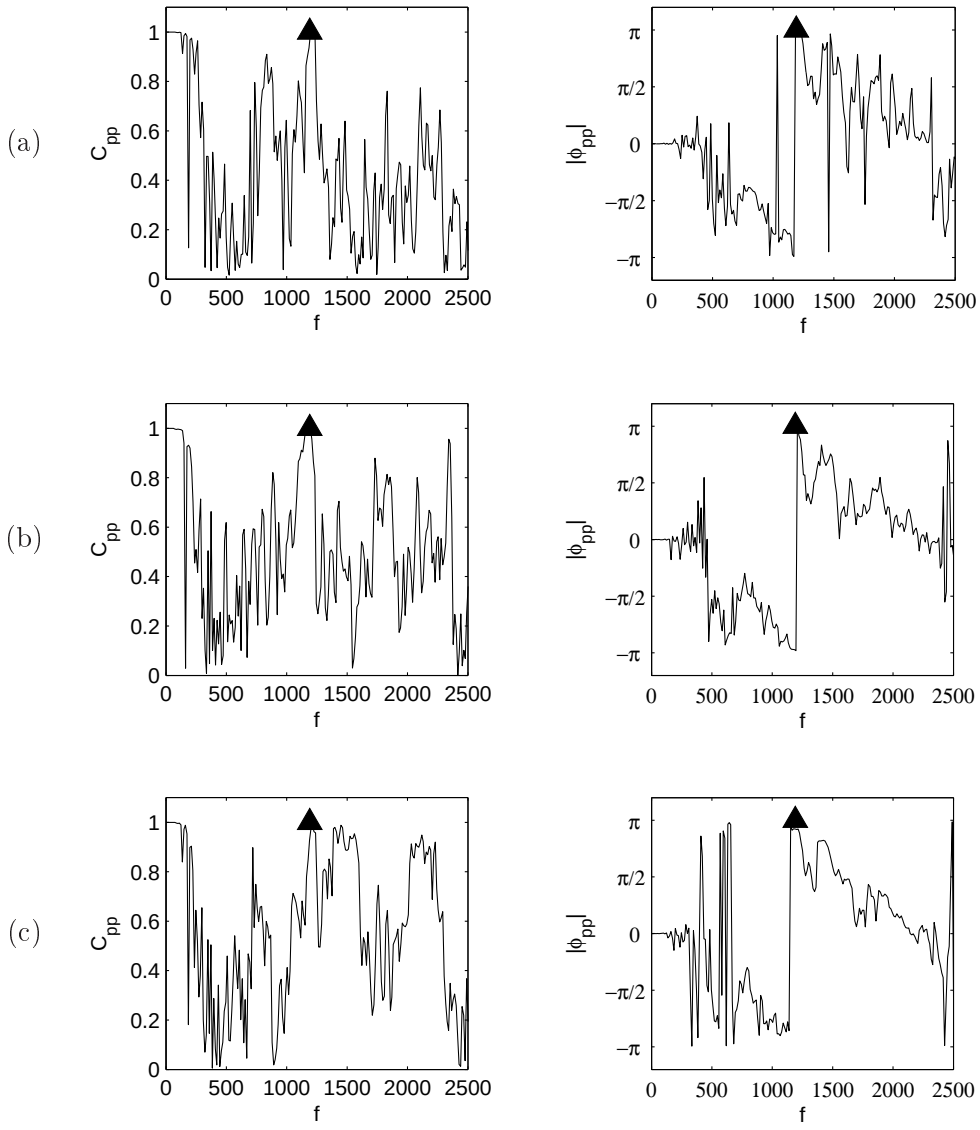

Figure 3.14: Phase Φ_{pp} and coherence C_{pp} of the cross power spectral density of signals recorded at the bottom of the cavity and the upper duct wall for different Mach numbers: (a) $M_0 = 0.13$, (b) $M_0 = 0.18$ and (c) $M_0 = 0.23$; ▲ designates the second Rossiter mode.

reproduce the coupling phenomenon between the cavity modes and the duct modes with affordable computational resources. In particular, frequencies are well retrieved by the computation.

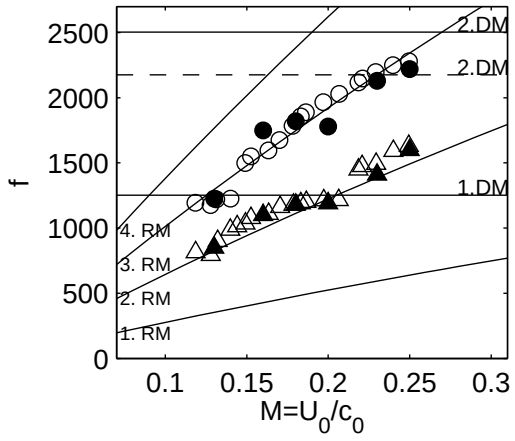

Figure 3.15: Computed frequencies (▲ mode 2, • mode 3) of the cavity modes compared to experimental ones (△ mode 2, ∘ mode 3) and to Rossiter and duct mode frequencies (RM = Rossiter mode, DM = duct modes). The modified second DM (- - - -) is calculated with the sum of the duct and the cavity heights $h + H$.

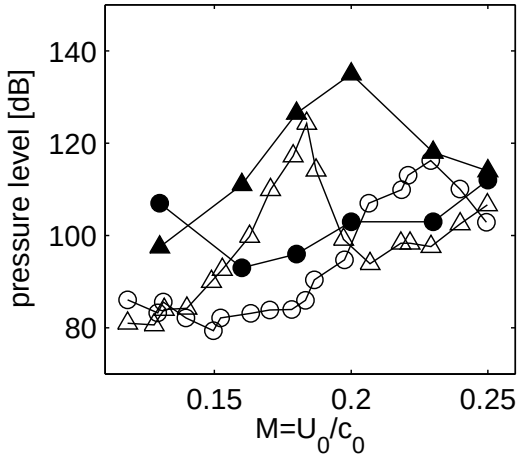

Figure 3.16: Computed power levels (▲ mode 2, • mode 3) of the cavity modes compared to experimental ones (△ mode 2, ∘, mode 3).

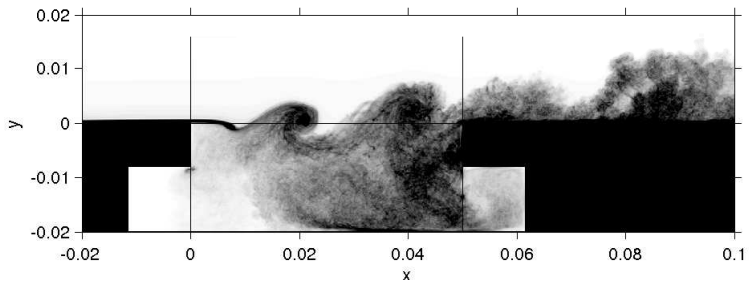

Figure 3.17: Spanwise averaged vorticity modulus in the cavity obtained for $M_0 = 0.23$ on a fine grid.

Chapter 4

Aeroacoustic simulation of the sudden expansion of a transonic flow

4.1 Introduction

Strong interactions between shock oscillations, internal aerodynamic noise and acoustic duct modes are often observed in confined flows but are undesirable to prevent excitation of structural vibrations and fatigue. Numerous examples can be found in the review of Meier *et al.* [95].

In the present work, a transonic flow passing a sudden expansion in a duct is studied. This kind of flow can be found downstream of control devices such as valves encountered in pipe systems of power plants, and has been investigated experimentally by Meier *et al.* [94, 6]. These authors studied a transonic flow in a rectangular duct such as displayed in Figure 4.1. Air at atmospheric conditions (denoted by subscript a) passes through a convergent nozzle. The flow in the nozzle throat is expanded abruptly by passing in the expansion duct of larger cross-section. The flow is driven by the exit pressure p_e in the reservoir downstream of the expansion duct. Different transonic and supersonic flow regimes have been investigated as a function of the pressure ratio defined by $\tau = p_e/p_a$.

For very low pressure ratios, the flow in the upstream part of the test duct is entirely supersonic. The flow regime for $\tau = 0.15$ is visualized by means of Mach-Zehnder Interferometry [94] in Figure 4.2 (a). A system of crossing oblique shock waves is observed. Increasing the exit pressure leads to a flow separation and to a breakdown of the shock cell structure. Shock pattern oscillations are then observed. In this work, this flow regime has not been considered. Details can be found in the work of Meier *et al.* [94].

If the downstream pressure is further increased, the oblique shock wave system disappears and the supersonic expansion ends up behind a single normal shock such as presented in Figure 4.2 (b) for $\tau = 0.364$. In this case, a strong coupling between the self sustained oscillations of the normal shock and the longitudinal acoustic modes of the duct is found. The observed oscillation frequencies are low, typically f $\sim 10^2$ Hz.

For lower pressure ratios, the flow regime is symmetrical. For higher pressure, ratios $\tau = 0.377$

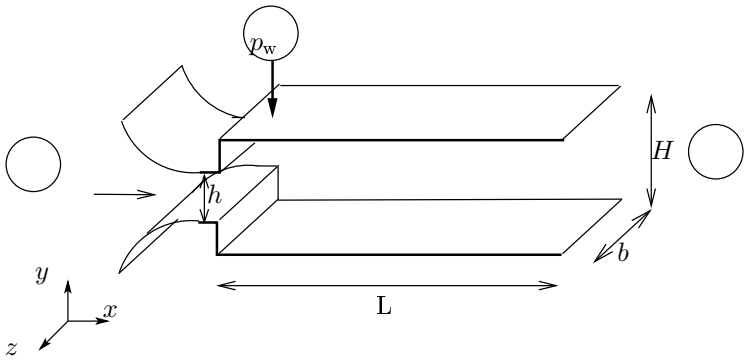

Figure 4.1: Transonic flow passing sudden expansion: sketch of the geometry and notations: H and L are the height and the length of the expansion duct respectively, h designates the height of the inflow nozzle and $b = 0.1$m is the width of the nozzle and the expansion duct in spanwise direction; p_a and T_a are the pressure and temperature of air at ambient conditions; p_e is the pressure in the downstream reservoir imposed by the pressure ratio $\tau = p_e/p_a$. p_w is the pressure in the corner region.

for instance, asymmetric flow pattern occurs and one side is entirely separated from the wall such as shown in Figure 4.2 (c). For those flows, having a more jet like structure, a coupling mechanism similar to the normal shock configuration, is only observed for longer ducts.

The flow regime depends also whether the pressure ratio is increasing or decreasing. For increasing pressure ratios, the symmetrical oscillating flow pattern is maintained even for pressure ratios where asymmetrical non-oscillating flow regimes are observed when the pressure ratio is decreasing. This hysteresis needs to be accurately captured by the simulations to reproduce the coupling between the shock oscillations and the longitudinal duct modes.

Meier *et al.* [94] provide time sequence visualizations of the different flow regimes based on Mach-Zehnder Interferometry. Static wall pressure data, frequency spectra and cross correlations of the pressure fluctuations along the walls are also available, making possible a quantitative validation of the numerical results.

This flow configuration involving turbulence, shocks, interaction with boundary layers and aeroacoustic resonances is a real challenge for computational aeroacoustics [123]. Devos and Lafon [82] studied numerically this configuration using a second-order TVD finite-volume scheme for solving 2-D Euler equations. The main flow patterns were captured but the coupling of the shock oscillations with the resonance modes of the duct was not considered.

The chapter is organized as follows. In section 4.2, the supersonic flow at a low pressure ratio is presented. In section 4.3, four simulations are presented for pressure ratios involving a normal shock flow pattern in order to demonstrate the influence of the pressure ratio on the flow field. In section 4.4 a simulation is presented where the shock oscillations couple with longitudinal duct modes.

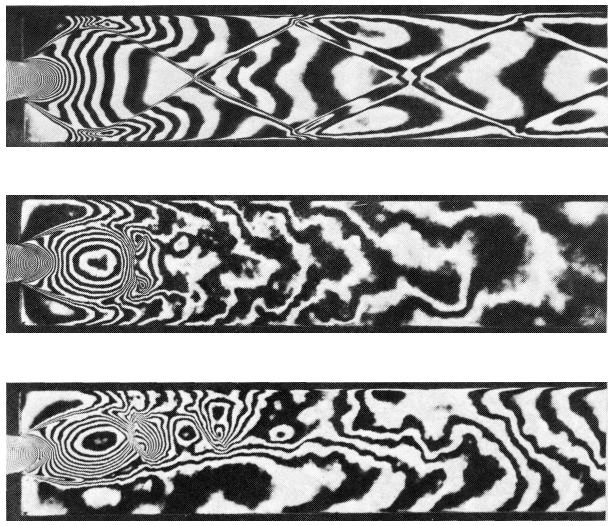

Figure 4.2: Mach-Zehnder interferometry visualizations at pressure ratios: (a) $\tau = 0.151$ (b) $\tau = 0.364$ and (c) $\tau = 0.377$ for a expansion duct length L = 0.24 m and aspect ratios L/H = 7.23 and h/H = 0.3.[94]

4.2 Supersonic flow at low pressure ratio ($\tau = 0.15$)

4.2.1 Simulation parameters

The entire overset grid generated by *ogen* is represented in Figure 4.3 (a). It consists of three parts: the nozzle, the expansion duct and the reservoir. Note that the convergent part of the nozzle is not modeled in this work. The inflow conditions are determined assuming the flow to be isentropic in the convergent part. The grid points in the nozzle and in the expansion duct are spaced uniformly in each direction. The reservoir grid is stretched in x-direction on the last 30 points and in y-direction on the last 50 points with a ratio of 3% and 1% respectively. The grid in the spanwise z-direction is also spaced uniformly.

For the low pressure ratio case, shocks interact with the boundary layers developing along the walls of the expansion duct and a fine grid resolution in these regions is required. This can be accomplished easily by the overset grid approach that allows to patch grids of arbitrarily refinement in the regions of interest as shown in Figure 4.3 (b). Refined grids has been used to mesh the nozzle and the near wall zone of the expansion duct. Two simulations have been carried out using two different grids: a coarse grid where the grid spacing in the wall region is halved relatively to the center grid and a fine grid where the grid spacing in the wall region is quartered relatively to the center grid. More details about the coarse and fine grid and its grid sizes in wall units are given in Table 4.1 and 4.2.

The pressure and temperature of air at rest in the upstream reservoir (not considered in the simulation) is provided by the experiments $p_a = 101325$ Pa and $T_a = 293$ K. The sonic conditions imposed at the nozzle inflow are computed using isentropic relations [34]:

$$M_{in} = u_{in}/c_{in} = 1.01,\ v_{in} = 0,\ p_{in} = 0.5221\ p_a,\ T_{in} = 0.8306\ T_a.$$

The velocity profile at the nozzle inflow is kept uniform. By applying no-slip adiabatic wall conditions,

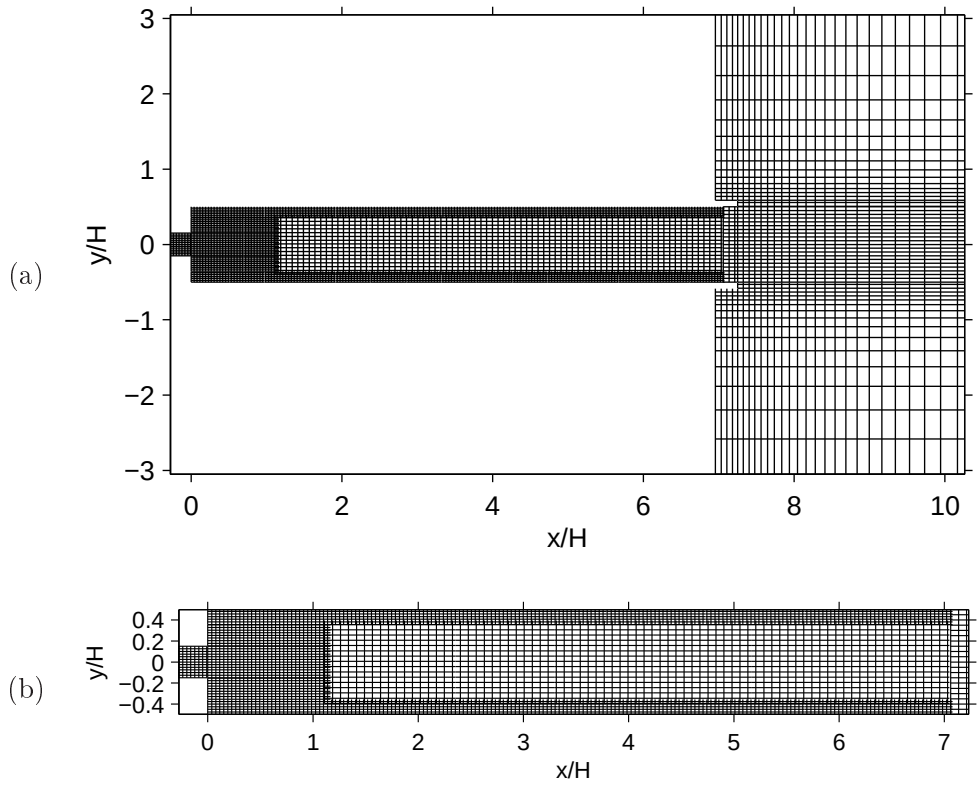

Figure 4.3: Grid generated by *ogen* for the computations at the the pressure ratio $\tau = 0.15$ ($x - y$ plane). The geometric parameters are $L = 0.24$ m, L/H = 7.23 and h/H = 0.3. Every eighth line is represented. Figure (a) shows the complete computational domain: the nozzle, the expansion duct and the outflow reservoir. Figure (b) is a detailed view on the nozzle and the expansion duct. The walls are refined using overlapping grids.

	N_x	N_y	N_z	Δx^+_{min}	Δy^+_{min}	Δz^+_{min}	N_{procs}
Nozzle	58	98	41	12	8	24	2
Expansion duct	744	127	41	24	16	24	22
Near wall grid	1439	47	41	12	8	24	2×9
Reservoir	180	398	41	24	16	24	16

Table 4.1: Characteristics of the coarse overset grid for the low pressure ratio case $\tau = 0.15$. The total number of 14×10^6 grid points have been distributed over $N_{\text{procs}} = 58$ processors. The length scales are given in wall units: $y^+ = yu_f/\nu$. The friction velocity $u_f = 4.3$ m.s^{-1} is determined near the outflow at $x = 0.2$ m.

a laminar velocity profile develops along the nozzle. Its development is reported in Figure 4.4 that shows the velocity profile at 3 positions in x-direction of the nozzle computed on the fine grid. The thickness of the boundary layer is 0.4×10^{-3} m and the developing boundary is resolved by 8 points using the fine grid. No further details about the boundary layer are given in the experiments.

The Reynolds number based on the nozzle height h and the inflow velocity u_{in} is $\text{Re}_h = 2.1 \times 10^5$. Along the walls of the expansion duct, adiabatic no-slip boundary conditions are imposed.

	N_x	N_y	N_z	Δx^+_{min}	Δy^+_{min}	Δz^+_{min}	N_{procs}
Nozzle	1491		41	6	4	24	2
Expansion duct	744	127	41	24	16	24	22
Near wall grid	3052	121	41	6	4	24	2×9
Reservoir	180	398	41	24	16	24	16

Table 4.2: Characteristics of the fine overset mesh for the low pressure ratio case $\tau = 0.15$. The total number of 46×10^6 grid points have been distributed over $N_{\text{procs}} = 253$ processors. The length scales are given in wall units: $y^+ = yu_f/\nu$. The friction velocity $u_f = 4.3$ m.s^{-1} computed for the coarse grid has been used, see Table 4.1.

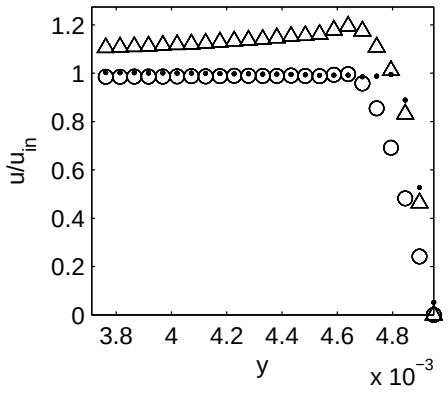

Figure 4.4: Velocity profiles of the laminar boundary layer in the nozzle of length $L_n = 9.1 \times 10^{-3}$ m at three positions: $\cdot$ at $x = -L_n$, $\circ$ at $x = -L_n/2$ and $\triangle$ at $x = 0$.

The pressure in the downstream reservoir $p_e = 17225$ Pa is fixed by the pressure ratio $\tau = 0.15$. The temperature in the downstream reservoir is given by $T_e = T_a = 293$ K. The non-reflective boundary conditions of Tam and Dong [127], extended to 3-D by Bogey and Bailly [28], are used along the reservoir boundaries. The turbulent flow leaves the computational domain without spurious acoustic reflections thanks to a sponge zone [28]. Periodic boundary conditions are used in spanwise direction.

The simulation has been carried out with the four stage Runge-Kutta scheme and the classical Jameson detector. A number of 5 $\times 10^4$ iterations has been run for the coarse grid computation in order to obtain a converged mean flow field. For the fine grid simulation, a number of 6 $\times 10^4$ iterations has been carried out.

4.2.2 Results

Mean flow

Mach Zehnder Interferometrie like plots showing the mean density iso-contours computed on the coarse and on the fine grid are represented in Figure 4.5 (a) and (b) respectively. Qualitatively the results correspond well to the experiments presented in Figure 4.2 (a). A divergent supersonic jet formed by the expansion waves that are generated at the nozzle edges is observed. A first oblique shock wave appears when the expansion waves are reflected by the upper and lower wall. In the

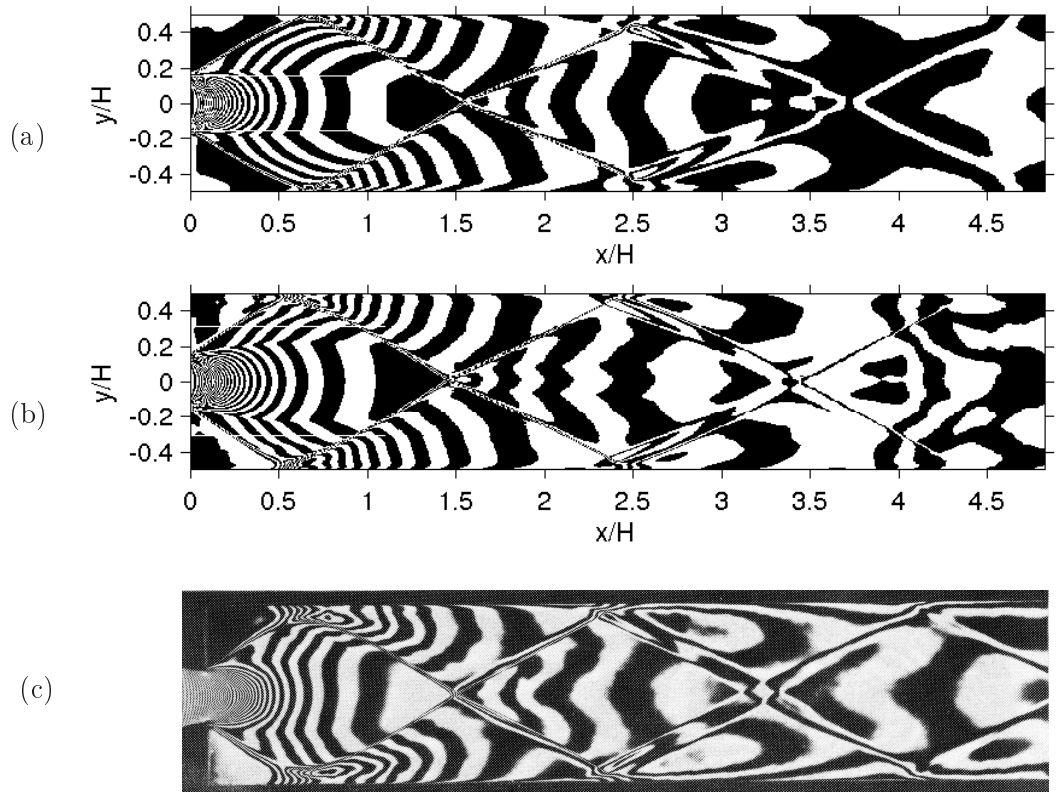

Figure 4.5: Mean density $\bar{\rho}$ for pressure ratio $\tau = 0.15$: (a) computed on coarse grid (see Table 4.1) using a Mach-Zehnder Interferometrie like colormap; (b) computed on fine grid (see Table 4.2) using a Mach-Zehnder Interferometrie like colormap; (c) visualized by Mach-Zehnder Interferometrie [94].

computation, the density maximum observed downstream of the jet reattachement is less extended in both computations. However, the fine grid computation reproduces the first interaction zone better than the coarse grid computation. A zoom on this zone is provided in Figure 4.6. The density maximum is slightly detached from the wall indicating more complex interactions.

The computed and measured static mean pressure $\bar{p}$, normalized by p_a, along the lower wall are displayed in Figure 4.7 (a) for the coarse grid computation and in 4.7 (b) for the fine grid computation. The computed and experimental curve compare well qualitatively. The first pressure peak caused by the jet reattachement is accurately predicted even though the peak is too narrow for the coarse grid. The fine grid computation seems to capture the pressure peak very well. The subsequent expansion fits very well with the experimental pressure curve for both computations. A second compression indicating the reflection of the oblique shock is also well predicted in its amplitude but is located too far downstream and deviates about 10% for the coarse grid and about 2% for the fine grid from the experimental location. For the coarse grid, this deviation is attributed to a difference of 2% of the computed and experimental pressure in the corner regions. This pressure indeed determines the entire flow regime in the downstream part of the expansion duct. In general, higher corner pressures lead to smaller expansion angles and more inclined shock waves are generated when the jet reattaches. The reason for the overpredicted pressure is not clear but might be attributed to an underresolution of the

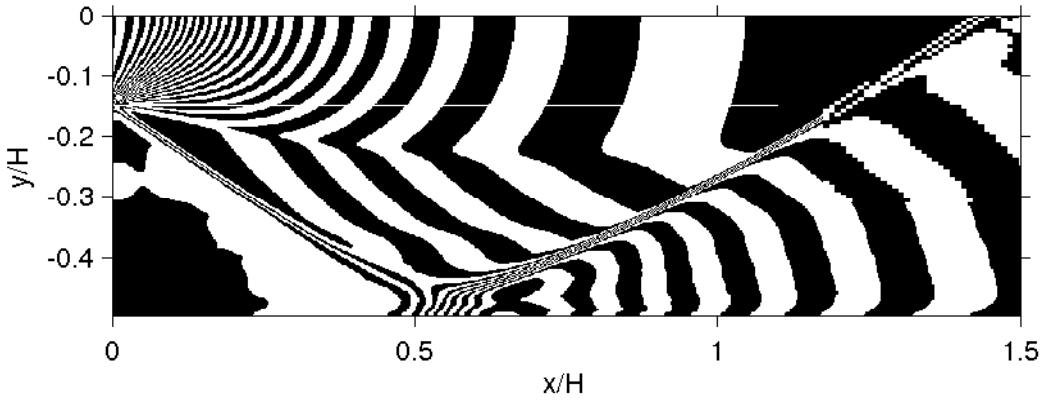

Figure 4.6: Zoom on the reattachement zone of the abruptly expanded jet: mean density is visualized by the Mach Zhender Interferometrie colormap.

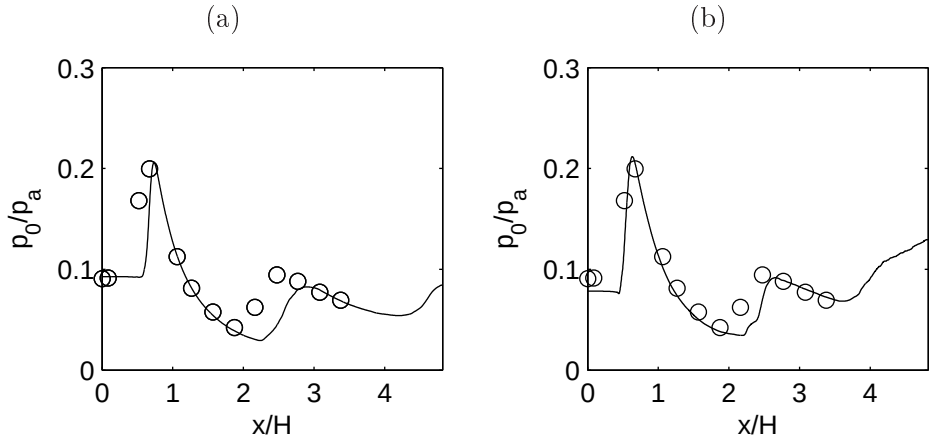

Figure 4.7: Static pressure distribution along the duct wall, obtained by: ——— the present computation; ∘ experiments [94]: (a) coarse grid computation (b) fine grid computation.

flow in the corner region, the reattachement region and of the incoming boundary layer.

Further downstream, the shock waves are reflected on the lower and upper wall respectively and form a symmetrical cell structure. Figure 4.5 (b) represents the mean pressure of the flow. The pressure in the corner regions does not match the pressure of the expanding supersonic jet. The mismatch is compensated by a normal shock near the nozzle edges. This can also be observed experimentally. The mean Mach number field, displayed in Figure 4.5 (c), confirms that the jet core is entirely supersonic and reaches its maximum speed upstream the first shock crossing location. The boundary layer thickens significantly at the shock reflection points. The flow in the corner region between the jet boundaries and the duct walls remains subsonic.

The existence of a universal law is examined. For incompressible equilibrium, zero-pressure-gradient, turbulent boundary layers, the mean velocity profile has a linear behavior $u^+_{\mathrm{VD}} = y^+$ for $y^+ \leq 5$ and a logarithmic behavior in the overlap layer $u^+_{\mathrm{VD}} = 0.42 \log(y^+) + 5.2$ for $10 \leq y^+ \leq 30$.

This law is validated for compressible flows when the van Driest transformation is applied [119].

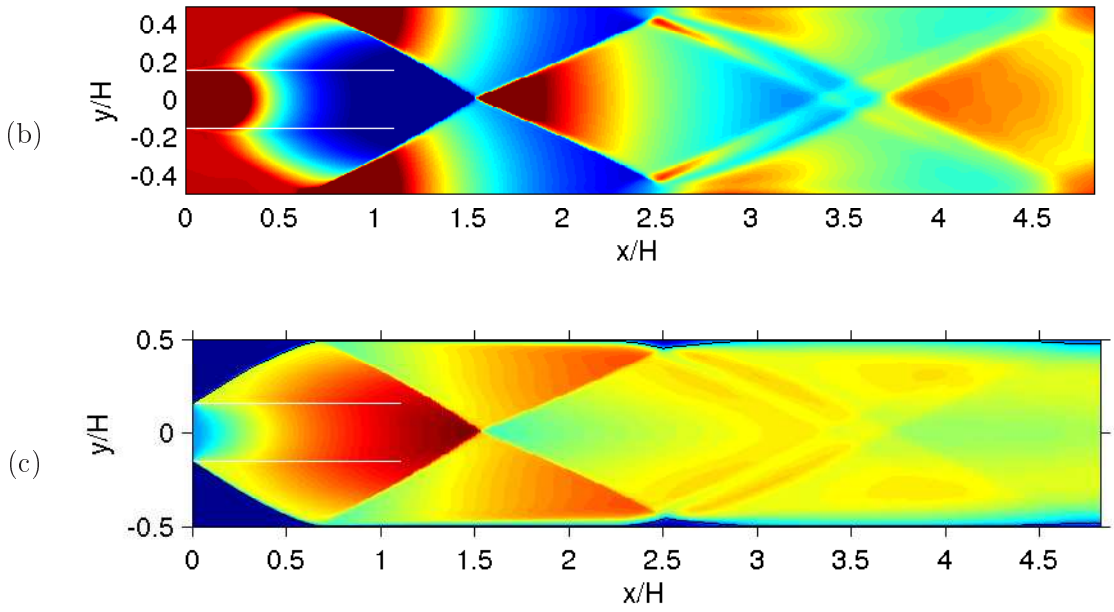

Figure 4.8: Computed mean flow properties for pressure ratio $\tau = 0.15$: (a) iso-contours of mean density $\bar{\rho}$ using a Mach-Zehnder Interferometrie like colormap; (b) mean pressure field (scale from 2000 Pa to 10000 Pa); (c) mean Mach number field (scale from 0 to 3.7).

The correction takes into account the variation of the viscosity through the boundary layer due to temperature variations. This transformation makes to collapse zero pressure gradient turbulent boundary layer data at Mach numbers up to $M = 12$, and the constants in the logarithmic law appear unchanged from their subsonic values. The van Driest transformation can be written as:

$$U_{\mathrm{VD}} = \int_0^{u_0^+} \sqrt{\frac{\bar{\rho}}{\rho}}\, du_0^+,$$

The van Driest transformed velocity profiles are given in Figure 4.9 for the fine grid computation at two different positions $x = 2\ H$ and $x = 3.5\ H$. The linear behavior is well captured by the computation. The mean flow profiles miss the logarithmic law. Propabely Further grid refinement would be necessary but is not affordable due to an excessive small time step.

Unsteady flow aspects

A boundary layer develops along the duct walls where the jet reattaches and interacts with the impinging oblique shock waves. Complex phenomena occur in such configurations as described in the review article of Dolling [46]. Instantaneous numerical Schlieren visualization of the entire computational domain is given in Figure 4.10 (a) for the fine grid computation. In the following, some interesting aspects will be discussed. As no unsteady data is given by the experiments for this pressure ratio, only qualitative comparison with similar cases issued from the literature can be carried out.

A zoom on instantanenous numerical Schlieren visualization in the jet reattachement region is

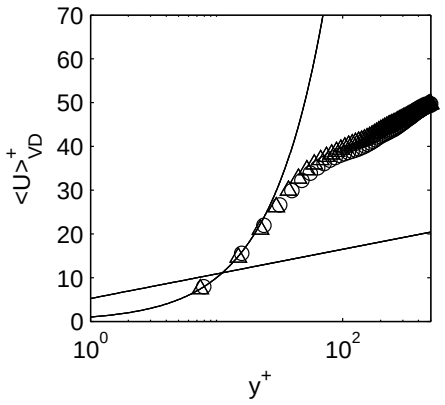

Figure 4.9: Van Driest transformed velocity profile at the positions $x = 2H$ ($\triangle$) and $x = 3.5H$ ($\circ$) for fine grid computation; ——— Mean velocity profile for incompressible equilibrium, zero-pressure-gradient, turbulent boundary layers: linear behavior $u^+_{\mathrm{VD}} = y^+$ for $y^+ \leq 5$; logarithmic behavior in the overlap layer $u^+_{\mathrm{VD}} = 0.42 \log(y^+) + 5.2$ for $10 \leq y^+ \leq 30$.

given in Figure 4.10 (b). The shear layer that represents a contact discontinuity limits the expanding jet. Small compression wave are emitted from the shear layer into the jet. Those are generated by instablities that develop and grow in the shear layer. For supersonic shear layers, the growth rate is small and the development of turbulent structures is retarded. When the shear layer impinges on the wall, mixing is enhanced making the rattachment zone to shift. Behind the jet reattachement zones, coherent structures that are sheded at low frequencies can be observed and might be linked to the instability development in the free shear layer further upstream.

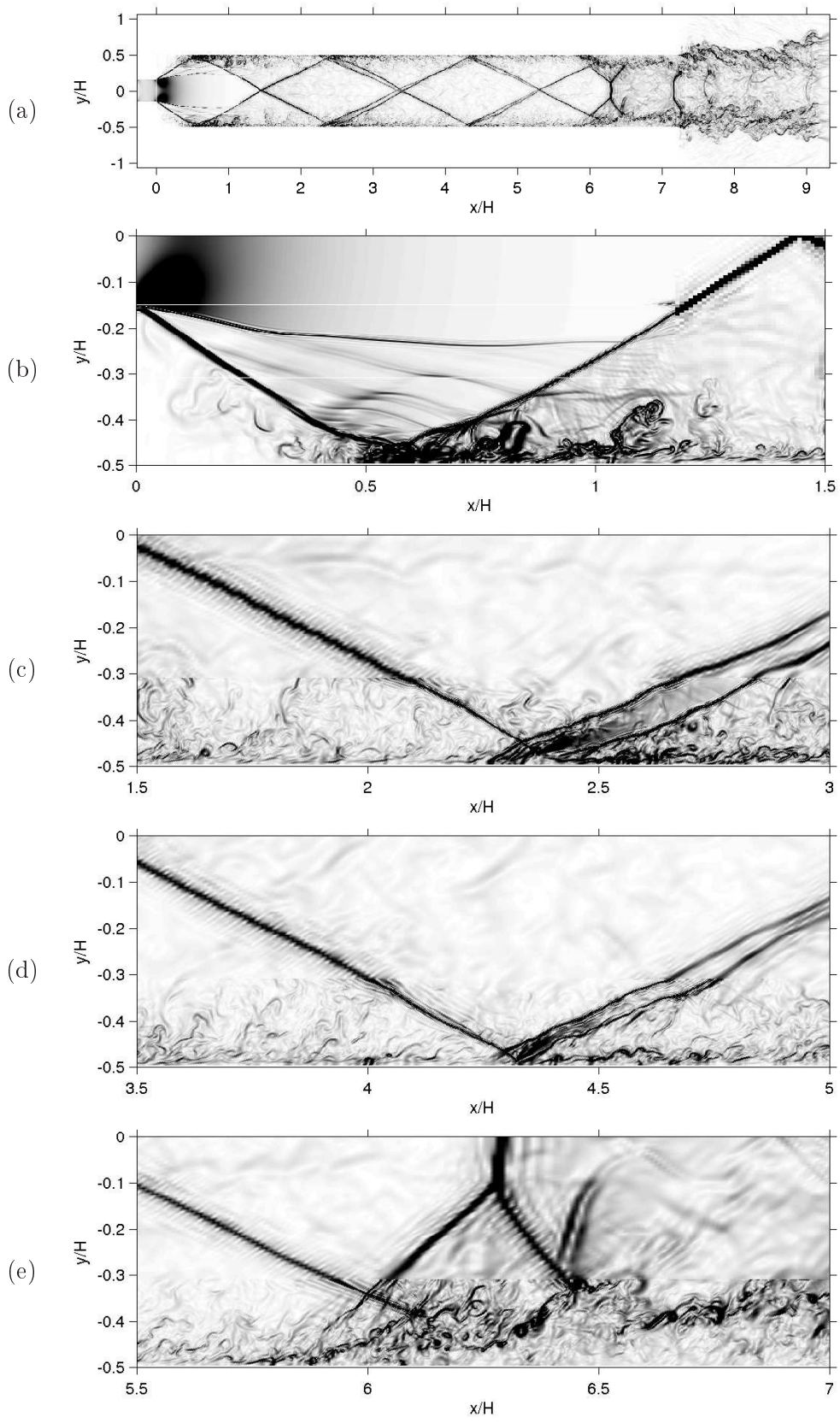

Figure 4.10: Instantaneous numerical Schlieren field $\nabla\rho$ (a) view on entire computational domain; (b) jet reattachement region; (c) first shock wave/ boundary layer interaction zone (d) second shock wave/ boundary layer interaction zone (e) Third shock wave/ boundary layer interaction zone with flow separation at the end of the duct.

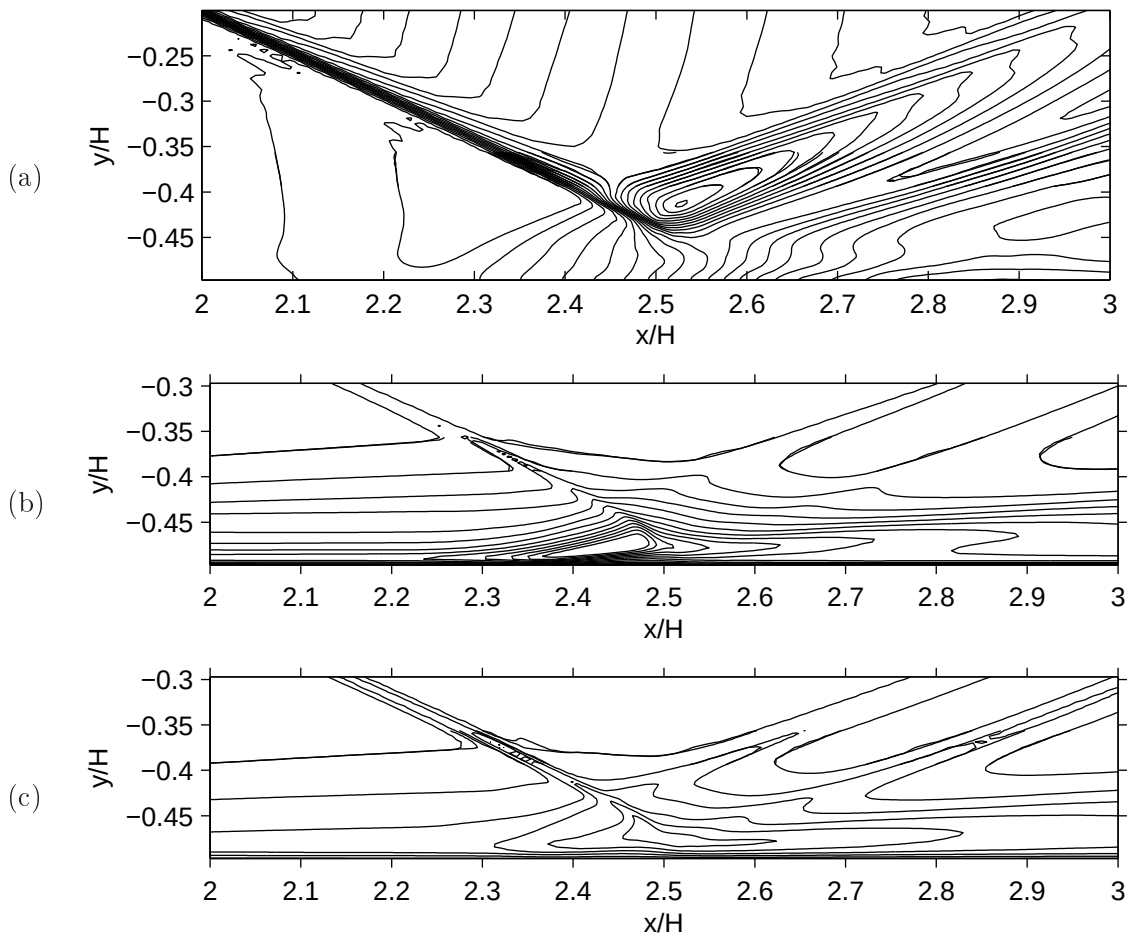

Figure 4.11: Detail view of the first shock wave/ boundary layer interaction: (a) computed mean pressure contours (31 contours spaced between 2000 and 10000 Pa); (b) iso contours of the turbulent kinetic energy k ranging from $0 \leq k \leq 25$ m^2.s^{-2} ; (c) iso contours of the shear stress τ_{xy}/ρ ranging from $0 \leq \tau_{xy}/\rho \leq 100$m^2.s^{-2}.

Visualizations of the instantaneous numerical Schlieren field of the first and second oblique shock-wave boundary layer interaction are given in Figure 4.10 (c) and (d). The incoming boundary layer seems to be transitional. Shock wave/ boundary layer interactions are observed and the downstream boundary layer is more turbulent. This mixing enhancement is typical for such interactions [119].

A detailed view on the first shock-wave boundary layer interaction on the lower wall is given in Figure 4.11 (a) representing the iso-contours of the time averaged pressure $\bar{p}$. The data is issued from the coarse grid simulation as the second order quantities for the fine grid computation are not converged up to this point. The incident shock is deviated towards the wall when entering the boundary layer and the reflected shock originates well upstream of the nominal impingement point due to the viscous interaction mechanism. A thickening of the boundary layer and small separation bubble can be observed.

The iso-contour lines of specific turbulent kinetic energy $k = (\overline{u'^2}+\overline{v'^2}+\overline{w'^2})/2$ and of $\tau_{xy}/\rho = \overline{|u'v'|}$, the turbulent shear stress, are represented in Figure 4.11 (c) and (d) respectively. The plot shows that

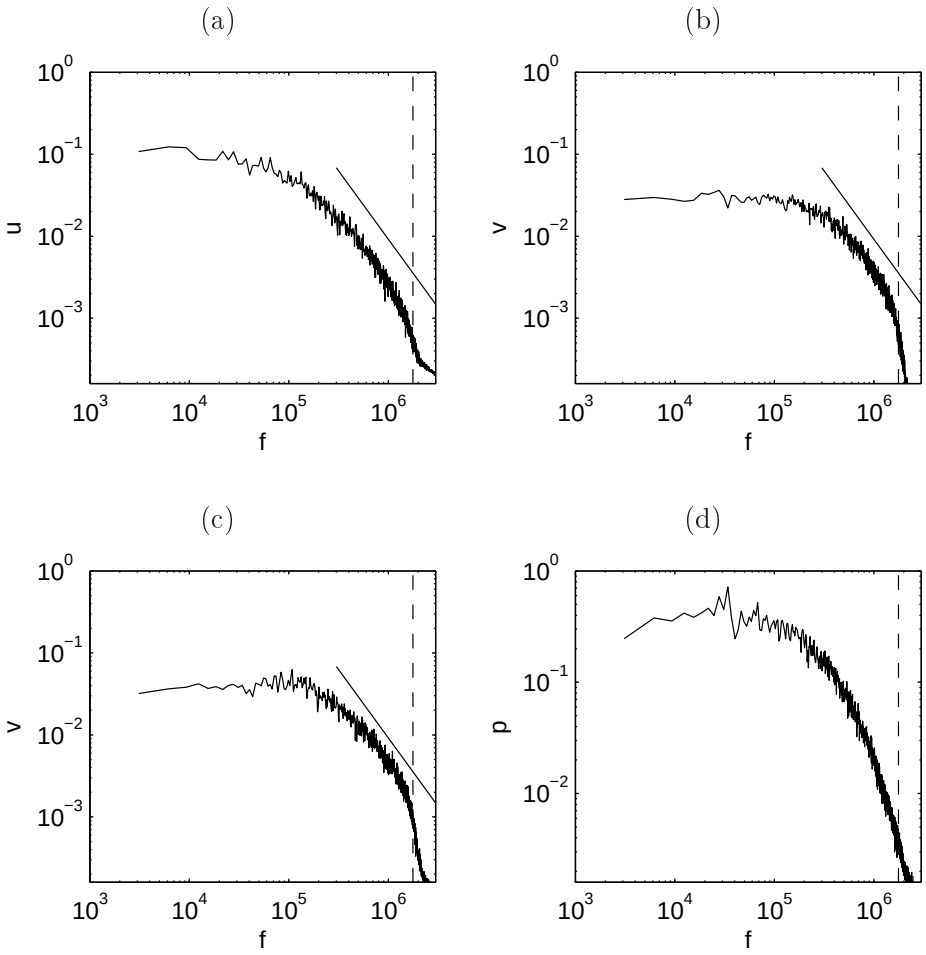

Figure 4.12: 1-D frequency spectra at $(x, y) = (3.5\ H, 15\Delta y^+)$;- - - - designates the cut-off frequency.

the turbulent kinetic energy k takes its maximum near the point of separation as observed by Pirozzoli *et al.* [98]. The turbulent shear stress reaches its maximum in the vicinity of the shock foot of the incident shock wave.

Figure 4.10 (e) shows the shock/boundary layer interaction near the outflow. The shock is normal and features a lambda shock. The boundary layer separates at the vicinity of the upstream foot leg. Turbulent mixing is enhanced.

1-D frequency spectra have been recorded at a position $(x, y) = (3.5\ H, 15\Delta y^+)$ and are given in Figure 4.12. The beginning of an energy cascade can be observed before the selective filter cuts off the high frequencies.

Beside these discrepancies, the present code is able to capture viscous as well as inviscid features of the flow. The passage of the oblique shock through the interpolation zone along $y/H \approx 0.3$ happens without creating spurious oscillations as they normally emerge when Lagrangian polynomials of higher-order come into play. The selective filter and the non-linear filter seems to eliminate those spurious modes efficiently. In the following, the expansion of a transonic flow for higher pressure ratios is presented.

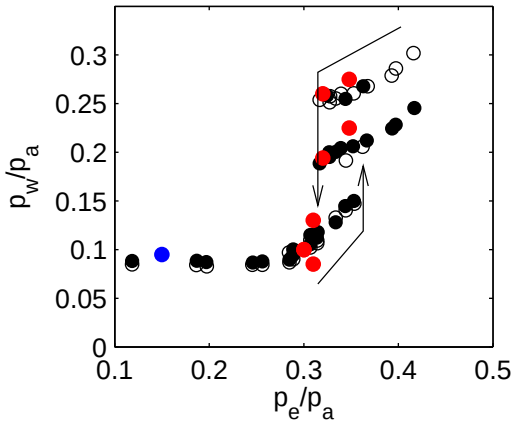

Figure 4.13: Static mean pressure measured in the corner region (∘ upper wall • lower wall) as a function of the pressure ratio τ: in black experimental values [94]; in red and blue the computed values for a duct of length $L = 0.16$ m and $L = 0.24$ m respectively.

4.3 The influence of the pressure ratio in the transonic regime

4.3.1 Experimental observations

The influence of the pressure ratio on the mean flow field has been investigated by Meier *et al.* for various duct geometries. Due to computational limitations, the following numerical study is done using the same duct as in the previous section, but with a reduced length $L = 0.16$ m. Figure 4.13 shows the normalized time averaged pressure $\bar{p}_w$ at the bottom and top corner region as a function of the pressure ratio τ, where $\bar{p}_w$ denotes the base pressure.

The mean base pressure $\bar{p}_w$ remains constant for low pressure ratios $\tau \leq 0.25$. Its values on both sides of the duct are the same and the flow is therefore symmetrical. The supersonic flow presented in section 4.2 is an example of this flow pattern. The computed base pressure is marked with a blue dot obtained for the longer duct. Above $\tau = 0.25$ the corner pressure increases on both sides. For this pressure ratio range, the oblique shock system has completely broken down. In the range from $0.305 \leq \tau \leq 0.352$ a large amplitude oscillation in the corner region can occur. Those large oscillations are associated with the coupling of the shock motion with the longitudinal duct modes such as described in the introduction. When these oscillations exist, the base pressure on both sides are low and of the same order of magnitude. The symmetrical flow is shown in Figure 4.2 (b).

With pressure ratios $0.316 \leq \tau \leq 0.352$ an additional flow pattern may occur in which the flow is asymmetrical and attached either to the top or bottom wall of the duct. In contrast to the symmetrical case, for the asymmetrical flow pattern no base pressure oscillations occur for the duct length $L = 0.16$ m. Figure 4.13 shows that two different base pressure values exist for the asymmetrical flow pattern: a lower value for the attached side and a higher value for the unattached side. No preferred attachment location to either the top or the bottom side has been observed experimentally.

The existence of the symmetrical, oscillating flow pattern or the asymmetrical, steady flow pattern depends whether the flow is driven with an increasing or a decreasing downstream pressure. In

(a)

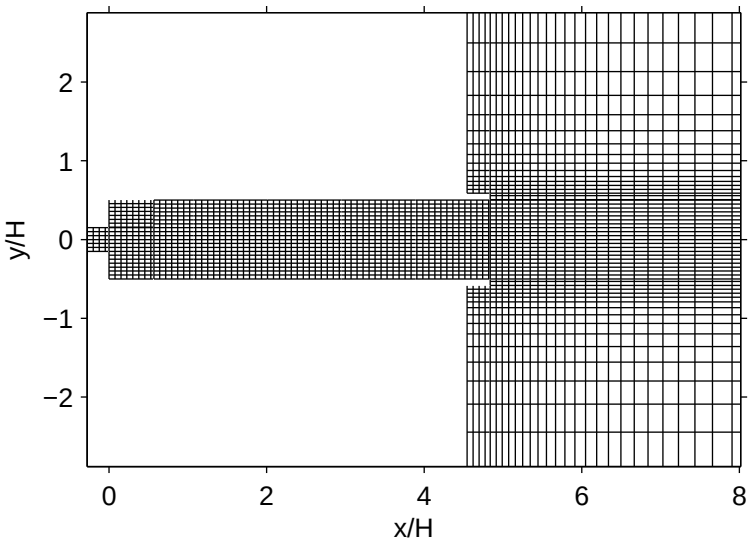

Figure 4.14: Visualization of the grid in the $x-y$ plane used for the cases of higher pressure ratios $0.30 \leq \tau \leq 0.348$. The geometric parameters are L = 0.16 m, L/H = 5.23 and h/H = 0.3. Every eighth grid line is represented.

the experiments the symmetrical oscillating flow pattern exists for an increasing pressure ratio until $\tau = 0.352$ and switches to an asymmetrical flow pattern. When the pressure ratio decreases the asymmetrical flow pattern switches to the oscillating flow pattern at $\tau = 0.316$. This hysteresis is indicated in Figure 4.13 by the arrows.

Four simulations with pressure ratios $\tau = 0.30$, $\tau = 0.31$, $\tau = 0.32$ and $\tau = 0.348$ have been carried out in order to check if it is possible to capture the symmetric flow pattern. As observed experimentally for this duct geometry aeroacoustic coupling between the shock motion and longitudinal duct modes occurs only with a symmetrical flow.

4.3.2 Simulation parameters

The grid is presented in Figure 4.14 that models a duct of length $L = 0.16$ m. Due to numerical limitations, no grid refinement near the duct walls are used for this study. The grid spacings are the same as in section 4.2 and are summarized in Table 4.4. The boundary conditions are applied as in the previous section. The same sonic inflow conditions as in section 4.2 are used. For the following cases, slip wall conditions are applied along the nozzle walls. This ensures that the boundary layer remains thin at the nozzle outflow.

The pressure ratios $\tau = 0.30$, $\tau = 0.31$, $\tau = 0.32$ and $\tau = 0.348$ impose exit pressures of $p_e = 30398$ Pa, $p_e = 31411$ Pa, $p_e = 32424$ Pa and $p_e = 35261$ Pa respectively. The temperature in the exit reservoir is given by $T_e = T_a = 293$ K.

4.3.3 Mean flow properties

The results of the four different computations are gathered in this section:

	N_x	N_y	N_z	Δx^+_{min}	Δy^+_{min}	Δz^+_{min}	N_{procs}
Nozzle	29	49	21	24	16	24	1
Expansion duct	490	161	21	24	16	24	15
Reservoir	180	398	21	24	16	24	16

Table 4.3: Grid parameters for the high pressure ratio cases $0.30 \leq \tau \leq 0.348$. All these cases have been computed using $N_{\text{procs}} = 32$ processors. The total number of grid points is about 5.0×10^6.

- $\tau = 0.30$:

  A rendered 3-D visualization of iso-surfaces of instantaneous numerical Schlieren and vorticity (spanwise component ω_z) is given in Figure 4.15 (a). The flow features a strong normal shock wave. The flow is symmetrical and the normal shock interacts with the attaching jet by forming a bifurcating or lambda shock on the lower and upper wall. The front leg of the bifurcation is the oblique shock wave that is generated when the supersonic jet is deflected by the duct walls. The upstream leg must exist to give proper continuity of the flow direction. Supersonic layers start at the lambda shock and are attached to the upper and lower duct wall. In the vortex sheet, separating the supersonic near wall layers and the subsonic flow in the duct center, 2-D instability rolls develop. These instabilities give rise to turbulent 3-D structures near the duct outflow. The plot of mean Mach number in the $x-y$ plane in Figure 4.17 (a) confirms that the flow downstream the normal shock is subsonic. The flow downstream the lambda shock remains supersonic up to $x/H \approx 3$. The averaged shock position is smeared, due to large shock motions. Figure 4.16 (a) shows the iso contours of the time averaged density, using a Mach-Zehnder Interferometrie like colormap. The normalized static mean pressure computed along the lower and upper wall is plotted in Figure 4.20. The wall pressure curves show a symmetrical behaviour. The pressure is constant in the base region and increases in the reattachement zone. The pressure exhibits its maximum further downstream at $x/H \approx 2$ and matches the downstream reservoir pressure at the end of the duct. The pressure in the base region at $x = 0$ is plotted in Figure 4.13 and is in very good agreement with the experimental values.

- $\tau = 0.31$:

  An increase of the reservoir pressure p_e leads to an asymmetrical flow as Figure 4.15 (b) illustrates. A slightly inclined normal shock can be observed. At the lower wall the normal shocks ends up with a lambda structure situated more upstream than in the $\tau = 0.30$ case. The 2-D vortex rolls develop further downstream. 3-D turbulent structures can already be observed at $x/H \approx 3.4$. On the upper wall the jet is separated from the wall. The jet shear layer is thickened thanks to instability development. The mean Mach number field displayed in Figure 4.17 (b) shows the inclined normal shock configuration. The upper supersonic layer is separated from the wall, is more extended in downstream direction and thicker than the lower one. The turbulent character of the this flow is illustrated in Figures 4.18 (a) and (b) showing the turbulent kinetic energy $k = (\overline{u'^2} + \overline{v'^2} + \overline{w'^2})/2$ and the turbulent shear stresses $\tau_{xy}/\rho = \overline{|u'v'|}$ respectively. High levels

are localized along the upper jet shear layer. They reach a maximum in the interaction zone with the normal shock. Less turbulent energy is produced on the lower side. The turbulent level grows near the walls and along the vortex sheets and reaches a saturation in the last quarter of the duct. The mean pressure computed along the upper and lower wall are given in Figure 4.20 (b). The pressure in the lower corner region reaches a value similar to the one obtained for lower pressure ratios. The subsequent compression is caused by the shock that is located slightly more upstream as in the upper case. The pressure in the upper corner region is increased and the compression takes place further downstream. The base pressures are also plotted in Figure 4.13 and agree well with the experiment. This kind of asymmetry was observed in the experiments only for longer ducts.

- $\tau = 0.32$:

  Figure 4.15 (c) shows the flow pattern obtained for $\tau = 0.32$. The flow is asymmetric and is separated entirely from the lower duct wall. The iso-surfaces of vorticity shows how the jet cross-section is initially intact and how it begins to break up and mix more efficiently at the middle of the first shock cell. On the lower wall regularly spaced strong perturbations that travel upstream can be observed. The Mach number field given in Figure 4.17 (c) exhibits two shock cells and a reversed flow is found on the lower duct wall. The jet reattaches after the end of the second shock cell. No major jet spreading can be observed such as observed for free jets. Turbulence data given in Figure 4.19 (a) and (b) show high turbulent kinetic energy production along the upper and lower shear layers. On the attached side turbulent production is endorsed by the presence of the wall. On the lower wall, the turbulent energy has reached its maximum downstream the first shock and drops to a constant stagnant value up to the end of the duct. This indicates a transition to a fully turbulent flow. The static mean pressure along the upper and lower wall are plotted in Figure 4.20 (c). The pressure at the duct end on the upper wall matches the reservoir pressure after the sequence of expansion and compression waves. The pressure curve at the lower duct wall does not feel the presence of the shock and increases slowly and ends up to match the reservoir pressure. Figure 4.13 reveals the excellent agreement of the normalized base pressures with the upper branch of the experimentally measured curve.

- $\tau = 0.348$:

  The flow pattern of this pressure ratio is very similar to the case with $\tau = 0.32$. The jet is attached on the upper wall. The jet expansion angle is smaller due to the increased pressure ratio. As shown in Figure 4.13, the pressure computed in the corner region are slightly over estimated compared to experiments.

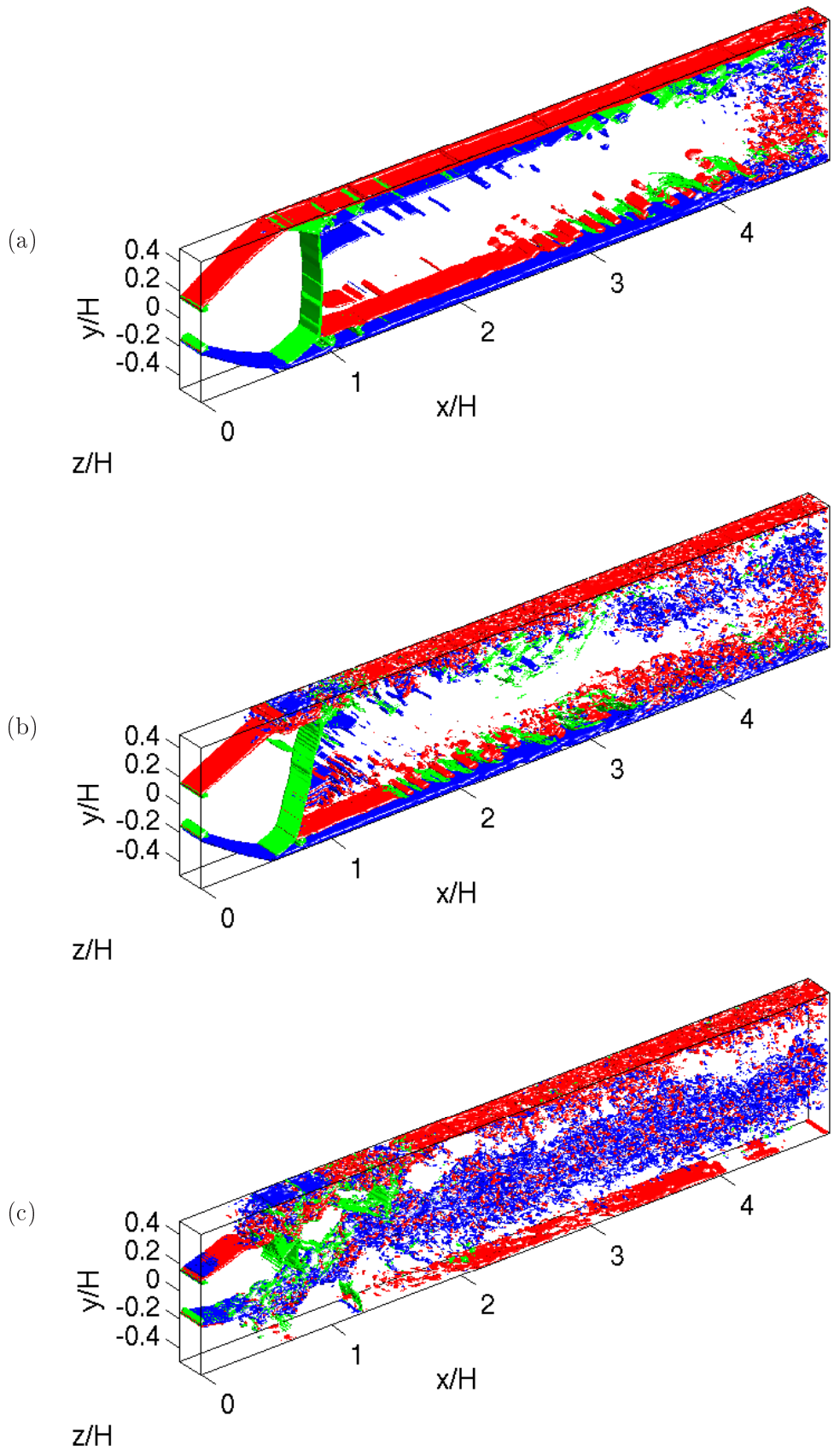

Figure 4.15: Rendered 3-D view of iso-surfaces: red and blue surfaces represent instantaneous spanwise vorticity field for $\omega_z = +150000\ \mathrm{s}^{-1}$ and $\omega_z = -150000\ \mathrm{s}^{-1}$ respectively, green surfaces represent numerical Schlieren with $\nabla\rho = 200\ \mathrm{kg.m}^{-4}$ for different pressure ratios: (a) $\tau = 0.30$, (b) $\tau = 0.31$ and (c) $\tau = 0.32$.

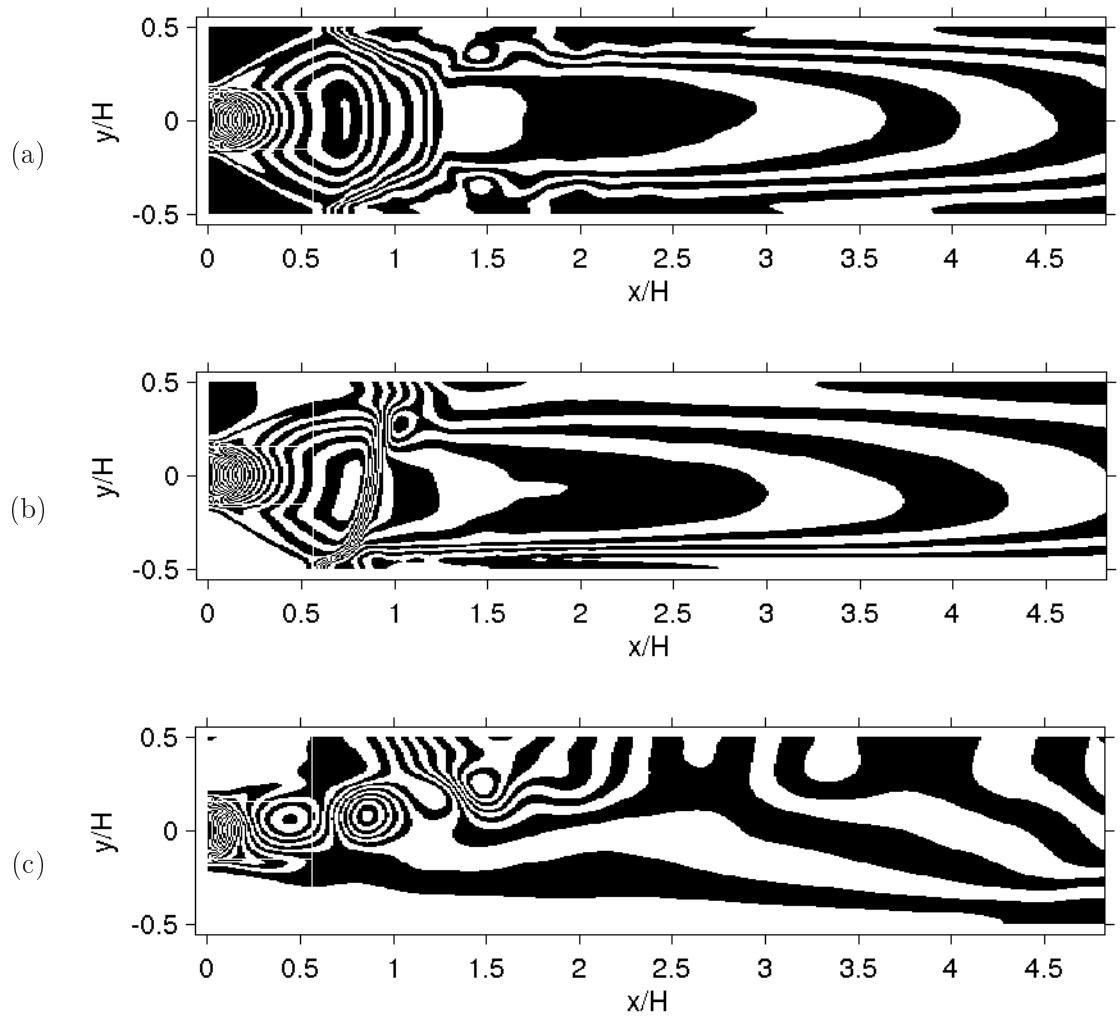

Figure 4.16: Iso-contours of the mean density $\bar{\rho}$ for different pressure ratios: (a) $\tau = 0.30$, (b) $\tau = 0.31$, (c) $\tau = 0.32$.

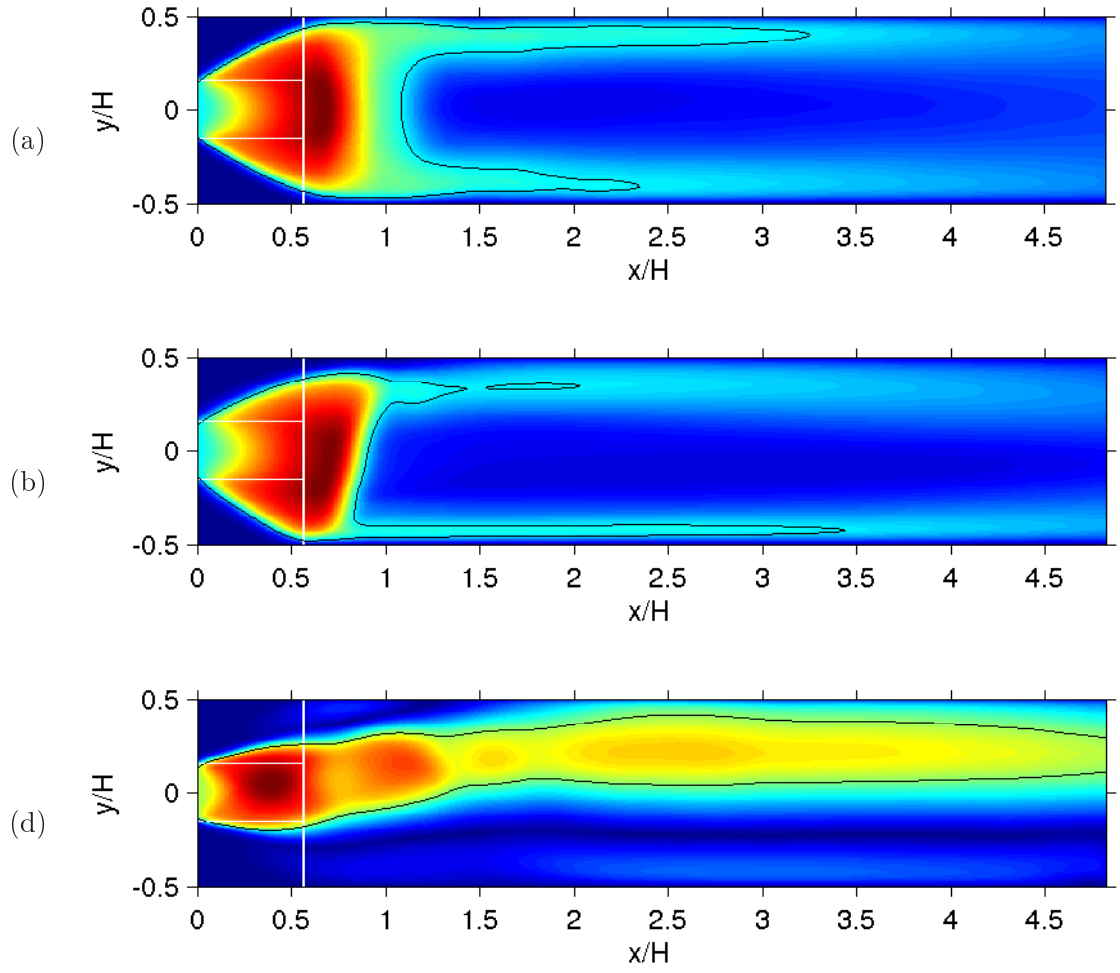

Figure 4.17: Mean Mach number field $M = |\bar{\mathbf{u}}|/\bar{c}$ for different pressure ratios: (a) $\tau = 0.30$, (b) $\tau = 0.31$, (c) $\tau = 0.32$; the color scale lies in the range $0 \leq \bar{M} \leq 2.1$. ——— represents the sonic line $M = 1$.

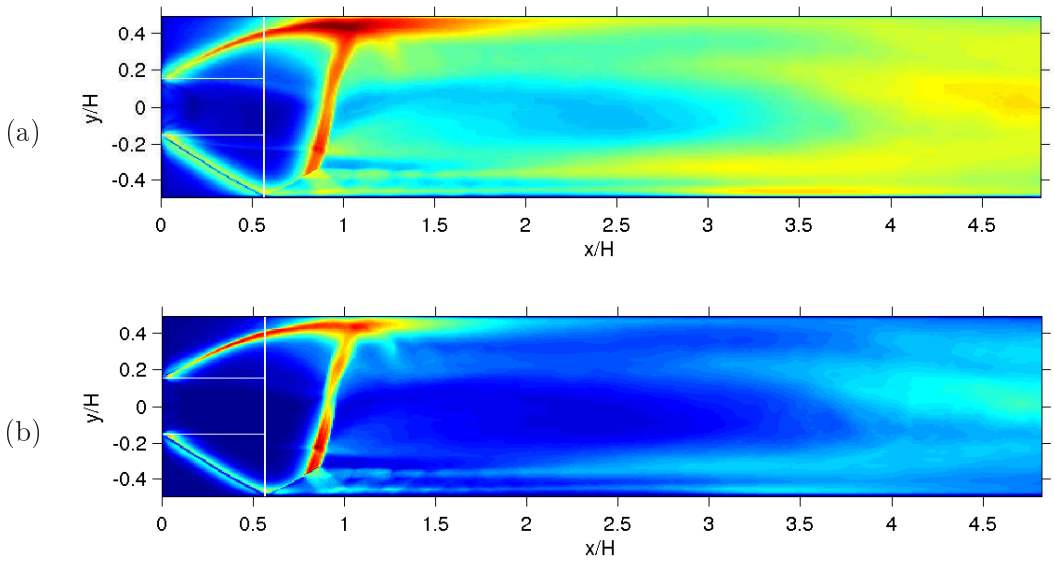

Figure 4.18: Turbulent data for the pressure ratio $\tau = 0.31$: (a) turbulent kinetic energy: the color scale range from $0 \leq k \leq 20$ m^2.s^{-2}; (b) turbulent shear stresses: the color scale range from $0 \leq \tau_{xy}/\bar{\rho} \leq 90$ m^2.s^{-2}.

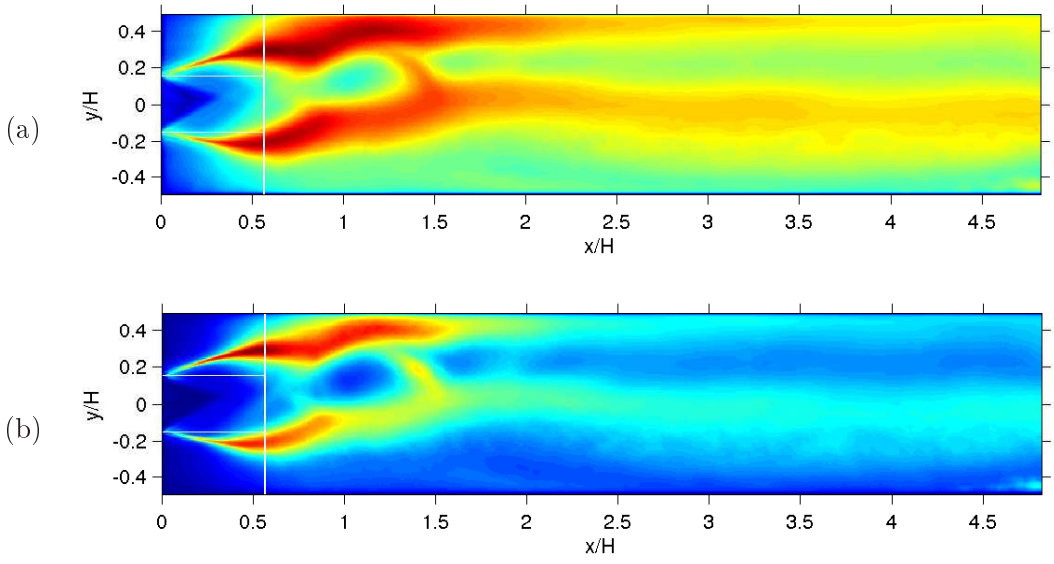

Figure 4.19: Turbulent data for the pressure ratio $\tau = 0.32$: (a) turbulent kinetic energy: the color scale range from $0 \leq k \leq 25$ m^2.s^{-2}; (b) turbulent shear stresses: the color scale range from $0 \leq \tau_{xy}/\bar{\rho} \leq 100$ m^2.s^{-2}.

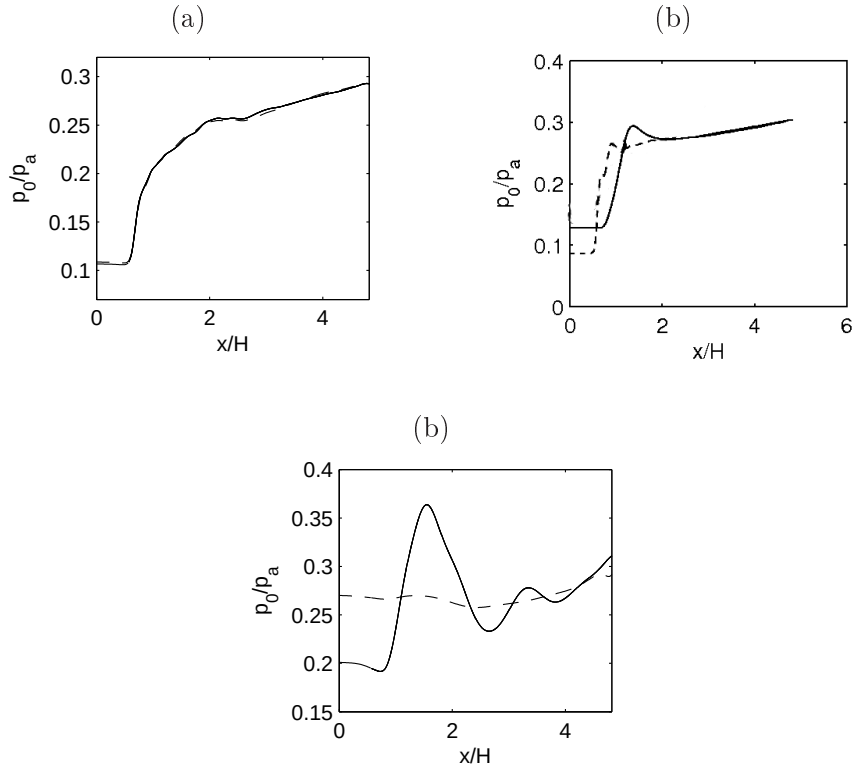

Figure 4.20: Static mean pressure measured on the lower (- - - - -) and upper (———) wall for different pressure ratios: (a) $\tau = 0.30$, (b) $\tau = 0.31$, (c) $\tau = 0.32$.

4.3.4 Unsteady flow aspects

The pressure signals recorded along the upper wall are examined for the flows computed for the pressure ratios $\tau = 0.31$ and $\tau = 0.32$.

- $\tau = 0.31$:

  The signal on the upper wall at the corner ($x = 0$) and at the duct end ($x = L$) are plotted in Figure 4.21. Regular small amplitude oscillations in the base region are observed. At the duct end, broadband noise dominates. Sound pressure levels are provided in Figure 4.22 (a) at three positions ($x = 0$, $x = L/2$ and $x = L$). Low frequency components, at $x = 0$ and at $x = L/2$, are observed. Those components are not present at the end of the duct. The pressure spectra reveal a high frequency component at $f \approx 4500$ Hz. This frequency is associated to the transverse duct modes that are excited by the turbulent broadband noise.

  During the simulation run a switch to a symmetrical flow pattern has been observed. The time history is given in Figure 4.23 (a). When this happens, strong pressure oscillations occur which is consistent with experimental observations. The pressure spectra obtained for a signal, when the flow is symmetrical is given in Figure 4.23 (b). The pressure signals exhibit a high amplitude, low frequency peak at $f \approx 350$ Hz. The reason for this switch that has random nature is not clear up to now. However, this phenomenon underlines the importance of the presence of a symmetrical flow pattern, for the computation of transonic resonance.

- $\tau = 0.32$:

  For $\tau = 0.32$, no low frequency oscillations can be observed. A frequency $f \approx 1500$ Hz is dominant. A high-frequency mode at $f \approx 5000$ Hz is also observed for this pressure ratio.

  For this computation, the influence of the shock capturing is considered. As observed for the validation test cases, the shock capturing can be minimized by the use of a high-order Jameson detector. Two computations have been carried out: one using the Jameson filter and one using the modified detector based on the selective 11-point filter. The obtained 1-D spectra are given in Figure 4.24. Using the classical detector leads to slightly lower amplitudes especially for w, the velocity component in spanwise direction. This might be an indication that the transition to a turbulent state of the shear layer might be retarded due to higher dissipation introduced by the low order shock capturing filter. Using the classical Jameson detector, an energy cascade is well captured and can be observed for the velocity component u over one frequency decade. Using the modified Jameson detector, the signal is disturbed by high frequency components. The origin of these high frequency components is propably due to the reduced low-order dissipation in the shock regions leading to a higher aliasing error.

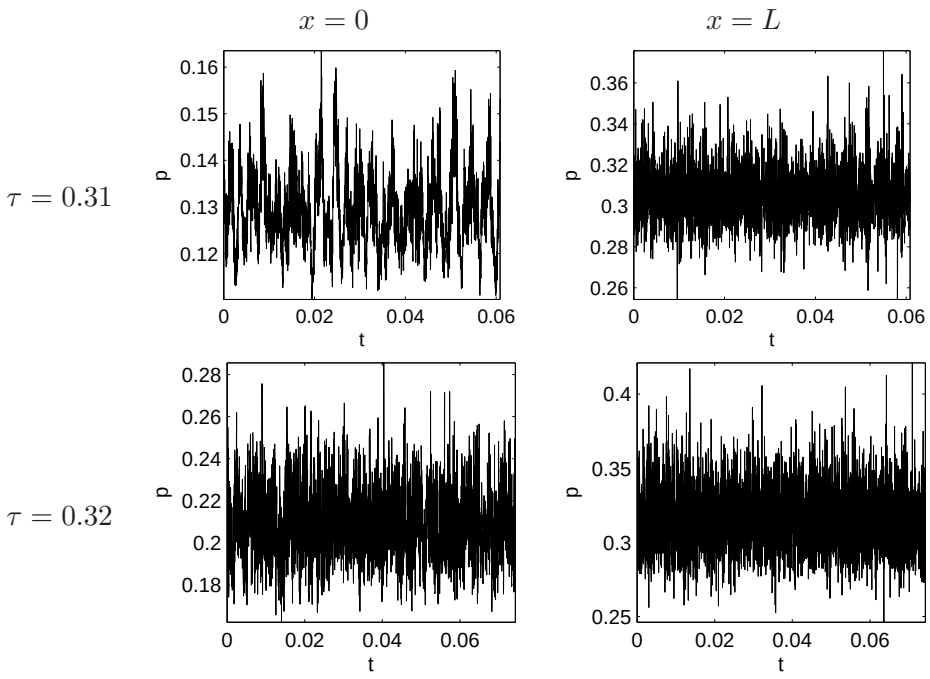

Figure 4.21: Pressure signals recorded at the upper wall for different pressure ratios for $\tau = 0.31$, $\tau = 0.32$.

No areoacoustic coupling is detected by the present simulation when the flow is asymmetrical. This is consistent with the experiments that does not exhibit aeroacoustic coupling when the asymmetric transonic flow regime is established in the duct. The dominance of the asymmetric flow pattern can be caused by the application of periodic boundary conditions in the spanwise direction. The pressure in the upper and lower corner regions cannot be kept in balance as it would be the case when the lateral walls are present: the jet destabilizes and attaches to one duct side more easily.

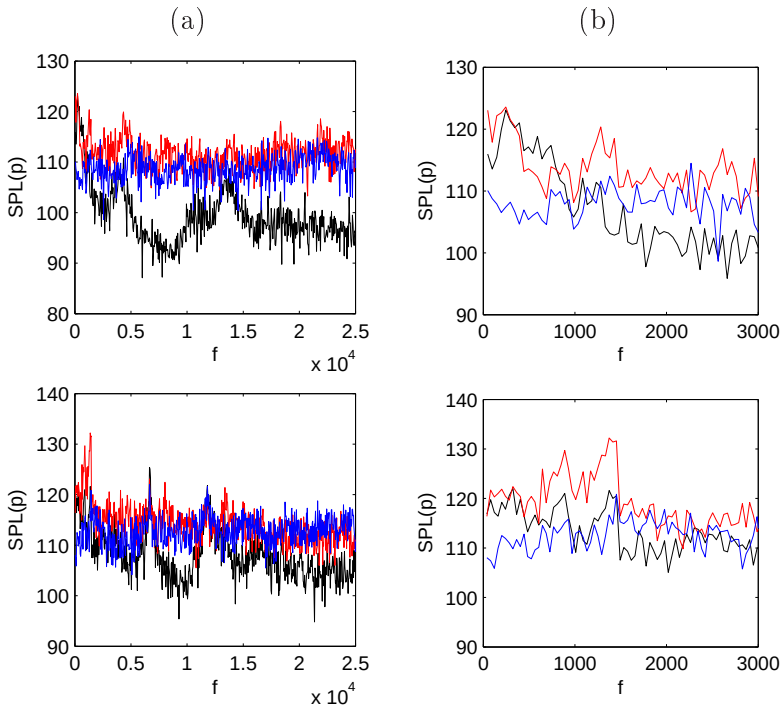

Figure 4.22: Spectra of pressure signals recorded on the upper wall at three positions —— $x = 0$, —— $x = L/2$, —— $x = L$ for different pressure ratios (a) $\tau = 0.31$, (b) $\tau = 0.32$.

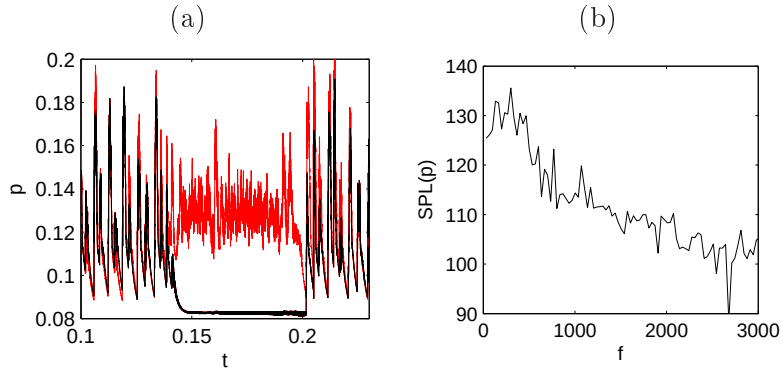

Figure 4.23: (a) Time history of the pressure measured in the corner region at $x = 0$ on the lower (——) and upper —— wall; (b) Pressure spectrum of a signal, when symmetrical flow pattern dominates.

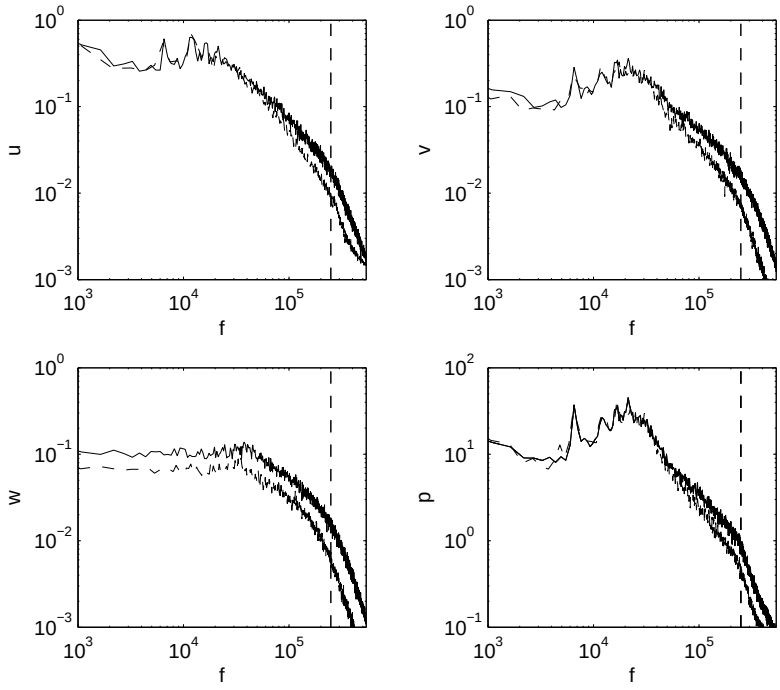

Figure 4.24: 1-D spectra for the pressure ratio $\tau = 0.32$ using the Jameson detector (- - - -) and the modified Jameson detector based on 11-point selective filter (——-).

4.4 Transonic resonance

A new grid has been built using the approximately the same number of grid points as in the previous section but taking a duct length of $L = 0.08$ m and an aspect ratio $\phi = 0.4$. This has two advantages: (a) the Reynolds number is decreased and (b) the new aspect ratio prefers a more symmetric flow regime as it is shown in Figure 4.27 (b). The plot shows the pressure in the corner p_w measured as a function of the outflow pressure p_e. The hysteresis region for this duct length is much smaller than for the longer duct case $L = 0.16$ m such as given in Figure 4.13.

	N_x	N_y	N_z	Δx^+_{min}	Δy^+_{min}	Δz^+_{min}	N_{procs}
Nozzle	29	65	21	12	8	12	6
Expansion duct	490	161	21	12	8	12	77
Reservoir	180	398	21	12	8	12	82

Table 4.4: Grid parameters for $L = 0.08$ m, $L/H = 5.33$ and $\phi = 0.4$ for $\tau = 0.42$. All these cases have been computed using $N_{\text{procs}} = 165$ processors. The total number of grid points is about 5×10^6.

The computation is carried out using a pressure ratio of $\tau = 0.41$, where transonic oscillations have been observed experimentally. In the following, the aerodynamic properties of the mean flow field are presented. Then, unsteady flow aspects are considered and the coupling of the shock oscillations with longitudinal duct modes is explained.

4.4.1 Aerodynamic field

Mean properties

Figure 4.25 shows the computed field of the mean number of the flow including the reservoir. The flow is symmetrical. A normal shock can be observed in the upstream part of the duct. The mean shock position is slightly smeared indicating that the shock oscillates. The flow downstream the normal shock is subsonic and layers with higher speeds can be observed near the upper and the lower duct wall. The subsonic jet downstream of the duct spreads as it is observed for free jets.

The Mach-Zehnder interferometrie like plot of the time averaged mean density in Figure 4.26 (a) compares qualitatively well with an instantaneous visualization for a similar flow regime observed with a longer duct with $L = 0.16$ m, $\phi = 0.3$ and $\tau = 0.364$ in Figure 4.26 (b).

The corresponding computed time averaged static pressure distributions along the upper and lower duct walls are given in Figure 4.27 (a). After the expansion, the compression zone indicates the location of the strong normal shock. Further downstream, the static pressure on the upper and the lower duct converges to a value that is close to the downstream pressure $p_e = 0.41 p_a$.

The time averaged pressures in the upper and lower corner region p_w obtained by computation are compared to the experimental values given as a function of the pressure ratio $\tau = p_a/p_0$ in Figure 4.27 (b). The mean pressure computed in the upper and lower corner is in excellent agreement with the measured corner pressure.

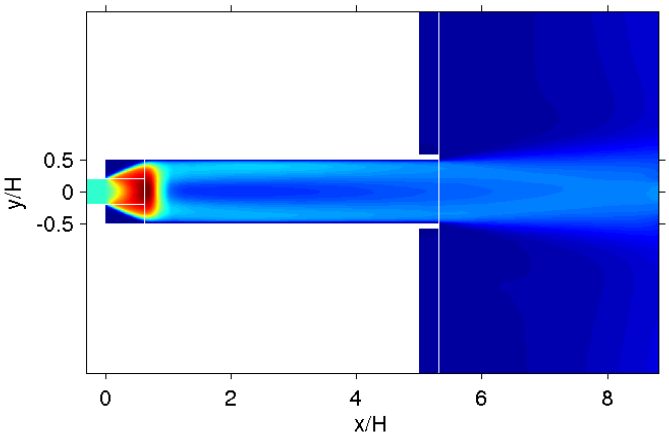

Figure 4.25: Computed time averaged Mach number field for $\tau = 0.41$ for a expansion duct length L = 0.08 m and aspect ratios L/H = 5.33 and h/H = 0.4. Color scales from 0 to 2.3.

A relation between the corner pressure and the Mach number downstream is given in the Meier *et al.* [94]:

$$\frac{1-\phi}{\phi}\frac{p_w}{p_0} = \left(\frac{2}{\gamma+1}\right)^{\frac{\gamma+1}{2(\gamma-1)}} \frac{1+\gamma M_e^2}{M_e\sqrt{(1+\frac{\gamma-1}{2}M_e^2)}} - (\gamma+1)\left(\frac{2}{\gamma+1}\right)^{\frac{\gamma}{\gamma-1}}, \tag{4.1}$$

where M_e is the Mach number behind the shock. Its derivation is has been reproduced in the Appendix B.

This relation is plotted in Figure 4.28 (a) for different nozzle aspect ratios $0.1 \leq \phi \leq 1.$. The Mach number behind the shock increases with increasing aspect ratios ϕ. This is due to an increased acceleration of the flow and increased Mach numbers upstream the normal shock. For the computed pressure a Mach number of $M_e = 0.51$ can be computed by equation (4.1) and is in good agreement with the computed Mach number along the centerline $y = 0$ of the duct, given in Figure 4.28 (b). The mean pressure and the time averaged speed of sound are given in Figure 4.29 (a) and (b) respectively.

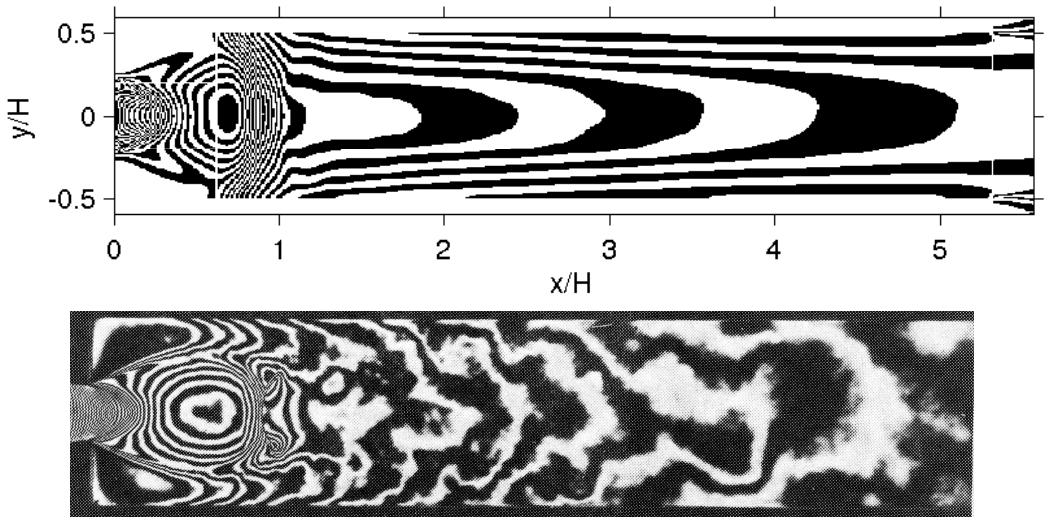

Figure 4.26: Mach-Zehnder interferometry visualizations of the time averaged density at pressure ratios: (a) computed for $\tau = 0.41$ for a expansion duct length L = 0.08 m and aspect ratios L/H = 5.33 and h/H = 0.4. (b) visualized experimentally for $\tau = 0.364$ for a expansion duct length L = 0.24 m and aspect ratios L/H = 7.23 and h/H = 0.3 [94].

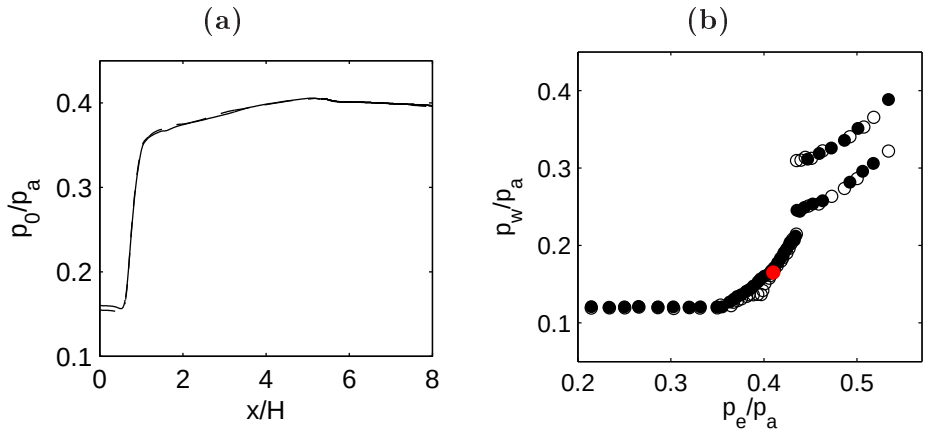

Figure 4.27: **(a)** Time averaged static mean pressure computed along the upper ——— and lower wall – – – ; **(b)** Time averaged static mean pressure measured in the corner region (○ upper wall • lower wall) as a function of the pressure ratio τ: in black experimental values [94]; in red the computed values for a duct of length $L = 0.08$ m.

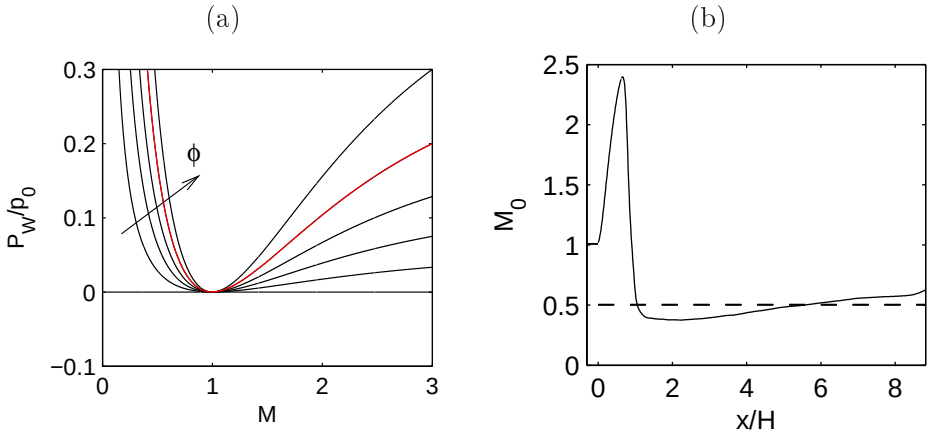

Figure 4.28: (a) Corner pressure as a function of the Mach number downstream of the shock for increasing aspect ratios ϕ; —— $\phi = 0.4$; (b) Local time averaged Mach number along the centerline $y = 0$; - - - - - theoretically predicted Mach number using equation (4.1).

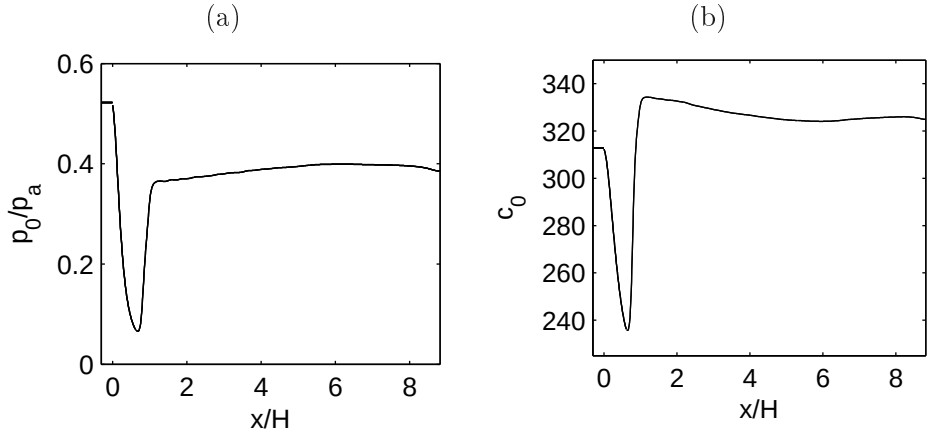

Figure 4.29: Time averaged quantities along the centerline ($y = 0$): (a) pressure; (b) speed of sound.

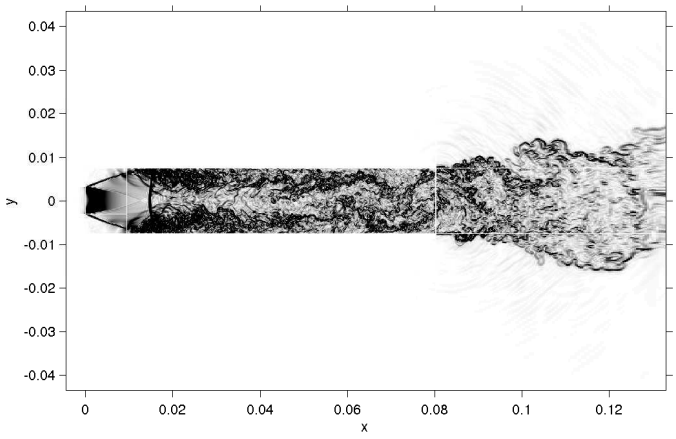

Figure 4.30: View on numerical Schlieren $|\nabla\rho|$ in a $x-y$-plane of the entire computational domain.

Instantaneous flow visualizations

Figure 4.30 shows the instantaneous numerical Schlieren field of the entire computational domain. The jet is exhausted at the outflow of the expansion duct. The jet is received by the sponge layer and fine scale vortical structures are dissipated without generating spurious sound. Thus the sponge layer is well suited. The acoustic waves that originate at the outflow of the test duct leave the computational domain without spurious reflections.

4.4.2 Shock oscillations

Figure 4.31 (a) and (b) compare two instants of the shock-oscillation cycle for the experiment and the computation by visualizing the iso-density contours. The flow visualizations show two extreme positions of the shock during a shock oscillation cycle. When the shock is closest to the nozzle, the subsonic center flow is more extended to the walls. In the second visualization the shock reaches its position farthest from the nozzle. The subsonic region is more narrow. The computed density field compares well with the experiments.

In the following, the self-exciting mechanism of the base pressure oscillations is explained. For that a sequence of the instantaneous Mach number field is given in Figure 4.32. The mechanism corresponds to the explanations of Meier *et al.* [94].

In frame 1, the dead-air region is connected to the downstream region by a subsonic layer on both sides of a central supersonic flow near the nozzle exit. The supersonic flow ends with a strong normal shock which is followed by subsonic flow in the central part of the field. Supersonic regions are formed downstream of the extremities of the normal shock. A pressure drop in the corner region makes the jet to spread and to reattach on both duct walls (frame 2). Meier *et al.* [94] noticed that the pressure drop is caused by an entrainment of air by the jet and a subsequent evacuation of the corner region. This causes an expansion and an acceleration of the transonic jet. The entrainment of air is increased and the expansion is therefore a self-amplifying process. Once the jet reattaches, the reattachement point

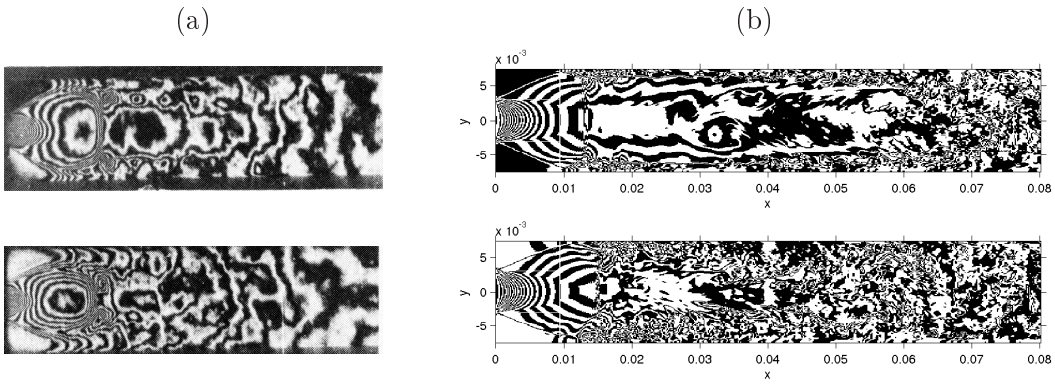

Figure 4.31: Time sequence of shock oscillation cycle: (a) the experiments for a longer duct ($L = 0.16$ m, $L/H = 4.82$, $\Phi = 0.3$); (b) computed results are visualized by a Mach-Zehnder-interferometrie-like colormap.

moves in upstream direction (frame 2 and 3). The expansion angle of the jet increases and the normal shock is moving upstream and reaches a position closest to the nozzle (frame 3). The jet velocity is increasing and the pressure therefore increases behind the shock. The pressure rise downstream of the reattachement zone makes the boundary layer to separate. The jet separates completely from the upper and lower duct wall (frame 4). The pressure rises in the corner region due to a compression wave that travels through the slit between the separated jet and the duct wall. In the experiments the pressure is amplified by a strong back flow in the corner region. The height of the normal shock reduces (frames 4-7) and the pressure behind the shock decreases. The shock moves downstream until reaching the most downstream position in frame 7. In frame 8, an expansion of the jet is observed. The jet begins to reattach to the duct wall and the loop is closed.

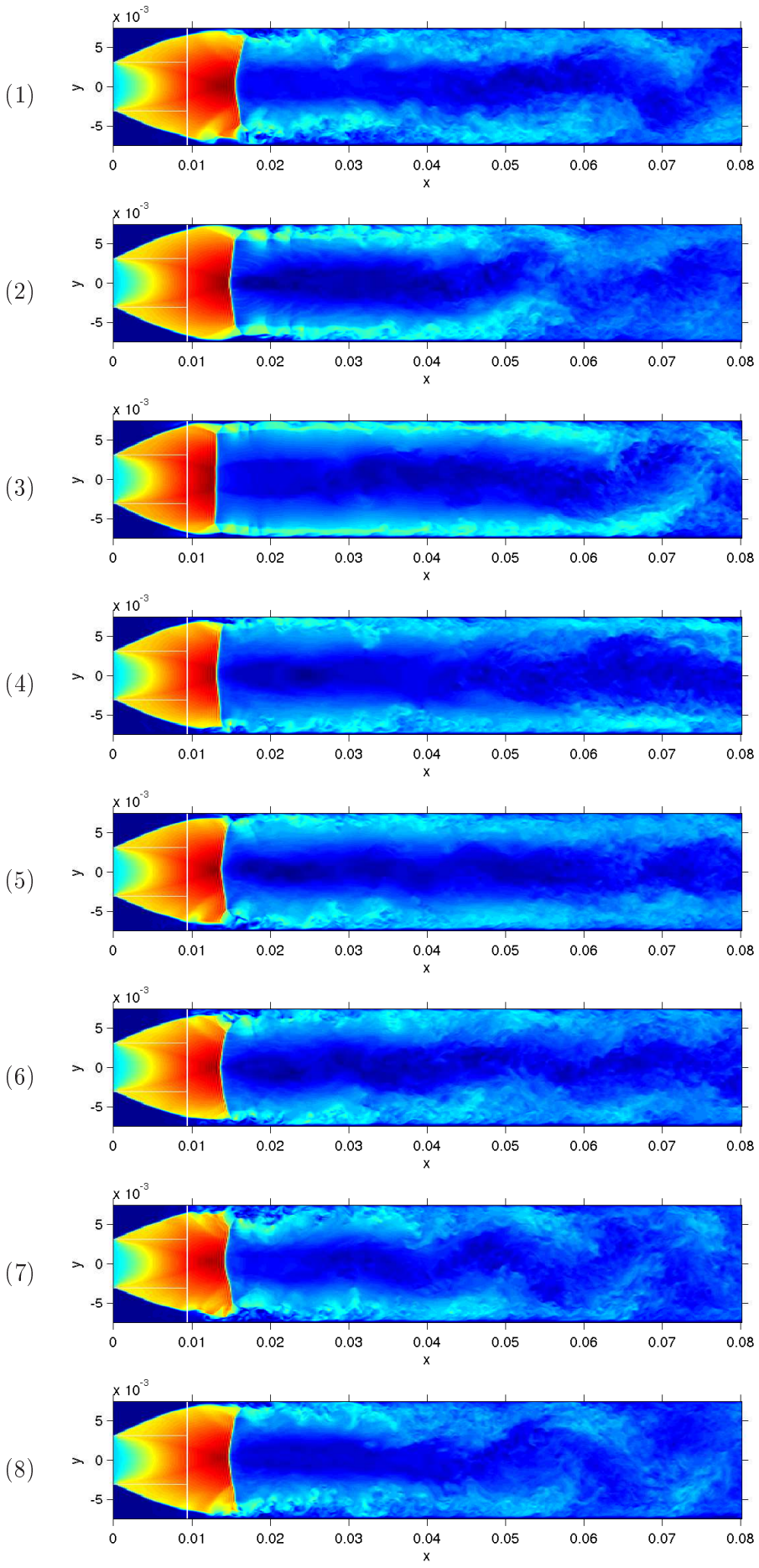

Figure 4.32: Time sequence of shock oscillation cycle: local Mach number (color scales from 0 to 3).

4.4.3 Aeroacoustic coupling

The self-exciting mechanism such as explained in the previous section exists without a coupled resonator. In this case, the pressure oscillations are irregular and weak. Coupling takes place only when the oscillation frequency of the shock is close to the longitudinal duct resonance frequencies.

The spectral densities of signals recorded along the upper duct wall are given in a 3-D plot of Figure 4.33 (a). A peak can be observed at $f = 710$ Hz. The amplitude diminishes when approaching the duct end. This indicates the presence of a standing acoustic wave in the duct.

The natural frequencies can be estimated in order to show that the base pressure oscillations are controlled by duct resonance. Assuming a 1-D flow the frequencies can be estimated by

$$f_{\text{duct},n} = (2n-1)(1-M_e^2)\,\frac{c_e}{4L}, \quad \text{for } n = 1, 2, 3 \;\text{ etc.} \tag{4.2}$$

where n is the duct mode number. This expression gives the frequencies of $(2n-1)\times$ quarter standing waves which are supported by a duct that is closed at one end ($u' = 0$) and that is open at the other end ($p' = 0$). The term $(1 - M_e^2)$ takes into account the mean Mach number M_e of the subsonic flow behind the normal shock. The mean sound speed of the flow is denoted by c_e. Note that the upstream part of the duct can be treated as a closed end because a sonic flow is present at the throat at all times and no information can travel upstream through the nozzle.

Equation (4.2) identifies, beside the duct length, the speed of sound as a determining parameter of the duct resonance. The mean Mach number is subsonic in the case of a normal shock. Meier *et al.* [94] estimated the downstream mean Mach number by a 1-D approach that can be found in the work of Jungowski [75]. The speed of sound has been determined from tables of adiabatic flow. The experimentally measured frequencies and the theoretically predicted frequencies of the base pressure oscillations are plotted in Figure 4.33 (b) as a function of the pressure ratio τ for a duct of length $L = 0.08$. The theoretical frequencies compare well with the measured ones indicating a coupling of shock oscillation and longitudinal duct modes.

For the simulated case, the mean Mach number $\bar{M}_e$ and the mean sound velocity $\bar{c}_e$ are computed using an average defined by

$$\bar{M}_e = \frac{1}{L}\int_{x_s}^{x_s+L} \bar{M}_{y=0}\,dx, \quad \bar{c}_e = \frac{1}{L}\int_{x_s}^{x_s+L} \bar{c}_{y=0}\,dx,$$

where the quantity x_s is the shock position and $\bar{M}_{y=0}$, $\bar{c}_{y=0}$ are the centerline distribution of the mean Mach number and sound speed, given in Figure 4.28 (b) and 4.29 (b) respectively. The computed frequency and the theoretical predicted frequency are given in Figure 4.33. First, the frequency of the computed result compare well with the measured frequency. Second, the theoretical frequency compare well with the duct mode frequency given by equation (4.2). This indicates that the shock oscillations are controlled by longitudinal duct modes.

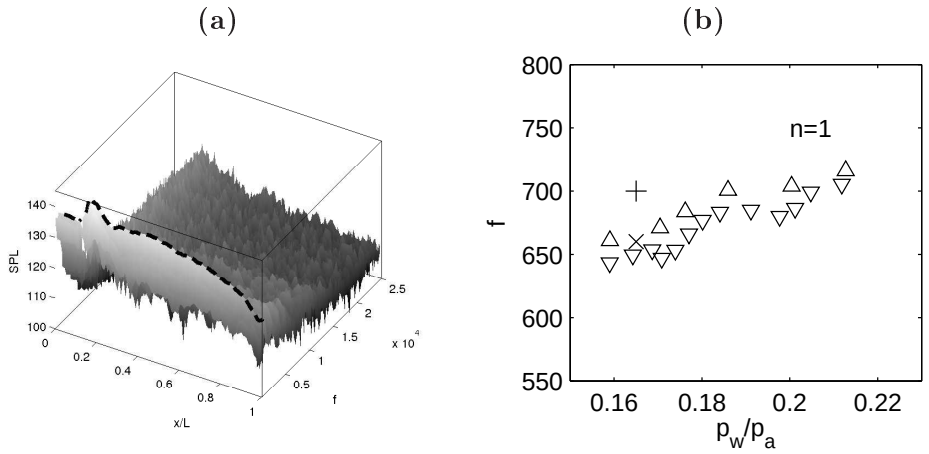

Figure 4.33: **(a)** Spectra of pressure signals recorded along the upper wall; - - - designates the dominant frequency at $f = 710$ Hz; **(b)** Frequencies of base pressure oscillations as a function of the pressure ratio τ for a duct of length $L = 0.08$ m; $\triangle$ experimental values [94] $\triangledown$ theoretically predicted values for the first longitudinal duct mode $n = 1$ using equation (4.2) [94]; $+$ the computed values $\times$ theoretical predicted values using equation (4.2)

4.5 Conclusion

The numerical algorithm is able to reproduce in a satisfying way the expansion of a transonic flow in a duct for various pressure ratios and duct geometries. First, the expansion of a transonic flow in a rectangular duct is computed for a pressure ratio leading to an entirely supersonic flow. The aerodynamic field is found to be in good agreement with experiments. Second, several simulations of the same configuration for different pressure ratios, where coupling between normal shock motion and longitudinal duct modes are likely to occur, are presented. An investigation of the influence of pressure ratio on the mean flow field shows that the present numerical algorithm is able to reproduce the main flow patterns in a satisfying way. The abrupt switch from symmetrical to asymmetrical flow pattern is well predicted and follows the hysteresis branch obtained for decreasing pressure ratios. The asymmetric flow pattern is the preferred configuration of the numerical simulation. In agreement with experiments, no aeroacoustical coupling is observed for the asymmetrical flow pattern. Third, a simulation were conducted where the symmetric flow pattern is captured. As observed by the experiments coupling between the shock oscillations and longitudinal duct modes occurs.

General conclusion

In the present work, a high-order algorithm based on centered finite-difference schemes has been developed for direct computation of aeroacoustic phenomena in complex geometries.

The first chapter is dedicated to the description of the numerical algorithm SAFARI (Simulation Aéroacoustique de Fluides Avec Resonances et Interactions). The governing equations, the Euler and Navier-Stokes equations, are solved with high-order optimized finite-difference schemes. In order to treat compressible flows, a first-order Jameson-like shock-capturing filter has been used. The filter is applied locally in the vicinity of shocks. The shock location is detected with a Jameson sensor. A high-order overset-grid approach is used in order to treat complex geometries with structured grids. The complex data structure is provided by a grid assembly software *ogen*, part of the freely available library *Overture*, that has been interfaced with SAFARI. The solver is parallelized using the standard MPI library and each grid can be computed on an arbitrary number of processors for the purpose of load balance. High-order Lagrangian polynomials are used for grid boundaries where the grid points do not coincide. The solver is portable on several massively parallel platforms. Computations involving 50×10^6 grid points with 250 processors have been carried out.

In the second chapter, the multi-domain ability and the influence of the implemented shock-capturing filter are validated with typical test cases found in the litterature. The convection of a vortex through an interpolation zone has been first examined. In particular, the generation of spurious sound when a vortex passes through an interpolation zone has been considered as a function of the polynomial order used for interpolation. The diffraction of a monopolar pressure source by a cylinder have been computed on a single-block grid and on an overset grid. These two test cases reveal that the accuracy of the high-order finite-difference scheme can be recovered when Lagrangian polynomials of sufficiently high-order are used. The computation of entropy/shock wave interaction and the computation of the sound/shock wave interaction problem reveal an impact of the shock-capturing filter on the small scale perturbations. The dissipation can be minimized using a modified Jameson sensor that is based on high-order dissipation terms. Furthermore, the computation of a low Reynolds number flow and a 3-D circular shock tube demonstrate that SAFARI is able to treat geometries involving grid singularities and complex overset-grid structures.

In the third and fourth chapter, SAFARI has been applied to two configurations typical for industrial applications of EDF. The two planar configurations have been solved in 3-D with periodic boundary conditions in spanwise direction.

The first application is the ducted cavity at low Mach number regime. In the experiments a strong

coupling between the cavity modes and the transverse duct modes has been observed. In order to show the numerical evidence of the coupling, computations with varying Mach numbers have been carried out. This coupling has been successfully reproduced by the algorithm. Despite some discrepancies in amplitude, the frequencies have been very well retrieved.

The second test case is the computation of a suddenly expanded transonic flow in a rectangular duct. The flow regime is governed in particular by the pressure ratio. For very low pressure ratios, the flow in the planar duct is entirely supersonic. The computation exhibits good agreement with the flow visualizations and wall pressure measurements. Furthermore the influence of the pressure ratio on the flow regimes has been examined. For higher pressure ratios, two flow regimes have been observed in the duct: a symmetrical and an asymmetrical field. The observed regime depends whether the pressure ratio increases or decreases, showing a hysteresis phenomenon. In the experiments, only the symmetrical flow regime has produced strong aeroacoustic coupling between shock oscillations and longitudinal resonance modes. From an industrial point of view, it is therefore crucial to know whether the symmetrical or the asymmetrical flow regime is stable. Numerically the hysteresis and the abrupt switch between the two regimes have been well reproduced. Then, the coupling for a symmetric flow regime is computed using a duct configuration where the hysteresis is less dominant. The shock oscillations have been well reproduced. The frequencies measured in the duct indicate that the longitudinal acoustic duct modes are excited.

The computation of these two industrial cases demonstrates that SAFARI is able to reproduce aeroacoustic phenomena in different flow regimes using affordable computer resources. The present work has shown that flows with industrial relevance can be computed using high-accuracy numerical techniques.

Outlook

SAFARI has been applied to 3-D flows using periodic boundary conditions in the third direction. The next step should be to take into account the entire 3-D geometry of the real gate valve, presented in Figure 1 (b).

In this work, the solver has been developed for static grids. In the future, the solver should be extended in order to tackle with overlapping grids that move relative to each other. The main configurations of interest are aeroelastic vibrations of turbine low pressure blades. For this purpose, the interface between *Overture* and SAFARI has to be developed because interpolation data has to be updated at each time step.

Another point that should be considered in the future is the use of multi-time stepping methods in order to overcome the constraining CFL condition of explicit time stepping for wall-bounded flows. This development should be quite easy due to the multidomain structure of SAFARI.

Appendix A

Conservativity aspects of finite-difference schemes

In CAA, finite-difference schemes are more popular than finite-volume methods as its order of accuracy can be increased easily. Additionally, they can be tuned in order to have minimum dispersion and dissipation over a certain wave-number range. However, finite-difference methods are non conservative, compared to finite-volume methods that ensures conservation of mass, momentum and energy per construction.

In the following, a finite-volume formulation of a centered finite-difference scheme is presented, when the governing equations are solved in conservation from. Furthermore, using conservative operators finite-difference operators ensure conservativity for flows containing shocks.

Finite-volume formulation of finite-difference

The finite-volume formulation of finite-difference schemes is considered in 1-D, using the following model non-linear equation in conservation form:

$$\frac{\partial u}{\partial t} + \frac{\partial f(u)}{\partial x} = 0,$$

where $u = u(x,t)$. On a uniform gird with grid spacing Δx, the spatial derivative is discretized in the finite-difference approach by the following expression:

$$\left|\frac{\partial f(u)}{\partial x}\right|_i \approx \frac{1}{\Delta x} \sum_{r=-n}^{n} a_r f_{i+r}$$

Conservative finite-volume approaches are based on the integral conservation law of a grid element limited by $x_{i-1/2} \leq x \leq x_{i+1/2}$ such as shown in Figure A.1 which leads on the semi-discrete form:

$$\frac{\mathrm{d}}{\mathrm{d}t} \int_{x_{i-1/2}}^{x_{i+1/2}} u \; dx + f_{i-1/2} - f_{i-1/2} = 0.$$

The fluxes at the interface $f_{i-1/2}$ are computed via interpolation of the points at the cell centers x_i. This step is also known as reconstruction step. The interpolation can be expressed in terms of a

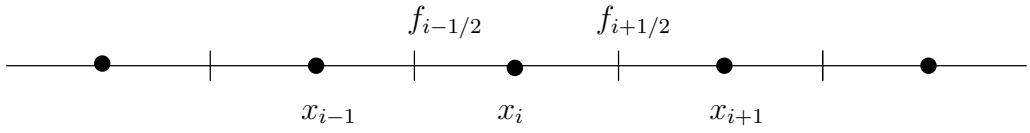

Figure A.1: Denotations used for the finite-difference and finite-volume approach.

finite-difference approximation as:

$$f_{i-1/2} = \sum_{j=1}^{n} b_j (f_{i-1+j} + f_{i-j}), \quad f_{i+1/2} = \sum_{j=1}^{n} b_j (f_{i+j} + f_{i+1-j}),$$

where b_j are the coefficients for a interpolation. The finite-difference form can be recasted in a finite-volume like form such as

$$\begin{aligned}
\sum_{r=1}^{n} a_r (f_{i+r} - f_{i-r}) &= \sum_{r=1}^{n} b_r (f_{i+r} + f_{i+1-r} - f_{i-1+r} - f_{i-r}) \\
&= \sum_{r=1}^{n} b_r (f_{i+r} - f_{i-r}) + \sum_{r=1}^{n} b_r f_{i+1-r} - \sum_{r=1}^{n} b_r f_{i-1+r} \\
&= \sum_{r=1}^{n} b_r (f_{i+r} - f_{i-r}) + \sum_{r=0}^{n-1} b_{r+1} f_{i-r} - \sum_{r=0}^{n-1} b_{r+1} f_{i+r}
\end{aligned}$$

Finally, the recursive formula is obtained:

$$\sum_{r=1}^{n} a_r (f_{i+r} - f_{i-r}) = \sum_{r=1}^{n} b_r (f_{i+r} + f_{i+1-r} - f_{i-1+r} - f_{i-r})$$

For $j = n$, $a_n = b_n$ and for $1 \leq j \leq n-1$ the a_j can be computed via $a_j = b_j - b_{j+1}$. Kim and Lee [78] writes this

$$b_j = \sum_{l=j}^{n} a_l.$$

For example, for a classical fourth-order finite-difference scheme the coefficients for a_r are:

$$\left| \frac{\partial f(u)}{\partial x} \right|_i \approx a_1 (f_{i+1} - f_{i-1}) + a_2 (f_{i+2} - f_{i-2}), \; a_1 = 8/12, \; a_2 = -1/12$$

and the coefficients for b_r are:

$$\left| \frac{\partial f(u)}{\partial x} \right|_i \approx b_1 (f_{i+1} + f_i) + b_2 (f_{i+2} + f_{i-1}) - b_1 (f_i + f_{i-1}) - b_2 (f_{i+1} + f_{i-2})$$

with $b_1 = 7/12$ and $b_2 = -1/12$.

In conclusion, centered finite-difference schemes on uniform Cartesian grids can be written on conservation form which is a necessary condition to deal with strong gradients [88]. This conservative property is still verified on orthogonal curvilinear grids provided some metrics relation are respected [130].

Appendix B

Estimation of the Mach number downstream of an abruptly expanded transonic flow

The simplified flow model is sketched in Figure B.1. A normal shock is situated in the duct and the flow downstream of the normal schock is subsonic. In this section the model such as proposed in the work of Jungowski [75] is derived.

In order to estimate the Mach number behind the shock the equations of mass, momentum and energy are used. The momentum equation writes

$$h(p_h + u_h^2 \rho_h) + (H - h)p_w - H(p_e + \rho u_e^2) = 0.$$

Mass conservation gives

$$h\rho_h u_h - H\rho_e u_e = 0.$$

Assuming adiabatic walls, the energy conservation gives:

$$c_p T_h + \frac{1}{2}u_h^2 - c_p T_e + \frac{1}{2}u_e^2 = 0.$$

In terms of the local Mach number $M = u/c$ and $c^2 = \gamma p/\rho$ the momentum equation writes:

$$hp_h(1 + \gamma M_h^2) + (H - h)p_w - p_e(H + h\gamma M_e^2) = 0.$$

This can be rearranged such as

$$\Phi p_h(1 + \gamma M_h^2) + (1 - \Phi)p_w - p_e(1 + \gamma M_e^2) = 0,$$

Using the fact that the flow in the throat is sonic ($M_h = 1$) the quantity $p_h/p_0 = ((\gamma + 1)/2)^{-\gamma/(\gamma-1)}$ can be introduced:

$$(1 + \gamma)\left(\frac{2}{\gamma + 1}\right)^{\frac{\gamma}{(\gamma-1)}} + \frac{(1 - \Phi)}{\Phi}\frac{p_w}{p_0} - \frac{1}{\Phi}(1 + \gamma M^2)\frac{p_e}{p_0} = 0.$$

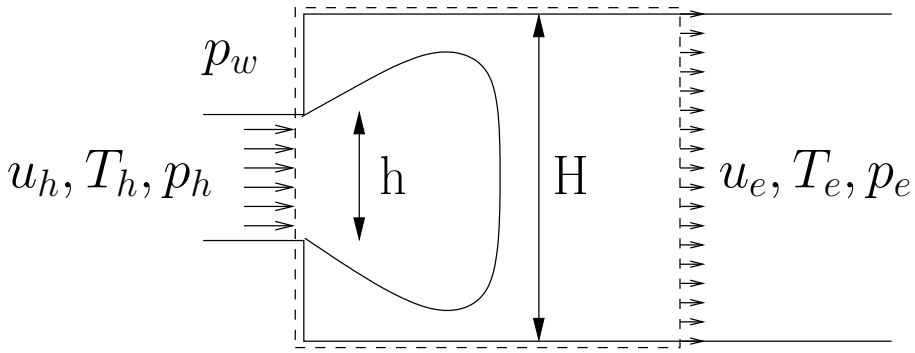

Figure B.1: Simplified model of the expansion of a confined flow; box bounded with - - - is the control volume for the application of the conservation equations.

Now, the quantities p_e/p_0 and Φ_j can be estimated using the mass conservation and energy conservation equations. These can be written in terms of local Machnumber following Candel [34] with $c_p = \gamma R/(\gamma - 1)$

$$T_h(1 + \frac{\gamma - 1}{2}M_h^2) = T_e(1 + \frac{\gamma - 1}{2}M_e^2).$$

A relation between the temperatures and the exit Mach number is found with $M_h = 1$

$$\frac{T_h}{T_e} = \frac{(1 + \frac{\gamma-1}{2}M_e^2)}{(\frac{\gamma+1}{2})}$$

The mass conservation equations gives using the perfect gas law $p = \rho RT$:

$$\frac{p_h}{p_e} = \frac{1}{\Phi}M_e\sqrt{\frac{T_h}{T_e}}.$$

Using the relation for the temperature gives

$$\frac{p_h}{p_e} = \frac{1}{\Phi}M_e\sqrt{\frac{(1 + \frac{\gamma-1}{2}M_e^2)}{(\frac{\gamma+1}{2})}}.$$

Introducing the relation for $p_h/p_0 = ((\gamma + 1)/2)^{-\gamma/(\gamma-1)}$

$$\frac{p_0}{p_e} = \frac{1}{\Phi}M_e\left(\frac{\gamma + 1}{2}\right)^{\frac{\gamma}{\gamma-1}}\sqrt{\frac{(1 + \frac{\gamma-1}{2}M_e^2)}{(\frac{\gamma+1}{2})}},$$

giving

$$\frac{p_0}{p_e} = \frac{1}{\Phi}M_e\left(\frac{\gamma + 1}{2}\right)^{\frac{\gamma+1}{2(\gamma-1)}}\sqrt{1 + \frac{\gamma - 1}{2}M_e^2}.$$

Finally, one obtains the relation between $p_w/p0$ and M_e:

$$(1 + \gamma)\left(\frac{2}{\gamma + 1}\right)^{\frac{\gamma}{(\gamma-1)}} + \frac{(1 - \Phi)}{\Phi}\frac{p_w}{p_0} - \left(\frac{2}{\gamma + 1}\right)^{\frac{\gamma+1}{2(\gamma-1)}}\frac{1 + \gamma M_e^2}{M_e\sqrt{1 + \frac{\gamma-1}{2}M_e^2}} = 0,$$

and gives the equation obtained by Jungowski [75].

Bibliography

[1] *Second Computational AeroAcoustics (CAA) workshop on benchmark problems.* (1997) NASA CP 3352.

[2] *Third Computational AeroAcoustics (CAA) workshop on benchmark problems.* (2000) NASA/CP-2000-209790.

[3] Ahuja K.K., Mendoza J. *Effects of cavity dimensions, boundary layer and temperature on cavity noise with emphasis on benchmark data to validate computational aeroacoustic codes.* Contractor report 4653, NASA, 1995.

[4] Amandolése X., Hemon P. *Essais aéroacoustiques de cavités au banc cornemuse.* Institut Aérotechnique, (2001) Rapport 2434/A.

[5] Amandolese X., Hemon P., and Regardin C. *Study of the acoustic oscillations by flows over cavities. Part1. Internals flows.* Proceedings of the Fifth International Symposium on Fluid-Structure Interactions, IMECE'02, New Orleans, (2002).

[6] Anderson J.S., Jungowski W.M., Hiller W.J., and Meier G.E.A. *Flow oscillations in a duct with a rectangular cross-section.* Journal of Fluid Mechanics, **79** (1977), 769-784.

[7] Arachambeau F., Mechitoua N. and Sakiz M. *A finite volume method for the computation of turbulent incompressible flows.* International Journal of Finite Volumes, (2003).

[8] Arunajatesan S., Sinha N. *Unsteady RANS-LES simulations of cavity flowfields.* AIAA Paper, 2001-0516.

[9] Bailly, C. and Comte-Bellot, G. *Turbulence.* CNRS Editions, Paris, 2003.

[10] Bailly C., Candel S. and Lafon P. *Prediction of supersonic jet noise from a statistical acoustic model and a compressible turbulence closure.* Journal of Sound and Vibrations, **194** (1996), 219-242.

[11] Bailly C., Juvé D. *A stochastic approach to compute subsonic noise using linearized Euler's equations.* AIAA Paper, 99-1872.

[12] Bailly C., Lafon P. and Candel S. *Computation of noise generation and propagation for free and confined turbulent flows.* AIAA Paper, 96-1732.

[13] Barth, T. & Frederickson P. *High-order solution of the Euler equations on unstructured grids using quadratic reconstruction.* AIAA Paper 90-0013, (1990).

[14] Bastin F., Lafon P. and Candel S. *Computation of jet mixing noise due to coherent structures: the plane jet case.* Journal of Fluid Mechanics, **335** (1997), 261-304.

[15] Bayliss, A. & Turkel, E. *Far-field boundary conditions for compressible flows.* Journal of Computational Physics, **48** (1982), 182-199.

[16] Béchara W., Bailly C., Lafon P. and Candel, S. *Stochastic approach to noise modeling for free turbulent flows.* AIAA Journal, **32** (1994), 455-463.

[17] Béchara W., Lafon P., Bailly C. and Candel, S. *Application of a K-Epsilon model to the prediction of noise for simple and coaxial free jets.* Journal of the Acoustical Society of America, **97** (1995).

[18] Benek J.A., Steger J.L. and Dougherty F.C. *A flexible grid embedding technique with applications to the Euler equations.* AIAA Paper, 83-1944 (1983).

[19] Benhamadouche S., Laurence D. *LES, coarse LES, and transient RANS comparisons on the flow across a tube bundle.* International Journal of Heat and Fluid Flow, **24** (2003), 470-479.

[20] Berland J., Bogey C., and Bailly C. *Numerical study of screech generation in a planar supersonic jet.* Physics of Fluids, **266** (2007), 1211-1217.

[21] Berland J., Bogey C., Marsden O. and Bailly C. *High-order, low dispersive and low dissipative explicit schemes for multiple-scale and boundary problems.* Journal of Computational Physics, **224** (2006), 637-662.

[22] Block P.J.W. *Noise response of cavities of varying dimensions at subsonic speeds.* Tech. note D-8351, NASA, (1976), 185-200.

[23] Bogar T.J. *Structure of self-excited oscillations in transonic diffuser flows.* AIAA Journal, **24** (1986), 54-61.

[24] Bogar T.J., Sajben M. and Kroutil J.C. *Shock wave oscillations in transonic diffuser flow.* AIAA Journal, **17** (1979), 1076-1083.

[25] Bogey C. *Calcul direct du bruit aérodynamique et validation de modéles acoustiques hybrides.* Ecole Centrale de Lyon, 2002 Ph.D. Thesis.

[26] Bogey C., Bailly C. *Large Eddy Simulations of transitional round jets : influence of the Reynolds number on flow development and energy dissipation.* Physics of Fluids, **18** (2006), 1-14.

[27] Bogey C., Bailly C. *Decrease of the effective Reynolds number with eddy-viscosity sugrid-scale modeling.* AIAA Journal, **43** (2005), 437-439.

[28] Bogey C., Bailly C. *Three-dimensional non-reflective boundary conditions for acoustic simulation: far field formulation and validation test cases.* Acta Acustica United With Acustica, **88** (2002), 463-471.

[29] Bogey C., Bailly C. and Juvé D. *Noise investigation of a high subsonic, moderate Reynolds number jet using a compressible Large Eddy Simulation.* Theoretical and Computational Fluid Dynamics, **16** (2003), 273-297.

[30] Bogey C., Bailly C. and Juvé D. *A family of low dispersive and low dissipative schemes for Large Eddy simulations and for sound propagation.* Journal of Computational Physics, **194** (2004), 194-214.

[31] Boris J.B., Grinstein F.F. Oran E.S. and Kolbe R.K. *New insights into large eddy simulation.* Fluid Dynamics Research, **10** (1992), 199-228.

[32] Borland C.J. *Numerical prediction of the unsteady flow field in an open cavity.* AIAA Paper, 77-673.

[33] Bres G.A., Colonius T. *Direct numerical simulations of three-dimensional cavity flows.* AIAA Paper, 2007-3405.

[34] Candel, S. *Mécanique des fluides.* Dunod, Paris, 2001.

[35] Chessirre G. and Henshaw W. D. *Composite overlapping meshes for the solution of partial differential equations.* Journal of Computational Physics, **90** (1990), 1-64.

[36] Cockburn B., Shu C.W. *TVB Runge-Kutta local projection discontinuous Galerkin finite element method for conservation laws II.* Mathematics of Computation, **52** (1989) 411-435.

[37] Colonius, T. *An overview of simulation, modeling and active control of flow/acoustic resonance in open cavities.* AIAA Paper, 2001-0076.

[38] Colonius, T. *Modeling Artificial Boundary Conditions for Compressible Flows.* Annu. Rev. Fluid Mech., **36** (2004), 315-345.

[39] Colonius T., Basu A.J. and Rowley C.W. *Numerical investigation of the flow past a cavity.* AIAA Paper, 99-1912.

[40] Colonius T., Lele S.K. *Computational aeroacoustics: progress on nonlinear problems of sound generation.* Progress in Aerospace Sciences, **40** (2004), 345-416.

[41] Colonius T., Lele S.K. and Moin P. *Sound generation in a mixing layer.* Journal of Fluid Mechanics, **330** (1997), 375-409.

[42] Daude F. *Méthode d'intégration temporelle implicite pour la Simulation des Grandes Échelles : application à la réduction du bruit de cavité.* Université Poitiers, 2007 Ph.D. Thesis.

[43] Delfs J.W. *An overlapped grid technique for high resolution CAA schemes for complex geometries.* AIAA Paper, 2001-2199.

[44] Dequand S., Hulshoff S.J. and Hirschberg A. *Self-sustained oscillations in a closed side branch.* Journal of Sound and Vibration, **265** (2003), 359-386.

[45] Desquesnes G., Terracol M., Manoha E., and Sagaut P. *On the use of a high order overlapping grid method for coupling in CFD/CAA.* Journal of Computational Physics, **220** (2006), 355-362.

[46] Dolling D.S. *Fifty years of shock-wave/ boundary layer interaction research: what next ?* AIAA Journal, **39** (2001), 1517.

[47] Domaradski J.A., Yee P. *The subgrid-scale estimation model for high Reynolds number turbulence.* Physics of Fluids, **12** (2000), ?

[48] Ducros F., Ferrand V., Nicoud F., Weber C., Darracq D., Gacherieu C. and Poinsot T. *Large-eddy simulation of the shock/turbulence interaction.* Journal of Computational Physics, **152** (1999), 517-549.

[49] Dumbser M., Munz C.D. *ADER discontinous Galerkin schemes for aeroacoustics.* Comptes Rendus de la Mécanique, **333** (2005), 683-687.

[50] Ekaterinaris J.A. *High-order accurate, low numerical diffusion methods for aerodynamics.* Progress in Aerospace Sciences, **41** (2005), 192-300.

[51] Erlebacher G., Hussaini M.Y., Speziale C.G. and Zang T.A. *Towards the large eddy simulation of compressible turbulent flows.* Journal of Fluid Mechanics, **238** (1992), 155-185.

[52] Ewert R., Schroder W. *Acoustic perturbation equations based on flow decomposition via source filtering.* Journal of Computational Physics, **188** (2003), 365-398.

[53] Forestier N. *Etude expérimentale d'une couche cisaillée au-dessus d'une cavité en régime transsonique.* Ecole Centrale de Lyon, 2000 Ph.D. Thesis.

[54] Freund J.B. *Noise sources in a low-Reynolds-number turbulent jet at Mach 0.9.* Journal of Fluid Mechanics, **438** (2001), 277-305.

[55] Garnier E., Mossi M., Sagaut P., Comte P., and Deville M. *On the use of shock-capturing schemes for large-eddy simulation.* Journal of Computational Physics, **153** (1999), 273-311.

[56] Garnier E., Sagaut P., and Deville M. *A class of explicit ENO filters with applications to unsteady flows.* Journal of Computational Physics, **170** (2001), 184-204.

[57] Garnier E., Sagaut P., and Deville M. *Large-eddy simulation of shock/boundary-layer interaction.* AIAA Journal, **40** (2002), 1935 - 1944.

[58] Germano M., Piomelli U., Moin P. and Cabot W.H. *A dynamic subgrid-scale eddy viscosity model.* Physics of Fluids, **3** (1991), 1760 - 1765.

[59] Geurts B.J. *Elements of direct and large-eddy simulation.* Edwards, 2003.

[60] Gloerfelt X. *Bruit rayonné par un écoulement affleurant une cavité: Simulation directe et application de méthodes intégrales.* Ecole Centrale de Lyon, 2001 Ph.D. Thesis.

[61] Gloerfelt X., Bailly C. *Étude 2-D d'une cavité peu profonde.* Rapport final de travail de la collaboration ECL -EDF R&D AMA, 2002.

[62] Gloerfelt X., Bailly C. and Juvé D. *Direct computation of the noise radiated by a subsonic cavity flow and application of integral methods.* Journal of Sound and Vibration, **266**(1) (2003), 119-146.

[63] Guénanff R. *Couplage instationnaire Navier-Stokes/Euler pour la génération et le rayonnement des sources de bruit aérodynamique.* IRMAR Rennes, 2004 Ph.D. Thesis.

[64] Harten A. *The Artifical Compression Method for computation of shocks and contact discontinuities: III self-adjusting hybrid schemes.* Mathematics of Computation, **32** (1978), 363-389.

[65] Harten A. *A high resolution scheme for computation of weak solutions of hyperbolic conservation laws.* Journal of Computational Physics, **49**,35 (1983).

[66] Heller H.H., Bliss D.B. *The physical mechanism of flow-induced pressure fluctuations in cavities and concepts for their suppression.* AIAA Paper, 75-491.

[67] Heo D.N. Lee D.J. *Numerical investigation of the cover-plates effects on the rectangular open cavity.* AIAA Paper, 2001-2127.

[68] Hirsch, C. *Numerical Computation of internal and external flows Vol.2.* John Wiley & Sons Ltd., (1984).

[69] Hixon, R. *Numerically consistent strong conservation grid motion for finite difference schemes.* AIAA Journal, **38** (2000) 1586-1594.

[70] Hixon, R. and Turkel, E. *Compact Implicit MacCormack-Type Schemes with High Accuracy.* Journal of Computational Physics, **158** (2000) 51-70.

[71] Hixon R., Bathe D., Nallasamy M., and Sawyer, S. *Shock-capturing dissipation schemes for high-accuracy Computational Aeroacoustics (CAA) codes.* AIAA Paper, 2006-3413.

[72] Inoue, O. Hatakeyama, N. *Sound generation by a two-dimensional circular cylinder in a uniform flow.* Journal of Fluid Mechanics, **471** (2002) 285-314.

[73] Jameson A., Schmidt W. and Turkel E. *Numerical simulation of the Euler equations by finite volume methods using Runge-Kutta time stepping schemes.* AIAA Paper, (1981) 81-1259.

[74] Jiang, G.S. and Shu, C.W. *Efficient Implementation of Weighted ENO Schemes.* Journal of Computational Physics, **126** (1996) 202-228.

[75] Jungowski W.M. *Investigation of flow pattern, boundary conditions and oscillation mechanism in a compressible flow through sudden enlargement of a duct.* Warsaw Techn. Univ. Publ., **3** (1968).

[76] Karamcheti K. *Acoustic radiation from two-dimensional rectangular cutouts in aerodynamic surfaces.* NACA, Techincal Note 3487.

[77] Kim J.W., Lee D.J. *Generalized characteristic boundary conditions for Computational Aeroacoustics.* AIAA Journal, **38** (2000), 2040-2049.

[78] Kim J.W., Lee D.J. *Adaptive non-linear artificial dissipation model for Computational Aeroacoustics.* AIAA Journal, **39** (2001), 810-818.

[79] Kim J.W., Lee D.J. *Generalized Characteristic Boundary Conditions for Computational Aeroacoustics, Part 2.* AIAA Journal, **42** (2004) 47-55.

[80] Komerath N.M., Ahuja K.K. and Chambers F.W. *Prediction and measurements of flows over cavities- a survey.* AIAA Paper, 87-0166.

[81] Lafon P., Caillaud S., Devos J.P. and Lambert C. *Aeroacoustical coupling in a ducted shallow cavity and fluid-structure effects on a steam line.* Journal of Fluids and Structures, **18** (2003) 695-713.

[82] Lafon P., Devos J. P. *Numerical prediction of instabilities in transonic internal flows using an Euler TVD code.* AAIA Paper, (1993) 1993-72.

[83] Lafon P., Devos J. P. *Computation of the noise generated by a shallow cavity and test of a solution for lowering the noise.* AAIA Paper, (2003) 2003-3105.

[84] Larchevêque L., Sagaut P., Lê T.-H. and Comte P. *Large-eddy simulation of a compressible flow in a three-dimensional flow at high Reynolds number.* Journal of Fluid Mechanics, **516** (2004) 265-301.

[85] Larchevêque L., Sagaut P., Mary I., Labbe O. and Comte P. *Large-eddy simulation of a compressible flow past a deep cavity.* Physics of Fluids, **15(1)** (2003) 193-210.

[86] Lele K.S. *Compact finite difference schemes with spectral-like resolution.* Journal of Computational Physics, **103** (1992), 16-42.

[87] Metais O. Lesieur M. and Comte P. *Large-eddy simulations of turbulence.* Cambridge University Press, 2005.

[88] LeVeque R.J. *Numerical Methods for Conservation Laws.* Lectures in Mathematics, ETH-Zurich, Birkhauser-Verlag, Basel, 1990.

[89] Lo S.-C., Blaisdell G.A. and Lyrintzis A.S. *High-Order shock capturing schemes for turbulence calculations.* AIAA Paper, 2007-827.

[90] Lockard D.P., Morris P.J. *A parallel implementation of a Computational Aeroacoustics for airfoil noise.* Journal of Computational Acoustics, **5** (1997) 337-353.

[91] Longatte E., Lafon P. and Candel S. *Computation of noise generation by turbulence in internal flows.* AIAA Paper, 98-2332.

[92] Marsden O., Bogey C. and Bailly C. *High-order curvilinear simulations of flows around non-cartesian bodies.* Journal of Computational Acoustics, **13**(4) (2005), 732-748.

[93] Mathew J., Lechner R., Foysi H., Sesterhenn, J. and Friedrich R. *An explicit filtering method for large eddy simulation of compressible flows.* Physics of Fluids, **15** (2003) 2279-2289.

[94] Meier G.E.A., Grabitz G., Jungowski W.M., Witczak K.J and Anderson J.S. *Oscillations of the supersonic flow downstream of an abrupt increase in duct cross-section.* Mitteilung aus dem Max-Planck-Institut fuer Stroemungsforschung und der Aerodynamischen Versuchsanstalt, **65** (1978), 1-172.

[95] Meier G.E.A., Szumowski A.P. and Selerowicz W.C. *Self-excited oscillations in internal transonic flows.* Progress in Aerospace Sciences, **2** (1990), 145-200.

[96] Normand X. and Lesieur M. *Direct and large-eddy simulations of transition in the compressible boundary layer.* Theoretical and Computational Fluid Dynamics, **3** (1992) 231-252.

[97] Oster D., Wygnanski I. *The forced mixing layer between parallel streams.* Journal of Fluid Mechanics, **123** (1982) 91-130.

[98] Pirozzoli S., and Grasso F. *Direct numerical simulation of impinging shock wave/turbulent boundary layer interaction at M=2.25.* Physics of Fluids, **18** (2006) 065113.

[99] Poinsot T.J., Lele K.S. *Boundary conditions for direct simulations of compressible viscous flows.* Journal of Computational Physics, **101** (1992), 104-129.

[100] Prewitt N.C., Belk D.M. and Shyy W. *Parallel computing of overset grids for aerodynamic problems with moving objects.* Progress in Aerospace Sciences, **36** (2000) 117-172.

[101] Pulliam T.H., Steger J.L. *On implicit finite-difference simulations of three dimensional flow.* AIAA Paper, (1978) 78-10.

[102] Pulliam T.H., Steger J.L. *Implicit finite-difference simulations of three dimensional flow.* AIAA Journal, **18** (1980) 159-167.

[103] Ricot D., Maillard V. and Bailly C.,. *Numerical simulation of unsteady cavity flow using Lattice Boltzmann method.* AIAA Paper, 2002-2532.

[104] Rizzetta D.P. *Numerical simulation of supersonic flow over a three dimensional cavity.* AIAA Journal, **26** (1988) 799-807.

[105] Rizzetta D.P., Visbal M.R. and Blaisdell G.A. *A time-implicit compact differencing and filtering scheme for large-eddy simulation.* Int. J. Numer. Meth. Fluids, **42**(6) (2003) 665-693.

[106] Rizzetta D.P., Visbal M.R. and Gaitonde D.V. *Large-eddy simulation of supersonic compression-ramp flow by high-order method.* AIAA Journal, **39** (2001) 2283-2292.

[107] Rockwell D. *Prediction of oscillation frequencies for unstable flow past cavities.* ASME Journal of Fluids Engineering, **99** (1977) 294-300.

[108] Rockwell D., Naudascher E. *Review: self-sustained oscillations of flows past cavities.* Journal of Fluids Engineering, **100** (1978) 125-165.

[109] Rogers S.E., Suhs N.E. and Dietz W.E. *PEGASUS5: An automated preprocessor for overset computational fluid dynamics.* AIAA Journal, **41** (2003) 1037-1045.

[110] Rossiter C.W. *Wind-tunnel experiments in the flow over rectangular cavities at subsonic and transsonic speeds.* Aeronautical Research Council Reports and Memoranda, Technical Report 3438.

[111] Sagaut P. *Large-eddy simulation of incompressible flow - An introduction.* Scientific Computation. Springer Verlag, 2001.

[112] Sahoria V. *Experimental and analytical investigation of oscillations in flows over cavities.* California Institute of Technology, 1975 Ph.D. Thesis.

[113] Schlichting H. *Boundary Layer Theory.* McGraw-Hill, Inc., (1979), 328.

[114] Schwartzkopff T., Dumbser M. and Munz C.D. *CAA using domain decomposition and high-order methods on structured and unstructured meshes.* AIAA Paper, 2004-2964.

[115] Schwartzkopff T., Dumbser M. and Munz C.D. *Fast high order ADER schemes for linear hyperbolic equations.* Journal of Computational Physics, **197** (2004), 532 - 539.

[116] Sherer S.E., Scott J.N. *High-order compact finite-difference methods on general overset grids.* Journal of Computational Physics, **210** (2005), 459 - 496.

[117] Shu, C.W. and Osher S. *Efficient Implementation of Essentially Non-oscillatory Shock-Capturing Schemes II.* Journal of Computational Physics, **83** (1989) 32-78.

[118] Sinha N., Dash S.M., Chidambaram N. and Finlay D. *A perspective on the simulation of cavity aeroacoustics.* AIAA Paper, 98-0286.

[119] Smits A.J. Dussauge J.P. *Turbulent Shear Layers in Supersonic Flows, second edition.* Springer, NY, (2006).

[120] Stolz, S. and Adams N.A. *An approximate deconvolution procedure for large eddy simulation.* Physics of Fluids, **11** (1999) 1699-1701.

[121] Swanson R.C., Turkel E. *Artificial dissipation and central difference schemes for the Euler and Navier-Stokes equations.* AIAA Paper, 78-1107.

[122] Tadeka K., Shieh C.M. *Cavity tones by Computational Aeraoustics.* International Journal of Computational Fluid Dynamics, **18** (2004), 439 - 454.

[123] Tam C.K.W. *Computational Aeroacoustics: An overview of Challenges and Applications.* International Journal of Computational Fluid Dynamics, **18** (2004), 547 - 567.

[124] Tam, C.K.W. and Hu, F.Q. *An optimized multi-dimensional interpolation scheme for Computational Aeroacoustics applications using overset grids.* AIAA Paper, AIAA 2004-2812.

[125] Tam, C.K.W. and Shen, H. *Direct computation of nonlinear acoustic pulses using high-order finite difference schemes.* AIAA Paper, AIAA 93-4325.

[126] Tam C.K.W., Block P.J.W. *On the tones and pressure oscillations induced by flow over rectangular cavities.* Journal of Fluid Mechanics, **89** (1978), 373 - 399.

[127] Tam C.K.W., Dong Z. *Radiation and outflow boundary conditions for direct computation of acoustic and flow disturbances in a nonuniform mean flow.* Journal of Computational Acoustics, **4** (1996),175-201.

[128] Tam C.K.W., Webb J.C. *Dispersion-relation-preserving finite difference schemes for Computational Acoustics.* Journal of Computational Physics, **107** (1993), 262 - 281.

[129] Testud P. *Aéro-acoustique des diaphragmes en conduit: sifflement et cavitation.* Université du Maine, 2004 Ph.D. Thesis.

[130] Thomas P.D., Lombard C.K. *Geometric conservation law and its application to flow computations on moving grids.* AIAA Journal, **17**(10) (1979), 1030-1037.

[131] Thompson, K.W. *Time Dependent Boundary Conditions for Hyperbolic Systems.* Journal of Computational Physics, **68** (1978), 1-24.

[132] Thompson, K.W. *Time Dependent Boundary Conditions for Hyperbolic Systems,II.* Journal of Computational Physics, **89** (1990), 439-461.

[133] Tracy, M.B. Plentovich E.B. *Cavity unsteady-pressure measurements at subsonic and transonic speeds.* Technical paper 3669, NASA, (1997).

[134] Uzun A., Hussaini M.Y. and Streett C.L. *Progress towards multi-block Large Eddy Simulations for wind turbine aeroacoustics.* AIAA Paper, 2005-1190.

[135] Van Leer B. *Towards the ultimate conservative difference scheme II. Monotonicty and conservation combined in a second-order scheme.* Journal of Computational Physics, **14** (1974), 361-370.

[136] Vinokur M. *Conservation equations of gasdynamics in curvilinear systems.* Journal of Computational Physics, **14** (1974), 105-125.

[137] Visbal M.R., Gaitonde D.V. *Shock capturing using compact-differencing-based methods.* AIAA Paper, 2005-1265.

[138] Vreman B., Geurts B. and Kuerten H. *A priori tests for large-eddy simulation of compressible plane mixing layer.* Journal of Engineering Mathematics, **29** (1995), 299-327.

[139] Vreman B., Geurts B. and Kuerten H. *Large eddy simulation of the turbulent mixing layer.* Journal of Fluid Mechanics, **339** (1997), 357-390.

[140] Vreman B., Geurts B. and Kuerten H. *Subgrid-modeling in LES of compressible flow.* Applied Scientific Research, **54** (1995), 191-203.

[141] Wang Z.J. *Spectral (finite) volume method for conservation laws on unstructured grids.* Journal of Computational Physics, **178** (2002), 210-251.

[142] Yee H.C., Sandham N.D., and Djomehri M.J. *Low-Dissipative High-Order Shock-Capturing Methods Using Characteristic Based Filters.* Journal of Computational Physics, **150** (1999), 199-238.

[143] Zaman K.B.M.Q., Dahl M.D., Bencic T.J., and Loh C.Y. *Investigation of a transonic resonance with convergent-divergent nozzles.* Journal of Fluid Mechanics, **463** (2002), 313-343.

[144] Zhang U.F., Fey U. Noack B.R. Koenig M. and Eckelmann H. *On the transition of the cylinder wake.* Physics of Fluids, **4** (1995), 779-794.

[145] Zhang X., Edwards J.A. *An investigation of supersonic oscillatory cavity flows driven by thick shear layers.* Aeronautical Journal, **100** (1990), 355-364.

[146] Ziada S., Rockwell D. *Vortex-leading edge interaction.* Journal of Fluid Mechanics, **118** (1982), 79-107.

dernière page de la thèse

AUTORISATION DE SOUTENANCE

Vu les dispositions de l'arrêté du 25 avril 2002,

Vu la demande du Directeur de Thèse

Monsieur C. BAILLY

et les rapports de

Monsieur C-D. MUNZ
Professeur - Institut für Aerodynamik und Gasdynamik - Universität Stuttgart - Pfaffenwaldring 21
D-70550 Stuttgart - ALLEMAGNE

Et de

Monsieur P. SAGAUT
Professeur - D'Alembert Institute - Université Pierre et Marie Curie - Paris 6 - 4, place Jussieu - Case 162
75252 Paris cedex 5

Monsieur EMMERT Thomas

est autorisé à soutenir une thèse pour l'obtention du grade de **DOCTEUR**

Ecole doctorale MECANIQUE, ENERGETIQUE, GENIE CIVIL ET ACOUSTIQUE (MEGA)

Fait à Ecully, le 8 novembre 2007

P/Le Directeur de l'E.C.L.
Le Directeur des Etudes

ECOLE CENTRALE DE LYON
SCOLARITE
3ème Cycle

M. JOSEPH

Développement d'un algorithme d'ordre élevé multi-domaines pour l'aéroacoustique numérique: Application aux écoulements confinés en régimes subsonique et transonique

Un nouvel algorithme de simulation numérique pour l'aéroacoustique, SAFARI (Simulation Aéroacoustique des Fluides Avec Résonances et Interactions), a été développé pour le calcul direct du bruit. Il s'appuie sur la résolution des équations de Navier-Stokes compressibles en coordonnées curvilignes. Des schémas aux différences finies d'ordre élevé sont implémentés. La solution est calculée sur des maillages recouvrants (méthode Chimère) pour traiter des géométries complexes. L'interpolation entre les maillages est effectuée par des polynômes de Lagrange également d'ordre élevé. De plus chaque maillage est découpé en blocs pour permettre l'exécution du calcul sur des machines parallèles. Le solveur est parallélisé à l'aide de la bibliothèque MPI. Afin d'assurer la capture des chocs forts, un filtre non linéaire de type Jameson est utilisé.

SAFARI est d'abord confronté à des cas-test simples: par exemple en 1-D l'écoulement dans une tuyère convergente/divergente ou en 2-D l'écoulement à bas nombre de Reynolds autour d'un cylindre. Les cas tests montrent que l'algorithme produit des résultats de haute précision et est bien adapté pour des calculs aéroacoustiques.

Ensuite, les simulations en 3-D de deux cas d'intérêt industriel sont présentées. D'abord un écoulement à nombre de Reynolds élevé et à nombre de Mach modéré affleurant une cavité confinée a été simulé. Pour des cavités confinées les modes de cavité peuvent se coupler avec les modes de résonance de la veine et produire des oscillations de grande amplitude. Le calcul met clairement ce couplage en évidence.

La deuxième application industrielle traitée dans le cadre de ce travail est la simulation d'un écoulement transsonique au travers d'un élargissement brusque dans un conduit plan. En fonction de la pression en aval, différents régimes d'écoulements s'établissent dans le tuyau. Pour des pressions faibles, l'écoulement est supersonique dans le tuyau et un système de chocs obliques s'établit. Pour des pressions plus élévées, un choc droit oscillant apparaît dans l'écoulement. Les oscillations de ce choc se couplent avec les modes acoustiques longitudinaux du tuyau. Pour des pressions en aval encore plus élevées , le jet recolle sur une des parois inférieure ou supérieure et des cellules des choc sont observées. Les résultats présentés dans ce travail reproduisent tous les aspects de ce type d'écoulement.

Development of a multidomain high-order algorithm for computational aeroacoustics: Application to subsonic and transonic confined flows

A new algorithm for computational aeroacoustics, SAFARI (Simulation Aéroacoustique des Fluides Avec Résonances et Interactions) is proposed for the direct calculation of noise. The compressible Navier-Stokes equations are solved using high-order finite difference schemes on structured curvilinear grids. To tackle with complex geometries, a high-order overset grid approach is implemented that consists in decomposing the geometry in grids that overlap. Communication between grids is computed by high-order multidimensional Lagrangian polynomials. Each grid is divided into blocks for allowing the use of parallel computing. The code has been parallelized using MPI-library and has been validated on massively parallel platforms. In order to accurately capture shocks, a Jameson-like dissipation has been implemented.

For validation, several canonical test cases have been computed that are typical for Computational Fluid Dynamics and Computational AeroAcoustics (CAA): for example a 2-D low Reynolds number flow around a cylinder and the transonic flow in a convergent-divergent nozzle. The test cases demonstrate that the solver is able to provide high-order accurate solutions on complex geometries and the shock-capturing strategy is well adapted to CAA problems

The first industrial application presented in this work is the simulation of a high-Reynolds number flow at low Mach numbers past a ducted cavity. For the chosen flow regime, the cavity modes couple with resonance modes of the duct, leading to high pressure levels. The coupling phenomenon is well reproduced by the computation.

As second industrial application, a sonic flow in a plane duct passing an abrupt increase in cross-section is numerically studied by solving 3-D compressible Navier-Stokes equations. Different flow patterns are likely to appear in such configuration. For a very low downstream pressure, the flow is entirely supersonic. For higher pressures, unstable flow patterns emerge. One of these patterns features a normal shock, that oscillates due to a self-exciting mechanism. As the duct is open at the outflow, aeroacoustic coupling occurs when the shock oscillations get in resonance with the longitudinal acoustic modes of the duct. The simulated flow has been found to be in good agreement with available experimental data.